Carnegie Mellon University
MELLON COLLEGE OF SCIENCE

THESIS

SUBMITTED IN PARTIAL FULFILLMENT OF THE REQUIREMENTS
FOR THE DEGREE OF

DOCTOR OF PHILOSOPHY IN THE FIELD OF PHYSICS

TITLE: "Lyman Alpha Intensity Mapping via Grism Spectrotomography"

PRESENTED BY: Zhonghao Luo

ACCEPTED BY THE DEPARTMENT OF PHYSICS

Jeff Peterson 9/18/17
JEFF PETERSON, CHAIR PROFESSOR DATE

Scott Dodelson 9/18/17
SCOTT DODELSON, DEPT HEAD DATE

APPROVED BY THE COLLEGE COUNCIL

Rebecca Doerge 9/22/17
REBECCA DOERGE, DEAN DATE

Lyman Alpha Intensity Mapping via Grism Spectrotomography

by

Zhonghao Luo

Submitted in partial fulfillment of the
requirements for the degree of
Doctor of Philosophy
at
Carnegie Mellon University
Department of Physics
Pittsburgh, Pennsylvania

Advised by Professor Jeffrey Peterson

September 18, 2017

Abstract

The discovery of cosmic acceleration implies that universe is dominated by some form of "dark energy" that causes repulsive gravity. This accelerated expansion of the universe can be probed by Baryon Acoustic Oscillations (BAO). BAO is a well developed method to measure the expansion history and the structure growth of the universe. Intensity mapping is a new observation technique that can probe BAO and large scale structures. A new type of telescope, the Grism Spectrotomographic Imager (GSTI), is described in the thesis. The GSTI is designed for Lyman Alpha (Lyα) intensity mapping. A grism, the combination of grating and prism, is placed in front of a camera to disperse the light of each point on the sky into a spectrum and shift the spectrum back closer to the original image point. Images are taken as the grism rotates about the optical axis, resulting in a set of grism-dispersed images with different spectra orientations. A hyperspectral data cube is then reconstructed from this set of grism-dispersed images through back projection and point spread function (PSF) deconvolution. The Richardson-Lucy method is chosen as the deconvolution algorithm in the thesis due to its speed and performance. In contrast to other wide field spectroscopy techniques, Grism Spectrotomography collects all available photons simultaneously and efficiently yields the spectrum of each sky pixel within the field of view. It has high throughput and a multiplex advantage. A prototype GSTI was built, and the data acquisition pipeline was developed for the telescope. GSTI was tested in the lab and on the sky. Reconstruction results show that GSTI is capable of simultaneously providing spectra of multiple sources in the field. The star foreground was also carefully studied for intensity mapping. Masking of Milky Way stars is required for cosmological Lyα intensity mapping because bright stars can affect the detection and the power spectrum of Lyα sources. A masking and filtering scheme is proposed to obtain a high signal-to-noise Lyα power spectrum using intensity mapping.

Acknowledgments

A lot of professors, classmates, friends and family members have helped me during my Ph.D. studies. I would like to take a moment to express my gratitude to those who made my research possible and my Ph.D. life memorable.

I would like to start off by thanking my advisor, Jeff Peterson, who can always inspire me with ideas. I would not have gone this far without the understanding and support from Jeff. He guided me through the darkness of research, and offered me great freedom to learn and explore. He encouraged me to always experiment ideas before giving up. He taught me how to study cosmology in an engineering way. Jeff's encouragement, insight, and immense knowledge have been priceless in my growth as a researcher.

Besides my advisor, I would like to thank the rest of my thesis committee. Rupert Croft offered me some helpful advice on simulation. Rachel Mandelbaum and I had useful discussions on star catalogs. Matthew Walker and David Turnshek provided valuable comments on my research and thesis. I would like to thank all of them for making my defense an enjoyable moment. I also want to thank all of them for their encouragement, comments, and suggestions.

I thank all the friends, students, post-docs and professors who helped me overcome the difficulties. I would like to thank Francois Lanusse for sharing his defense experience and advising me on image processing problems. I would like to thank Sukhdeep Singh for helpful discussions on cosmology. I would like to thank Hung-Jin Huang for sharing her code and knowledge on the power spectrum. I would like to thank Hsiu-Hsien Lin for his support, advice, and knowledge. I want to thank Hongyu Zhu for helpful discussions on coding and correlation functions. I want to thank Yixian Zhu for her continuous support and suggestions. I want to thank Sergey Koposov for useful discussions on stars. I would like to thank Siddharth Satpathy for helpful discussions on physics and cosmology. I would like to thank Anthony Pullen for helpful discussions on intensity mapping. I want to thank Tanmay Mudholkar, Mert Terzi and Vikesh Siddhu for studying homework together in the first year. After all, I would like to extend my gratitude to everyone I have met in the Physics department and Carnegie Mellon University.

Finally, I want to extend special thanks to my family. My parents encouraged me to study physics and pursue a Ph.D. degree. They supported my decisions on my research and career. They offered sincere suggestions when I was confronted with troubles. They have always been there for me through good times and bad. I would also like to thank my uncles, aunts, and grandparents for their advice and support.

Contents

List of Tables

List of Figures

Chapter 1

Introduction

Cosmic acceleration is one of the most surprising discoveries in many decades, which requires the existence of some form of "dark energy" with unusual physical properties and repulsive gravity. This "dark energy" is also known as the cosmological constant problem in General Relativity. The profound implication of cosmic acceleration leads to a wide range of experiments to measure the history of expansion and growth of structure in the universe. There are four most well established methods for such measurements: Type Ia supernovae, Baryon Acoustic Oscillations (BAO), weak gravitational lensing, and the abundance of galaxy clusters [17].

Baryon Acoustic Oscillations (BAO) provide one of the features Lyα intensity mapping is aiming at. In an initially dense region in the early universe, the baryon-photon fluid is oscillating as sound waves due to the radiation pressure. The sound waves propagate like spherical waves from the center of dense regions, leaving a spherical structure that ceases propagation at recombination. Although it is difficult to identify this structure by eye, it can be statistically detected because there is an excess of probability that pairs of galaxies are separated by a comoving distance $100\mathrm{h}^{-1}$Mpc [18]. This is the radius of the acoustic sphere, or sound horizon at recombination.

The BAO scale is used as the standard ruler in the universe. Cosmic separations can be measured by this ruler so that Hubble parameter $H(z)$ and angular diameter distance $d_A(z)$ can be determined at various redshifts z. The evolution of the separation with z reveals evidence on cosmic acceleration. By comparing observations with theoretical models, people can further constrain cosmological constant and equation-of-state parameter w.

1.1 Hyperspectral Imaging

Hyperspectral imaging collects the spectral information of every pixel in an image. The final reconstruction result is presented as a hyperspectral data cube, where (x, y) are the spatial coordinates on the image and λ is the spectral coordinate representing wavelength. Spatial coordinates release information about shape, location, and structure of the objects of interest. The spectral coordinate can provide chemical composition and emission fingerprints of the objects. In astronomy, hyperspectral imaging is used to analyze the density, velocity, and distance of the objects within a field. In agriculture, hyperspectral imaging is used to detect the nutrient and water status of wheat in irrigated systems [19]; in mineralogy, it helps to detect minerals in silica, calcite, garnet groups that have strong spectral signature [20]; in food processing industry, it is able to identify defects and foreign materials that are invisible to traditional cameras [21].

In astronomy hyperspectral imaging is also called Integral Field Spectroscopy (IFS), whose scientific goals include [9]: a) study of the distribution of star formation in distant galaxies, b) kinematical studies of galaxies at intermediate redshift, c) intermediate redshift distance estimation with Tully-Fisher relation d) reconstruction of lensed galaxies. In keeping with these goals, IFS usually aims at providing high angular resolution of a small field that includes an extended object, like a galaxy. Expanding the plate scale of the hyperspectral imaging allows wide field spectroscopy to examine large scale structure in the universe. This technique is usually called intensity mapping in astronomy society.

1.2 Intensity Mapping

Intensity mapping is short for three dimensional mapping of the specific intensity due to line emission. The technique assumes the flux due to a single emission is dominant or can be selected out, and the emissivity of the line is linearly related to the source mass density. Then, spectral information can be translated into cosmic density, by converting wavelength to comoving distance and intensity to mass density. Measuring large scale structure (LSS) is one of the key goals of intensity mapping, which reveals important information about cosmological parameters, dark matter, and dark energy. Galaxy surveys such as 2dF Galaxy Redshift Survey (2dFGRS) [22] and Sloan Digital Sky Survey (SDSS) [23, 24, 25] are also used to map cosmic structure but do this by detecting and mapping the coordinates of many individual galaxies. Although the distribution of galaxies can be used to trace LSS, they are more easily detected at low redshifts about $z \leq 1$ because they become fainter at higher redshifts. For higher redshifts, it is challenging to resolve or even detect small and faint objects with galaxy surveys. Intensity mapping provides an alternative way to probe LSS without resolving individual galaxies.

Intensity mapping has been described as a powerful tool to understand the Epoch of Reionization (EoR), when the universe became completely ionized from the neutral state. Further study on EoR will shed light on star formation, galaxy formation and large scale structure (LSS). Intensity mapping has been proposed mostly on long wavelength lines, but very few in visible regions. 21 cm intensity mapping has been developed rapidly to probe this epoch [26, 27, 28, 29, 30], while there are a variety of potential lines that can be used for this purpose, such as CO [31, 32], C II [33, 34, 35], H_2 [36], and Lyα [37]. A short wavelength line He II (164nm) is proposed for intensity mapping, although it is in the infrared region $z = 10 - 20$ [38]. There is also a study indicating that Lyα, Hα, O II, C II and the lowest rotational CO lines are the best candidates for intensity mapping probes [39].

My focus in the thesis is on moderate redshift ($z = 2 \sim 4$) Lyα line. The Lyα line is emitted during the transition from the first excited state (n=2) to the ground state (n=1) of the hydrogen atom. It has a rest wavelength of $\lambda_{Ly\alpha} = 121.567$nm. Ly$\alpha$ emission mainly comes from hot young stars within massive dark matter halos, but can be scattered by neutral gas in the surrounding intergalactic medium (IGM). High energy photons emitted by star forming galaxies in halos ionize the hydrogen, which then recombines to emit Lyα photons [40]. These photons then undergo thousands of scattering in gas in the circumgalactic medium before escaping, making the Lyα emission extended. In addition, the collisions and recombinations in IGM also generate Lyα photons [37]. The UV photons that escape the galaxies can ionize the low-density neutral gas in IGM, which then emits Lyα photons upon recombination. The electrons due to ionization of the gas can also cause collisional excitations that result in Lyα photons [41, 42]. Furthermore, Lyn photons emitted from galaxies can also get scattered by neutral hydrogen and finally produce Lyα. The Lyα intensity from IGM is determined by the thermal and ionization state of the gas which are related to the UV and X-ray backgrounds. However, the Lyα emission from IGM is about ten times lower than galaxy Lyα emission when considered as a contribution to the power spectrum described in Section.3.3 [43]. In this thesis, I mainly focus on the Lyα photons from galaxies that are extended by scattering.

Galaxies are receding from us due to the expansion of the universe. And wavelength of light emitted from a receding object is stretched out so that the observed wavelength is larger than the emitting wavelength. This effect can be characterized by redshift z, which is defined as: [44]

$$1 + z = \frac{\lambda_{obs}}{\lambda_{emit}} \tag{1.1}$$

where λ_{obs} is the observed wavelength, and λ_{emit} is the emitting wavelength. At moderate redshift ($z = 2 \sim 4$), the Lyα line is redshifted to wavelength 365nm $\sim$ 608nm. This wavelength range overlaps with the u band and the g band of SDSS filters. I choose to study this redshift and wavelength because the total night sky brightness is relatively low in this band, as shown in Fig.1.1. Various brightness components outside the lower terrestrial atmosphere are plotted as a function of wavelength. They are discussed in details in Chapter.3. The airglow, zodiacal light, and star light are all brighter as the wavelength increases in the visible light band. Shorter wavelengths are unacceptable for the ground based telescope because they are blocked by the upper atmosphere. Overall, the u band provides a low sky brightness region that is preferable for ground based Lyα intensity mapping.

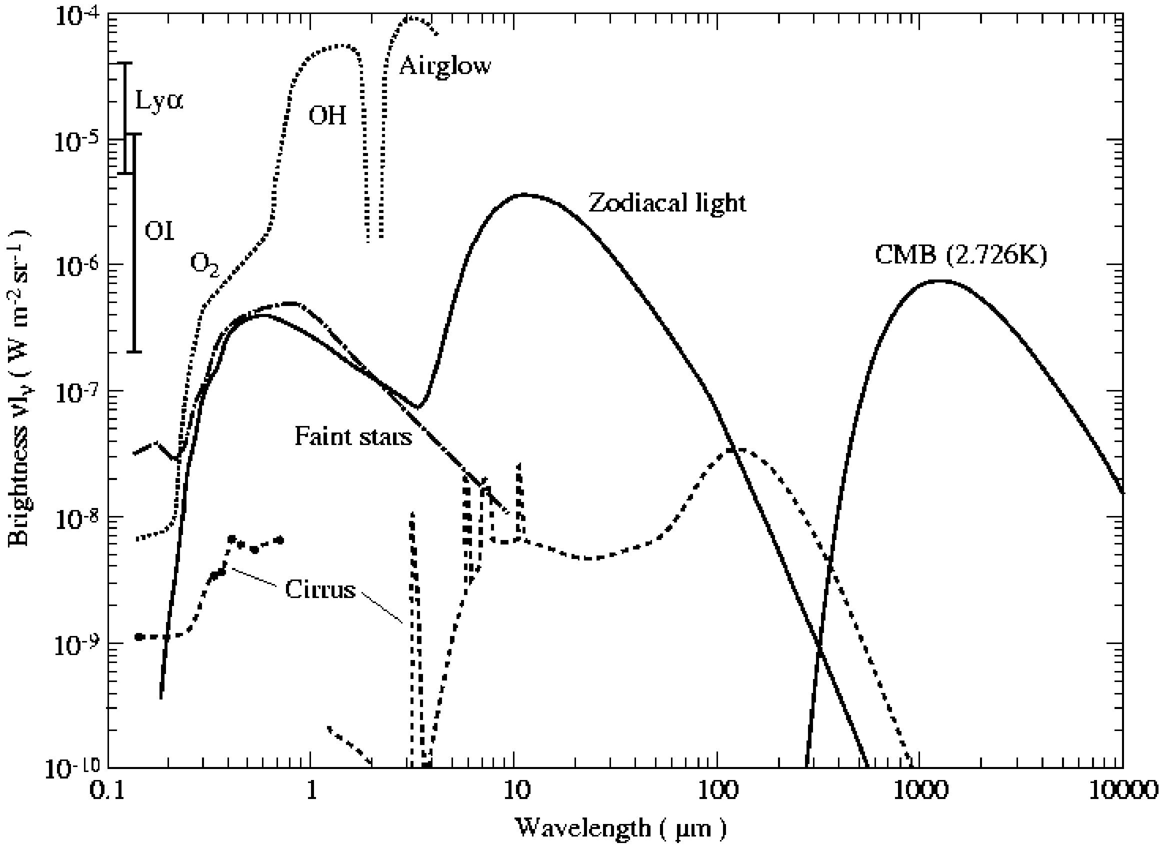

Figure 1.1: Overview on the brightness of the sky outside the lower terrestrial atmosphere and at high ecliptic and galactic latitudes. Various components are plotted separately. Figure adapted from [1].

A few existing theories have indicated the possible results of Lyα intensity mapping experiments. Quantitative models of Lyα emission from $z = 2 - 11$ give an estimate of Lyα intensity and recommend to pursue intensity fluctuations [37, 45]. The power spectrum of the Lyα spatial fluctuations has also been predicted at redshift $z > 4$ based on the Hubble Space Telescope (HST) legacy fields [46].

The mapping speed of an intensity mapping experiment is proportional to throughput(etendue) $A\Omega$, because the specific intensity is measured by intensity mapping is the power per wavelength, per aperture and per solid angle $I_\lambda = dP/(d\lambda dA d\Omega)$. An illustration of throughput is shown in Fig.1.2. Some influential optical telescopes, such as SDSS, have a large aperture A that delivers high flux sensitivity, to compensate for the small Ω of a distant unresolved point source. But detecting individual faint objects is not the goal of intensity mapping. For intensity mapping, a small aperture A instrument can be sensitive if a wide instantaneous field of view Ω is observed. Thus intensity mapping experiments can aim for a wider field of view and use coarser pixels that still provide information on large scale structure. In many optics systems, the throughput is determined by the area of the detector or slit aperture, along with the solid angle subtended by the optics that feed the detector or slit. Holding a constant throughput $A\Omega$, an intensity mapping instrument with large aperture A spends less integration time on a smaller field Ω. And the total time required for the entire survey field is independent of collecting area A. As a result, intensity mapping speed is independent of telescope aperture if throughput is limited at the detector. We can, therefore, use short focal length along with small aperture optics while maintaining a high throughput for intensity mapping. This will minimize the cost and complexity at the same time.

Taking $h = 0.7$ and redshift $z = 2$, the BAO radius is converted to $4.6°$ on the sky, which sets the relevant field size for the instrument. The hyperspectral data cube should cover a field several times this radius. Intensity mapping does not require high angular resolution for large scale structures since the nonlinear scale subtends about 5 arcminutes at this redshift. Instead, the pixel scale is determined by masking requirements, which are discussed in Chapter 3. Several techniques that are commonly used in IFS and their suitability for Lyα intensity mapping are discussed in Chapter 2.

1.3 Instrument

The Wisconsin H-Alpha Mapper(WHAM) is an existing telescope most similar to an intensity mapping instrument, which maps the interstellar medium in the Milky Way [47]. WHAM is designed to obtain spectra of Hα emission from ionized hydrogen and conduct an all-sky survey. WHAM consists of a 0.6-meter telescope and a Fabry-Perot spectrometer, which provides a $1°$ angular resolution and 0.026nm spectral resolution within a 0.44nm spectral window. The large field of view of WHAM increases the sensitivity of WHAM tremendously to faint emission and also illustrates

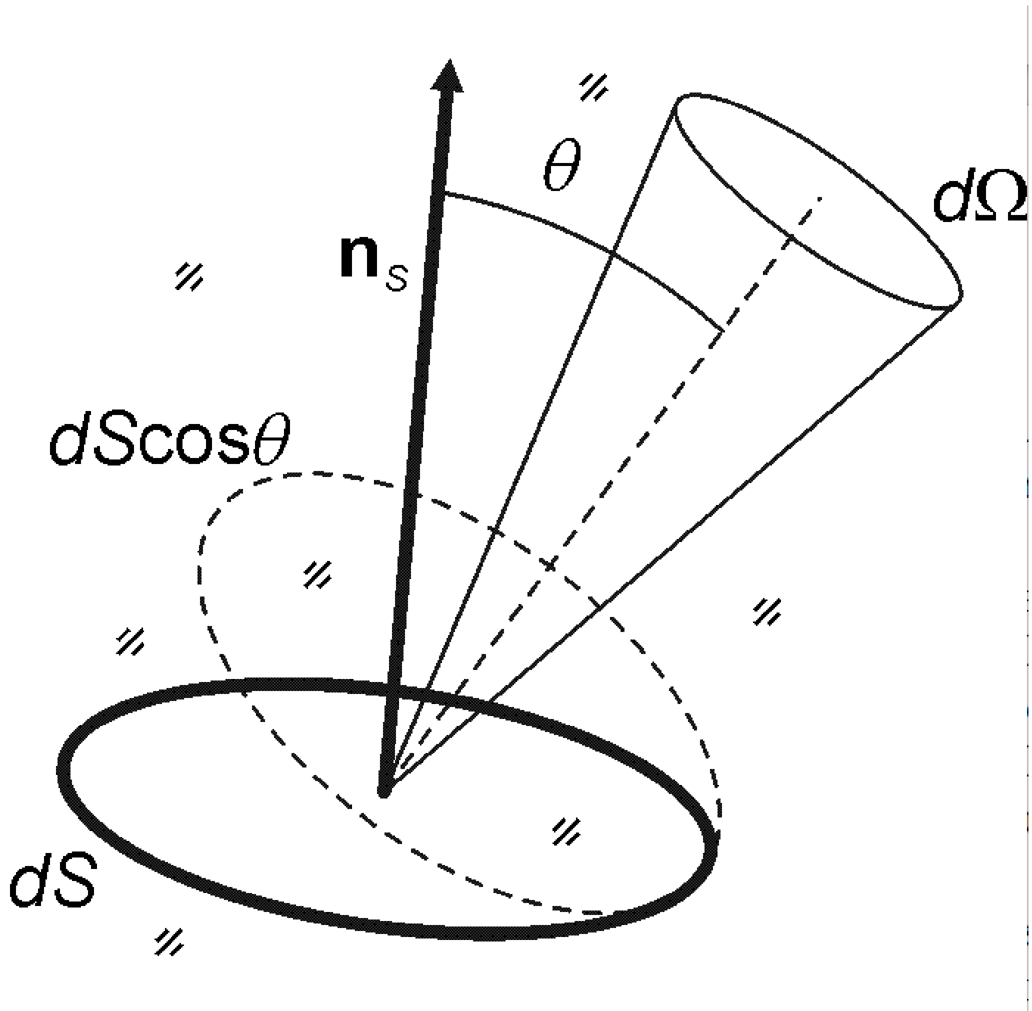

Figure 1.2: An example of throughput $A\Omega$. dS is an infinitesimal surface element whose integral is A.dΩ is an infinitesimal solid angle element whose integral is Ω. Figure adapted from [2].

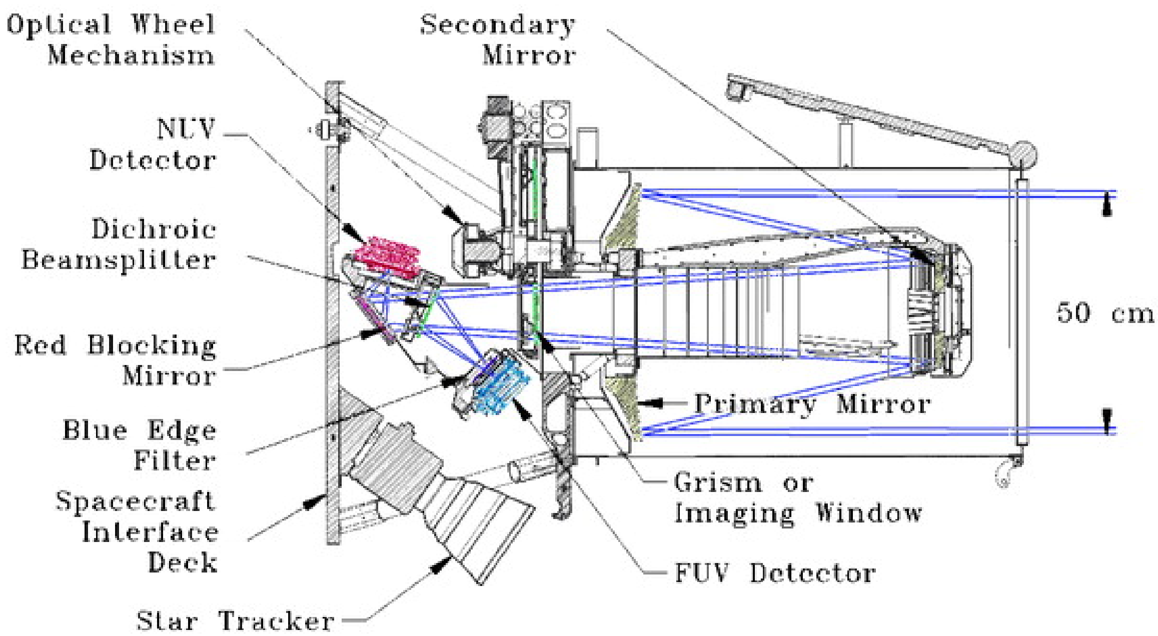

Figure 1.3: Schematic GALEX instrument design. The optical path is outlined in blue. Figure adapted from [3].

the importance of brightness sensitivity when designing an intensity mapping instrument. However, Fabry-Perot spectrometer can only obtain the spectrum within a small wavelength range at a time, making it inefficient for intensity mapping.

The Galaxy Evolution Explorer (GALEX) satellite is similar to the telescope I built [48]. It is designed to investigate how star formation in galaxies evolved from the early Universe up to the present. GALEX can obtain direct images in the near-UV band and the far-UV band, and obtain low resolution spectra using a grism. The spectroscopic survey had a goal of covering 5 square degrees. The GALEX instrument design is shown in Fig.1.3, where the grism can be placed in front of the detector [3]. Its CaF_2 grism forms simultaneous spectra of all sources in the field on the detector. Since many spectra may overlap, the GALEX rotates the grism to different position angles and conduct repeat observations of the same field. These grism-dispersed images are combined to eliminate confusion as shown in Fig.1.4 [4]. The best non-overlapping spectrum for each source is then extracted from these images. Although the GALEX and the GSTI telescope I built in the thesis both take advantage of grism, GALEX only extracts spectra of isolated point sources based on the conventional idea of grism spectroscopy. However, my GSTI is aiming at reconstructing the spectra of every pixel in the field even for weak sources via grism spectrotomography.

The Spectro-Photometer for the History of the Universe, Epoch of Reionization, and Ices Explorer (SPHEREx) is a proposed all-sky survey satellite that can map Lyα

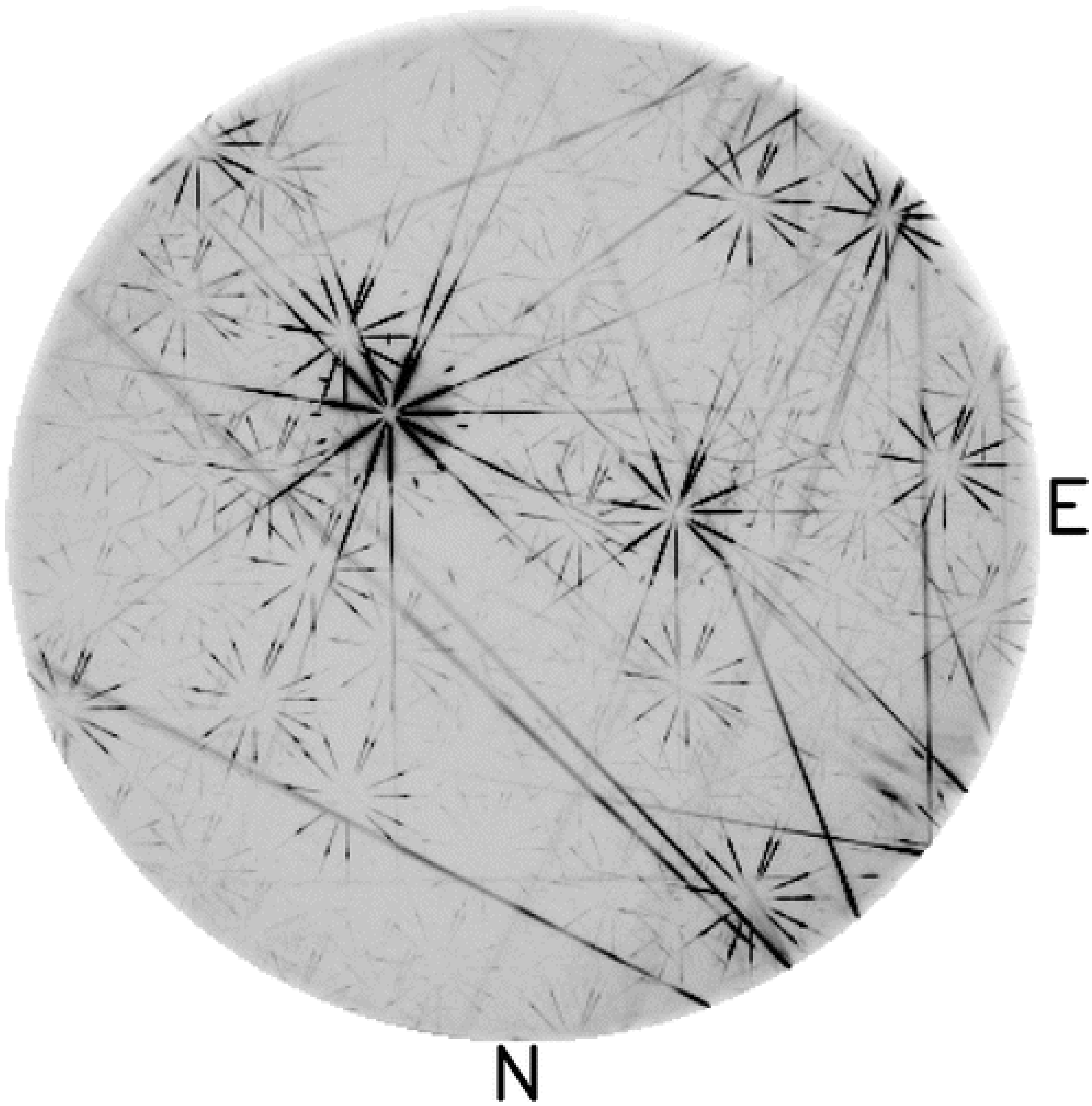

Figure 1.4: A combined image of GALEX grism spectra collected with multiple grism position angles. Each spectrum spins around its own undeviated wavelength point as the grism rotates. Figure adapted from [4].

line at high redshifts $5.2 < z < 8$. Its sensitivity will enable the satellite to detect Lyα fluctuations at S/N$\approx$10 during reionization at $z > 6$ [49]. This next generation telescope can investigate scientific issues such as cosmic inflation, interstellar and circumstellar ices, and the extragalactic background light [50].

1.4 Spectrotomography

Spectrotomography is a class of techniques that applies tomographic principles to obtaining the spectra of spatially extended objects. Several techniques and mathematics are discussed in papers [51, 52, 53, 54, 55]. This thesis focuses on a telescope I built, the Grism Spectrotomographic Imager (GSTI), using Grism Spectrotomography (GST) technique to achieve our goal of high throughput intensity mapping. GSTI has a rotating grism in front of the camera and takes a set of grism-dispersed images as the grism rotates. This process is very similar to X-ray computed tomography or Computerized Axial Tomography(CAT) scan, where source and sensor rotate about the object to obtain a set of projected images. In GST, the grism rotates as if sources and sensor rotate about the hyperspectral data cube to obtain the projected images set. The object reconstructed in CAT is the organ or tissue of the patient, while the object reconstructed in spectrotomography is the spectrum of every pixel. The imaging process is described by Radon transform or X-ray transform mathematically [56, 57, 58]. Further studies and reconstruction algorithms are grounded on these transforms.

Due to its close relations with the CAT scan, spectrotomography usually borrows tomographic reconstruction techniques from medical imaging [59, 60, 61]. Reconstruction is either based on inverting the transform equations such as filtered back projection and direct Fourier method [62, 56], or on solving a system of linear equations that lead to algebraic reconstruction techniques [63, 64]. I developed a new technique for GSTI which implements the basic back projection along with PSF deconvolution. The new technique borrows ideas from both direct inversion and algebraic reconstruction. It is a special filtering in Fourier space after basic back projection.

1.5 Thesis Overview

The thesis is outlined as follows. In Chapter.2, I compare 5 most common types of integral field units (IFU): fiber, lenslet array, image slicer, imaging Fourier transform spectroscopy, grism spectrotomography. The grism spectrotomography is the technique I explored in the thesis. In Chapter.3, three major sources of foreground contamination are discussed: continuum foreground, line contamination, and bright stars. I propose a masking and filtering scheme to remove star foreground. In Chapter.4, I describe the telescope Grism Spectrotomographic Imager (GSTI) I built, and show sample images from the telescope. In Chapter.5, I describe the grism imaging process as the projection from hyperspectral data cube and propose a two-step reconstruction algorithm. The first step, back projection algorithm, is analyzed in details. In Chapter.6, I discuss the second step of the reconstruction algorithm: point spread function (PSF) deconvolution. Direct Fourier deconvolution and Richardson-Lucy (RL) deconvolution are compared through simulations. In Chapter.7, I show three experiment results using the GSTI. The targets are HeNe laser, LEDs and stars respectively. In Chapter.8, I summarize the entire thesis and suggest some future work based on the analysis.

Chapter 2

Integral Field Spectroscopy Overview

There are a few methods widely used in integral field spectroscopy (IFS), and they are different mainly by the integral field units (IFU) that are used. I will compare their advantages and disadvantages here, and then discuss their suitability for wide field Lyα intensity mapping.

In this Chapter, I discuss five common types of IFU: fiber, lenslet array, image slicer, imaging Fourier transform spectroscopy, and grism spectrotomography. I describe how they work and show examples of their application. I use the GSTI I built to compare with other major telescopes. By comparing different IFS techniques, I show that imaging Fourier transform spectroscopy and grism spectrotomography are two techniques especially suitable for high throughput intensity mapping.

2.1 Fiber IFS

A bundle of optical fibers in the focal plane of a telescope covers the spatial region of interest and transfers the incident light to the slit of a spectrograph. The flexibility of fibers allows people to obtain the spectrum for all fibers simultaneously with one or more slits [65]. A major problem with fiber optics is that the sampling is not contiguous because there are gaps between each fiber on the focal plane. And focal ratio degradation (FRD) due to inefficient fiber is another problem. FRD describes the fact that incoming light cone is smaller than the outcoming light cone, as shown in Fig.2.1 [5]. And the outcoming light is partially lost if the light cannot go through the optics following the fiber. It is generally caused by waveguide scattering and mechanical deformation due to bending and surface irregularities. These two disadvantages can be overcome using lenslet arrays, which are discussed below.

The IFUs for SDSS-IV survey MaNGA (Mapping Nearby Galaxies at APO) are examples of hexagonal dense packing of fibers [66], as shown in Fig.2.2. Their sizes range from 19 to 127 fibers and reach a fill fraction of 56%. It achieves a high

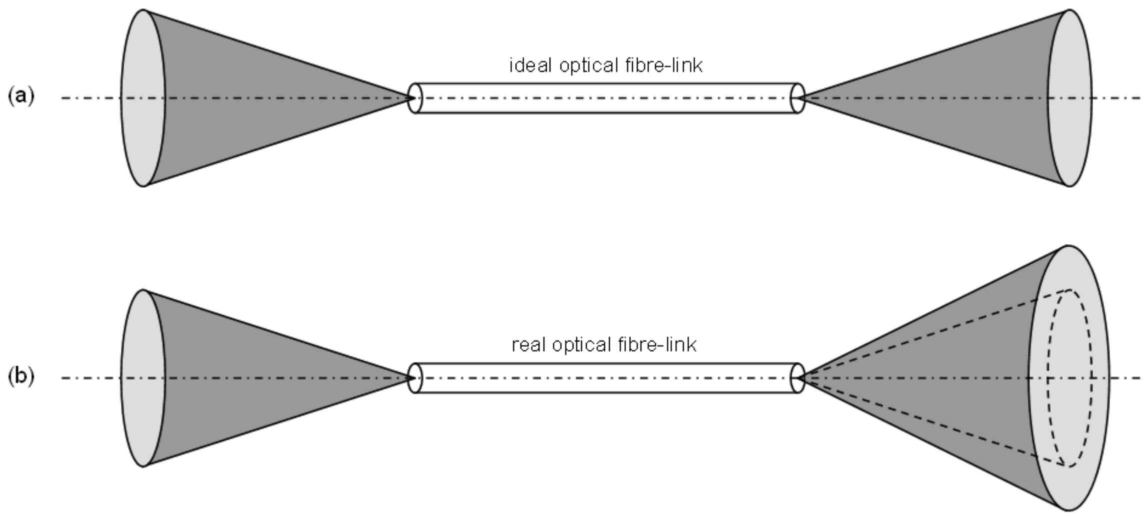

Figure 2.1: Schematic illustration of focal ratio degradation. The top figure shows an ideal fiber with no FRD losses, whereas the lower figure represents a real fiber with a wider output cone than its input cone due to FRD losses. Figure adapted from [5].

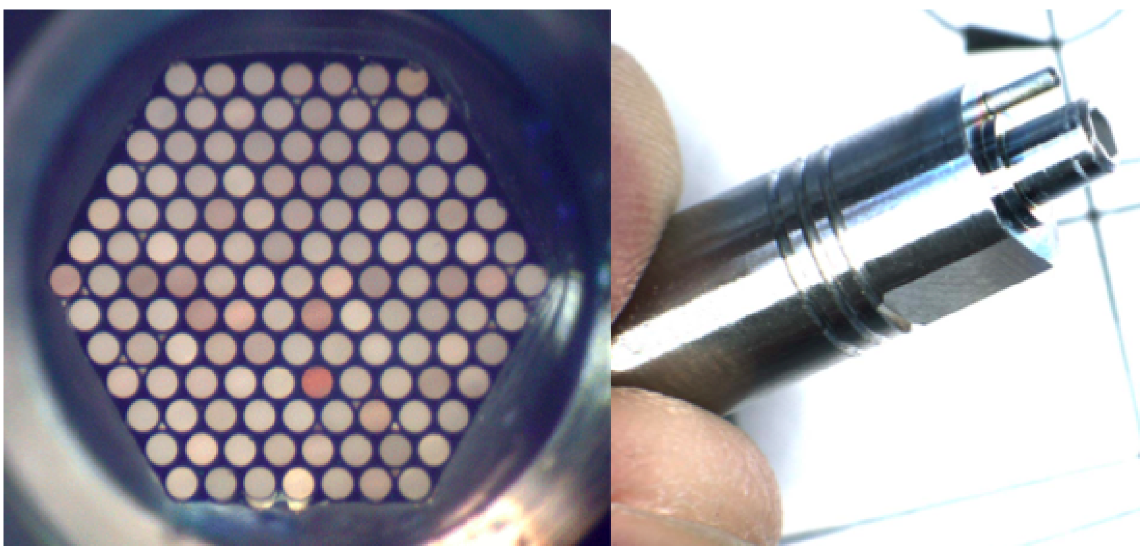

Figure 2.2: Close-up of a MaNGA 127-fiber dense packing IFU (left) and ferrule housing that holds the IFU (right). Figure adapted from [6].

transmission and low FRD by maintaining the fiber cladding and buffer layers intact, polishing the surface, and adding a multilayer AR coating to the input and output surfaces. The fiber they are using has 120μm core diameter, or $2''$ on sky, and reaches the spectral resolution at $R = \lambda/\Delta\lambda \sim 2200$ with BOSS spectrographs. The MaNGA has a maximum etendue of $4.5 \times 10^{-4}\text{m}^2\text{deg}^2$ at wavelength $\lambda = 500$nm [67].

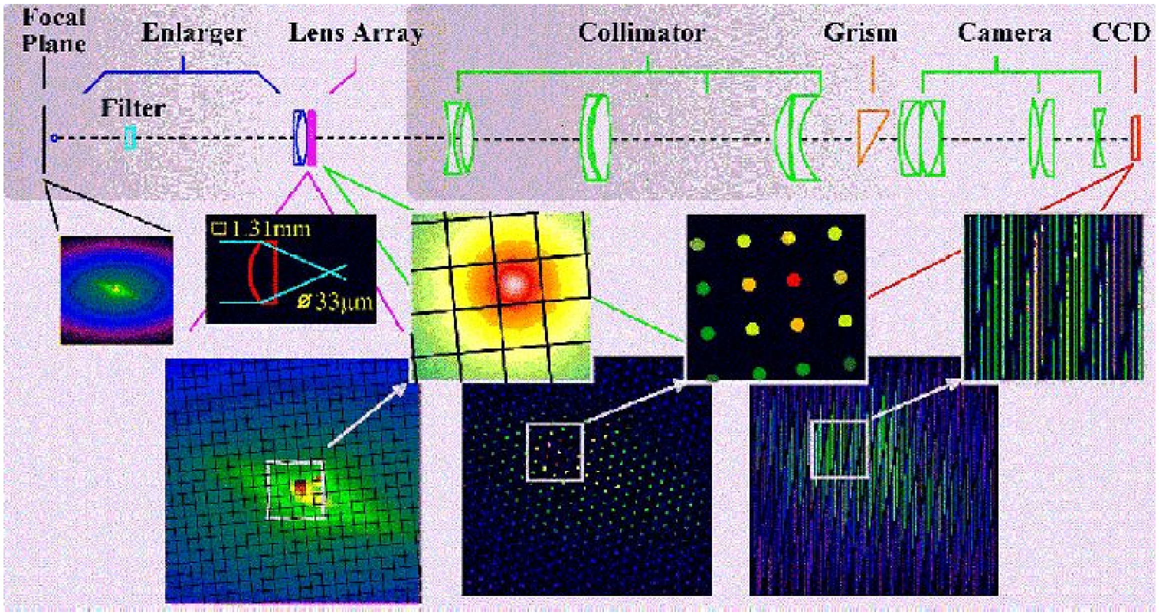

Figure 2.3: Optics design of Sauron: Elements are listed from focal plane(left) to detector plane(right). Figures shown from left to right are the image of a galaxy seen at the entrance of MLA, at the exit of MLA and at the detector plane respectively. Figure adapted from [7].

2.2 Lenslet Array IFS

The incident light is split up by microlens array (MLA) and focused into small dots. These small dots are fed into spectrograph and dispersed into spectra. SAURON is an integral field spectrograph that uses lenslet array with grism, and its optics design is illustrated in Fig.2.3 [7]. The final spectra of each small dots are non-overlapping vertical stripes in the rightmost pictures. Notice that the final spectra from different dots are not overlapped, because the dispersion direction is not parallel with the lens array alignment. This is achieved by rotating the MLA or the grism to a different angle about the optical axis. MLA can achieve contiguous sampling because there are no gaps between lenses. MLA also avoids FRD problem since light does not go through the fiber. However, the length of spectra is restricted to be short enough that they do not overlap with each other and a lot of pixels on the sensor are not used, which indicates inefficient use of the sensor.

But MLA can be used together with fibers, which is demonstrated by the Gemini Multi-Object Spectrographs (GMOS) IFU on the Gemini-North telescope [68], similar to Fig.2.5. The fibers are fed to a spectrograph and allow the image area to be distributed on the slit of a spectrograph. Microlenses also slow the telescope focal beam so that FRD can be minimised.

2.3 Image Slicer IFS

Image Slicer, as the name itself indicates, slices the image by using mirror segments that are at slightly different angles. These slices of the image are then realigned into a long slice by other mirrors and sent to the slit of a spectrograph. The spectra obtained from the long slice of the image are rearranged to obtain the original hyperspectral data cube. As an example, image slicer is proposed to Gemini telescope in both the optical band and the infrared band [8]. Its optics design is shown in Fig.2.4. Near-Infrared Integral Field Spectrometer (NIFS) is the Image Slicer commissioned on Gemini North telescope [69].

Image slicer also has the advantage of contiguous sampling and avoiding FRD caused by fibers. Since the reflecting mirrors are achromatic and can be cooled down to cryogenic temperatures, it applies to infrared well. However, image slicer requires the spectrograph to have a long slit and encounters engineering problems during fabrication, such as a large number of carefully aligned mirrors required. A comparison of the first three main methods is presented in Fig.2.5.

2.4 Imaging Fourier Transform Spectroscopy

Imaging Fourier Transform Spectrometer (IFTS) is essentially a Michelson interferometer with a moving mirror in one arm. The interferometer acts as an optical filter with a transfer function that depends on the setting of the Optical Path Difference (OPD) between two arms. Observations are made at evenly spaced OPD settings by moving the mirror with equal distance steps, creating the raw data set called interferogram as shown in Fig.2.6. The interferogram is then Fourier transformed to yield the spectrum of each pixel. Several IFTS systems are used for ground based telescopes [10], such as SpIOMM [70] and BEAR [71].

As the OPD step size of the IFTS system is selected manually, it is usually set to half of the shortest wavelength of the band being observed according to the Nyquist sampling theorem. The IFTS can be applied in the dual-port mode as the detector accesses both output beams, which achieves the optimal efficiency by collecting every photon from a telescope. SITELLE, the successor of BEAR and SpIOMM, is an example of the dual-port design IFTS [72]. A potential downside of IFTS is the difficulty in assembling a large IFTS with large detectors. Furthermore, the dead periods during each reading could also slow down the observation due to multiple readouts.

2.5 Grism Spectrotomography

Grism spectrotomography has the multiplex advantage that achieves high throughput with minimum cost. A grism that can rotate about its optical axis is placed in front

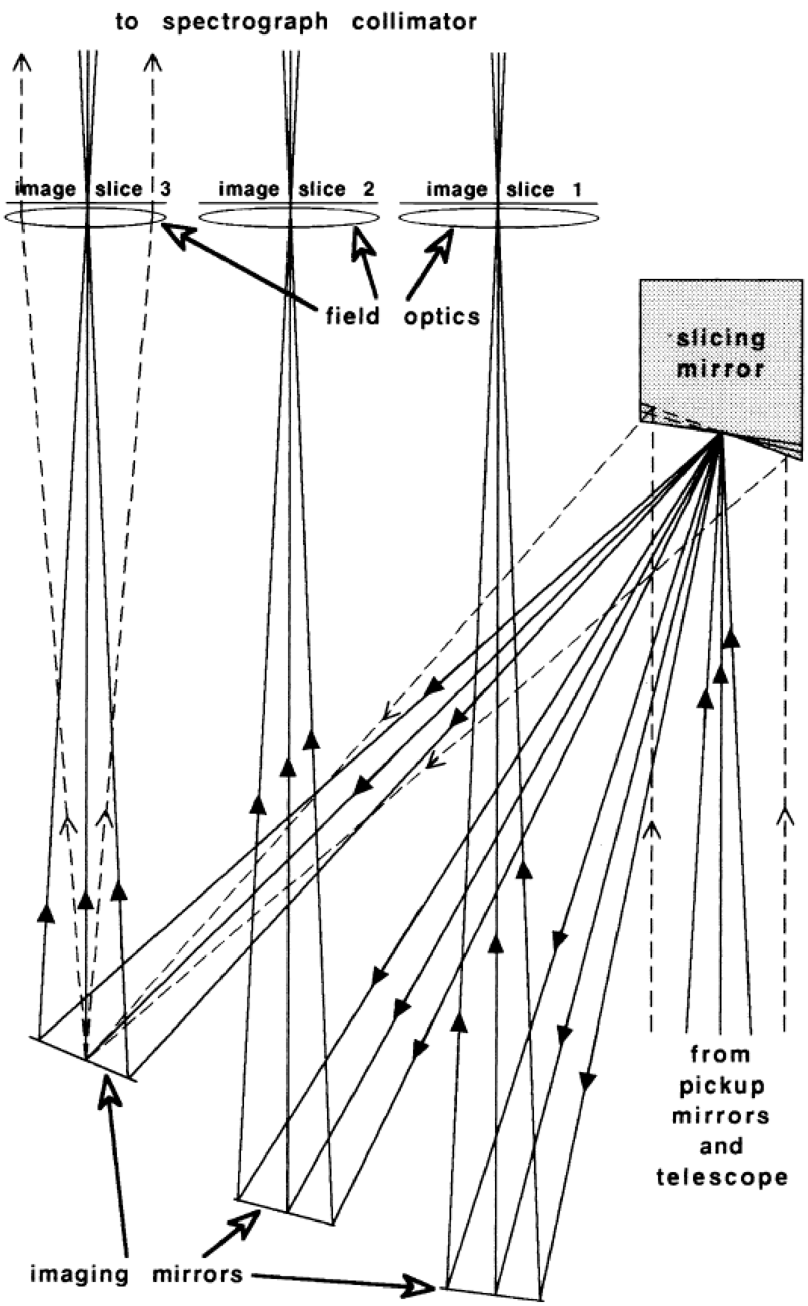

Figure 2.4: Schematic Image Slicer: Rays from telescopes are reflected to different imaging mirrors according to different slices, and then sent to spectrograph. Figure adapted from [8].

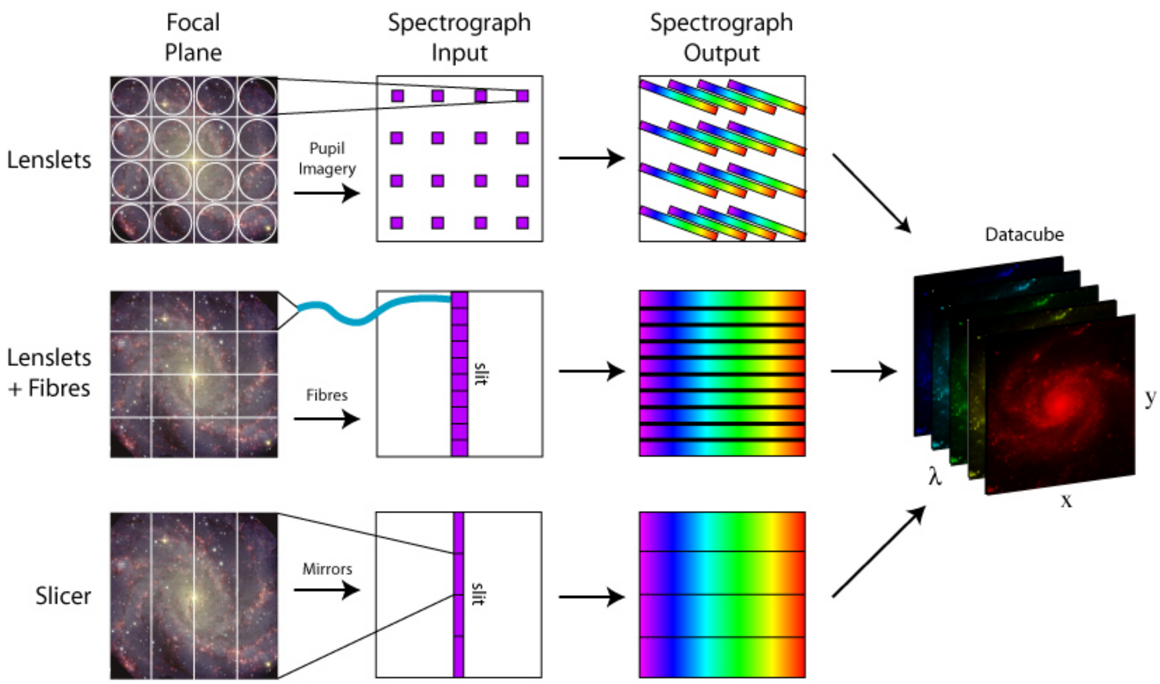

Figure 2.5: Comparison of three major IFS techniques: Lenslets, Fibers with lenslets and image slicer. Credit: M. Westmoquette, adapted from Allington-Smith et al. 1998 [9].

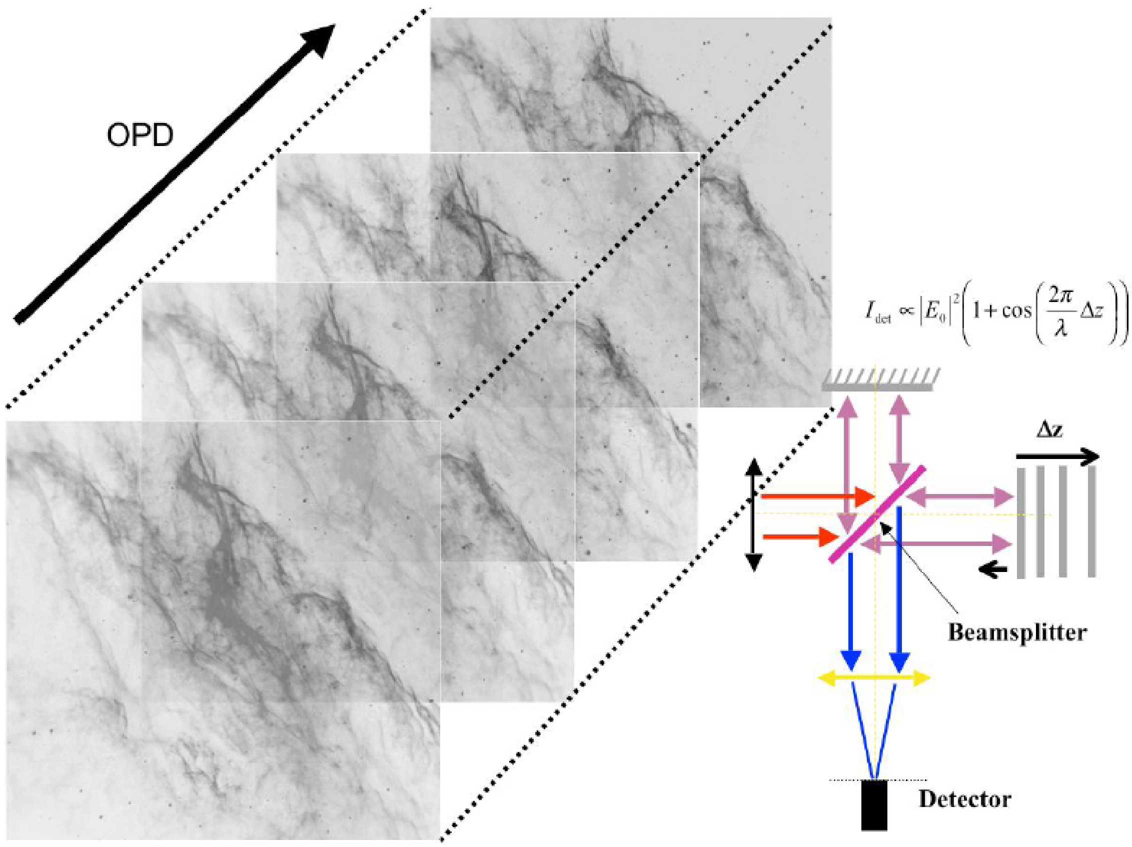

Figure 2.6: Schematic IFTS: At each step of the Michelson interferometer OPD, an image of the entrance field is recorded on the 2D-detector array, creating the interferogram. Figure adapted from [10].

Characteristic	Fiber	Lenslet	Image Slicer	IFTS	GST
Simple optics	✓				✓
Contiguous sampling		✓	✓	✓	✓
Focal ratio degradation	✓				
High throughput		✓	✓	✓	✓
Limited spectrum length		✓			
Inefficient use of sensor		✓			
Intrinsically achromatic			✓		
Multiple exposure				✓	✓
Information loss					✓
Computationally intensive					✓
Multiplex advantage				✓	✓
Suitable for wide field spectroscopy				✓	✓

Table 2.1: Comparison between different IFS techniques

of the imaging camera. A set of grism-dispersed images are taken at each angular step as the grism rotates. The set can be treated as the projection of a hyperspectral data cube, which is then reconstructed via tomographic techniques to 3D hyperspectral space. A schematic GST instrument is displayed in Fig.4.1. Unlike the traditional grism spectroscopy that only resolves the spectra for multiple objects, GST is able to yield the spectrum for every pixel within the field of view without isolation of individual source.

Grism Spectrotomography utilizes all the photons within the hyperspectral cube at every grism orientation, ensuring a large throughput and thereby a high sensitivity. Another advantage of GST is its easy installation. It works on any existing telescopes by inserting only one piece of grism and rotation stage. However, the reconstruction is subject to loss of information and expensive computation as described below.

2.6 Suitable Techniques for Wide Field Lyα Intensity Mapping

Table.2.1 provides a table comparison of advantages and disadvantages for each IFS technique. Overall, the spectrograph must be able to map a large field of view to perform wide field Lyα intensity mapping. This goal should be achieved at an affordable cost and a reasonable size of the instruments. The diameter of BAO ring is 9.3°, which gives the lower limit of our FOV in order to contain the whole ring.

The image slicer needs a large number of slicing mirrors and slits to slice a large region and obtain the spectra. For example, given a spatial pixel size $5'' \times 5''$ and $5 \times 5\mu$m pixels, it requires a total slit length of $20.97m$ to achieve the FOV $2.8° \times$

2.8°. The Wide Field Spectrograph (WiFeS) that is developed in Australian National University achieves only a field of view $38'' \times 25''$ using image slicer technique and two 4096×4096 pixel CCD detectors [73]. Thus it is unrealistic to use image slicer for wide field spectroscopy.

Similar problems exist for fiber IFS, because we need the same number of fibers as the number of pixels. Assuming the same pixel sizes $5 \times 5\mu$m in focal plane as above, 4 million fibers and 20.97m long slits are required to achieve the FOV $2.8° \times 2.8°$. Another example is Visible Integral-field Replicable Unit Spectrograph (VIRUS) for Hobby-Eberly Telescope Dark Energy Experiment (HETDEX). VIRUS consists of 150 identical spectrographs and 33600 fibers, but only covers a field of $4.6 \times 10^{-3}\text{deg}^2$ [74, 75].

For lenslet array, it faces the same problem of too many fibers if it is used together with fiber. However, if it is applied independently of fibers, there are no requirements for long slits and fibers. Instead, the bottleneck is the number of lenslet in microlens array, which is equal to the number of pixels. This number is approximately 2 million using the above assumption, and it is hard to realize. I also mentioned in Section 2.2 that MLA does not use all the pixels on the sensor and make thus requires more sensors than other techniques.

Gratings and slits both suffer from requiring multiple pixels to resolve the spectra from the sources in one pixel. In comparison, IFTS solves the problem through interferometry and GST solves this problem through spectrotomography. In addition, IFTS and GST can conveniently set its FOV by adjusting the focal length and sensor size.

2.7 Conclusion

IFTS and GST are two most cost-effective and high-throughput techniques for wide field Lyα intensity mapping. Their multiplex advantages enable them to observe a large field without using multiple spectrographs simultaneously. In contrast, fibers, lenslet arrays and image slicers all require extra spectrographs to perform wide field intensity mapping. Furthermore, GST's optics design is simpler than IFTS. I focused on GST in my thesis. I built a prototype GSTI with the Nikon D800 camera with 200mm focal length and 30mm $\times$ 24mm sensor. It achieves an FOV of 3° diameter. The details of the instrument are discussed in Chapter.4.

Chapter 3

Foreground contamination in Intensity Mapping

Lyα intensity mapping suffers from three major sources of foreground contamination: continuum foreground, line contamination, and bright stars. I will discuss the effects of these three sources of foreground contamination and methods to remove them.

In this Chapter, I first discuss the spatial continuum foreground components and their contributions to the diffuse night sky brightness. Then I introduce some standard procedures to remove the continuum foreground and calibrate the telescope. I also discuss line confusion for Lyα intensity mapping and the ways of dealing with it. Finally, I focus on star foreground that can affect the mapping and power spectrum of Lyα sources. And I propose a masking and filtering scheme that can retrieve Lyα fluctuations in large scale. It also provides insights on the design of an intensity mapping instrument.

3.1 Continuum Foreground Components

For ultra-violet and optical bands, the continuum foreground refers to the night sky brightness. The contribution to the diffuse night sky brightness can be formally described as the following formula [1]:

$$I_{nightsky} = (I_A + I_{ZL} + I_{ISL} + I_{DGL} + I_{EBL}) \cdot e^{-\tau} + I_{SCA} \tag{3.1}$$

where $I_{nightsky}$ is the total diffuse brightness of the sky, I_A is the airglow, I_{ZL} is the zodiacal light, I_{ISL} is the integrated starlight, I_{DGL} is the diffuse galactic light, I_{EBL} is the extragalactic background light. These contributions are attenuated by atmospheric extinction with an extinction coefficient τ. Furthermore, the tropospheric scattering of these sources adds another component I_{SCA} to the total brightness. The fraction of individual contribution to the total sky brightness in u band is given in Fig. 3.1. The source of each component is shown in Fig. 3.2. Each component will

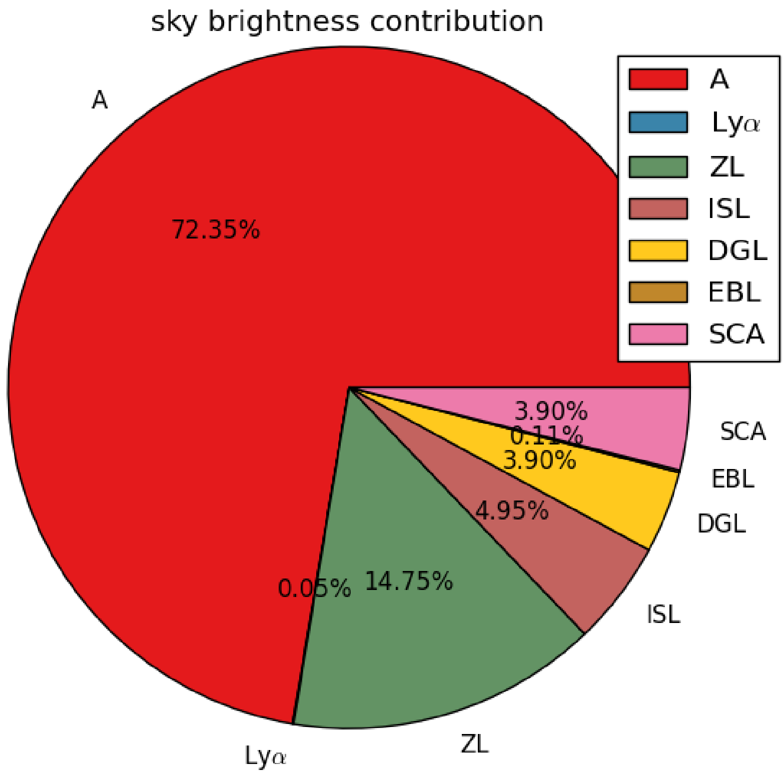

Figure 3.1: Approximate brightness contribution from each source.

be specified in the following paragraphs.

3.1.1 Airglow

Airglow emission can appear in ionospheric E layer (∼90km), F region (∼180km), or Lyα and Hα in the Geocorona. According to Broadfoot & Kendall [76], the average airglow intensity is approximately 0.6R/Å $= 2.6 \times 10^{-9}$W m^{-2}nm^{-1}sr^{-1} in u band. This result is based on the observation at Kitt Peak near zenith and within 30° of the galactic pole. There are several features about airglow. First, airglow depends on zenith angle z and is usually increased from the zenith to the horizon. This relation is given by the *van Rhijn function*.

$$I(z)/I(zenith) = \frac{1}{\sqrt{1 - [R/(R+h)]^2 \sin^2 z}} \tag{3.2}$$

where R is the radius of earth, h is the height of homogeneous emitting layer and z is the zenith distance or the complement of altitude.

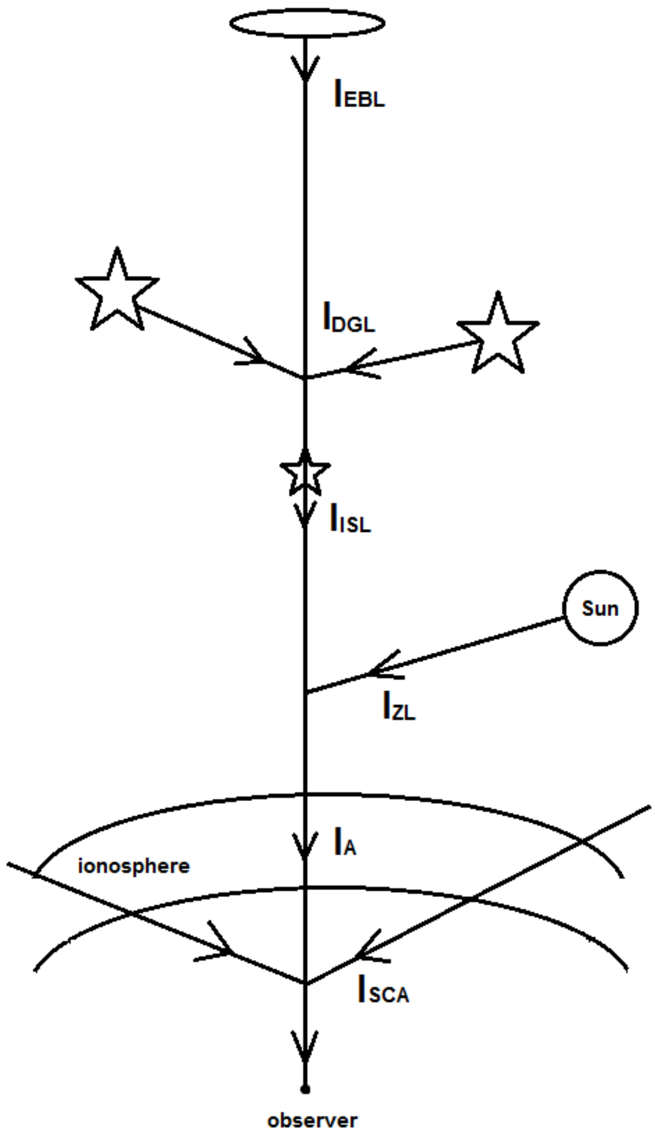

Figure 3.2: Schematic source of night sky brightness.

Second, Airglow can vary enormously with time due to atmospheric changes and solar activity. Third, the upper atmosphere can interact with interstellar neutral atoms, or low earth orbit artificial satellites, producing continuum emission.

3.1.2 Zodiacal Light

Zodiacal light is formed due to sunlight scattered by interplanetary dust particles in ultraviolet, visual and near infrared region. Its brightness is usually a function of wavelength, heliocentric distance, viewing direction and the position of the observer relative to the interplanetary plane. It is shown in Table 19 of Leinert's paper [1] that zodiacal light brightness at elongation $\epsilon = 90°$ around 300nm is 0.53×10^{-9}W m^{-2}nm^{-1}sr^{-1}.

3.1.3 Integrated Starlight

This is the light from unresolved stars contributing to the sky brightness. Usually, it is dominated by hot stars and white dwarfs at the ultraviolet, main sequence stars at visual wavelengths, and red giants in the infrared [77]. In the pie chart Fig.3.1, the total starlight brightness $I_{ISL} = 0.302 \times 10^{-9}$W m^{-2}nm^{-1}sr^{-1} comes from the brightness measurement at south galactic pole [1, 78, 79]. I choose south galactic pole integrated starlight brightness as a lower bound and estimate for my intensity mapping experiment, because it is intended for higher galactic latitude to avoid light from stars.

3.1.4 Tropospheric Scattering

Tropospheric scattering is another crucial contribution to the night sky brightness, whose scattering sources are mainly airglow, zodiacal light, and integrated starlight. The model of scattering usually assumes first order Rayleigh scattering and Mie scattering from a uniform and unpolarized source in the atmosphere. The intensity is a function of zenith distance for various extinction values. Leinert [1] mentioned the scattering is usually in the order of $10 - 100$ S$_{10}$ ($0.14 - 1.4 \times 10^{-9}$W m^{-2}nm^{-1}sr^{-1} in U band), about 15% or more of the zodiacal light and 10- 30% integrated starlight.

3.1.5 Diffuse Galactic Light

Diffuse galactic light (DGL) is the diffuse component of the galactic background radiation produced by scattering of stellar photons by dust grains in interstellar space. Dust particles' infrared thermal emission is known as "cirrus" due to IRAS observations. A comprehensive measurement of DGL in the visual band is conducted by Pioneer 10 probe. It carried out an all-sky photometric mapping in two wavebands centered near 440 nm and 640 nm from beyond the asteroid belt, where the zodiacal light can be neglected. Based on the results of Leinert's paper[1], the dark region at high galactic latitude ($> 50°$) has an intensity around 10 $S_{10} = 0.14 \times 10^{-9}$W m^{-2}nm^{-1}sr^{-1} centered at 440 nm.

3.1.6 Extragalactic Background Light

Extragalactic background light (EBL) in the visual band is believed to consist mainly of redshifted starlight from unresolved galaxies, from stars or gas in the intergalactic space, and from decaying elementary particles. Based on the results of Leinert's paper [1], the brightness from extragalactic background light is approximately 0.0057×10^{-9}W m^{-2}nm^{-1}sr^{-1} at 350 nm.

3.1.7 Remove Continuum Foreground

As can be seen from Fig.3.1, the estimated Lyα signal is dim compared to other components of the sky brightness. Some bright and time-variant components must be removed before we can effectively detect Lyα signal. Here are standard procedures for imaging data reduction adopted by Dragonfly telescope [80], which can also be applied to the GSTI.

- Dark frames are taken throughout each night due to slight variation and may be subtracted from the source and sky measurements. They are taken using the same ISO, exposure time, and temperature as the normal images, but with the lens cap on. A large number of dark frames should be averaged together with a median algorithm to reduce noise. Usually, all dark frames should have the same duration as the source and sky measurements to which they will be applied.

- Bias frames are complementary to dark frames, which have a charge integration time but in darkness. They are taken using the same ISO and temperature as the normal images, but with fastest shutter speed and lens cap on. Bias frames contain electrical noises the camera generates.

- Flat-field calibration frames are necessary to remove pixel-to-pixel variations. Ideally, the flat field should be illuminated in the same way as the image to which it will be applied. A series of flat-field frames are taken at the beginning of each night, slightly offset from one another. They will be combined using a median filter or clipping algorithm to remove stars, which provides a very good flat field. Sky-frames can also serve the purpose of flat-fielding.

- Dithering is a strategy to minimize the effects of undersampling and to reduce the effects of hot pixels, by offsetting the telescope between exposures by either integer or subpixel steps. Some resolution lost due to sampling by pixels that are not small compared to the point spread function can be recovered through independent exposures with sub-pixel offsets. Individual images taken with subpixel offsets can be combined to form an image with higher spatial resolution than that of the original images, where 2-4 dither positions are recommended for this case. Dithering by an integer number of pixels can also reduce hot pixels, while dithering on scales of several pixels can help to smooth out pixel-to-pixel variations in detector sensitivity. Pixel-to-pixel errors in flat-fielding average out, thus allowing a higher signal-to-noise by combining data taken with integer pixel offsets. The algorithm for combining dithered images is Variable-Pixel Linear Reconstruction, or informally “Drizzle”, which can weigh input images according to the statistical significance of each pixel, and removes the effects of geometric distortion on both image shape and photometry [81, 82]. Dithering can also be used to make the sky and target frames.

- After dark subtraction, flat-fielding, and dithering, Dragonfly also corrects each image for foreground total sky brightness with a model. The model identifies the brightness distribution across the entire field of view at the site due to light pollution from nearby cities, foreground emission and scattering [83]. Since the sky brightness is not uniform across the sky, it can be subtracted with a tilted plane based on the theoretical model. Besides, Dragonfly identifies the large scale background in the image determined with SExtractor. It is then fitted a third-order polynomial and subtracted from the image.

Besides data reduction, there are several other techniques to remove continuum foreground. Shaver et al. discussed ways of correcting for diffuse galactic and extra-galactic foreground emissions by sufficient modeling and measurement [84]. There are also discussions focusing on their smooth frequency structure in a narrow bandwidth, higher spectral resolution and cross-correlation [85, 86, 87, 88, 89]. Continuum foreground removal is a well-studied problem for 21 cm intensity mapping, and most of the techniques can be adapted for Lyα intensity mapping.

3.2 Line Foreground

Line foregrounds are caused by spectral lines other than Lyα redshifted to the same observing band, where it is hard to separate the signals. 21 cm intensity mapping is not contaminated by this issue because there are few lines at such long wavelength. But Lyα suffers from line foregrounds at various redshifts. For Lyα intensity mapping at moderate redshift ($z = 2 \sim 4$), some possible line foregrounds are O II ($372.7nm$), O III ($500.7nm$) and Hα ($656.3nm$).

One method to remove the line foregrounds is to cross-correlate two intensity maps at different wavelengths, or one intensity map with another LSS tracer [90]. This works because only the target signals in the two maps are correlated, while the foregrounds in either map are uncorrelated. Comaschi et al. showed cross correlation between diffuse Lyα line emission and Subaru Hyper Suprime Cam Lyα emitters could recover Lyα line intensity [91]. However, there are two disadvantages of this method. The first is that observing two signals is expensive and not straightforward. Second, it is not well studied how to reconstruct the auto power spectrum from the cross correlation, indicating a possible loss of information during cross correlation [92].

Masking bright pixels is another method to remove foregrounds. Usually, the intensity mapping signal becomes weaker with redshift, so that lower redshift lines are more problematic than higher redshift lines. Since galaxy masses are larger at lower redshift, foreground line sources tend to be brighter than target sources. This implies that the brightest pixels are more likely to be foreground line sources. Therefore masking the brightest pixels can effectively reduce the line foreground contamination. Visbal et al. demonstrated that this technique could bias the target power spectrum [93]. Gong et al. demonstrated it is applicable to Lyα intensity mapping and discussed the projection effect of the foreground power spectra [92]. Breysse et al. showed that foreground contamination is effectively dropped below the Lyα signal in their simulation after masking 3% of the pixels. They also stated that the shape of the power spectrum is not affected much after masking, although the amplitudes of the power spectrum are lowered. So after masking, much of the cosmological information is preserved, while the astrophysics information is lost [94].

3.3 Star Foreground

3.3.1 Star Foreground Contamination

All the stars brighter than Lyα can interfere with the Lyα signal during the intensity mapping experiment. The SDSS Data Release 13 catalog is used to estimate the brightness and the distribution of stars [95]. A field centered at (RA=180°, DEC=10°) with size $10° \times 10°$ is chosen for the simulation in this section. To compensate for the incomplete detection of SDSS, I correct the number of stars in each bin with the completeness curve shown in Fig.3.4. The completeness curve is estimated by comparing the number of stars found in Data Release 1 [96] to the number found in Classifying Objects by Medium-Band Observations (COMBO-17) survey [97]. Although Fig.3.4 shows the fractional completeness of stars in r band, I assume u band completeness curve has a similar shape because both bands have magnitude limits at 22. The measured star magnitude distributions before correction and after correction in u band are shown in Fig.3.3.

The SDSS catalog in the selected field contains stars from magnitude 10 to magnitude 30. On the bright side of the distribution, SDSS catalog is inaccurate because the point source saturates at magnitude 13 in u band. On the dark side of the distribution, SDSS catalog is incomplete because u band has a 5σ detection limit at magnitude 22.3 [23]. Fig.3.3 indicates that number corrections mainly apply to magnitude 22-24, and the number of stars begins to decrease when they are fainter than

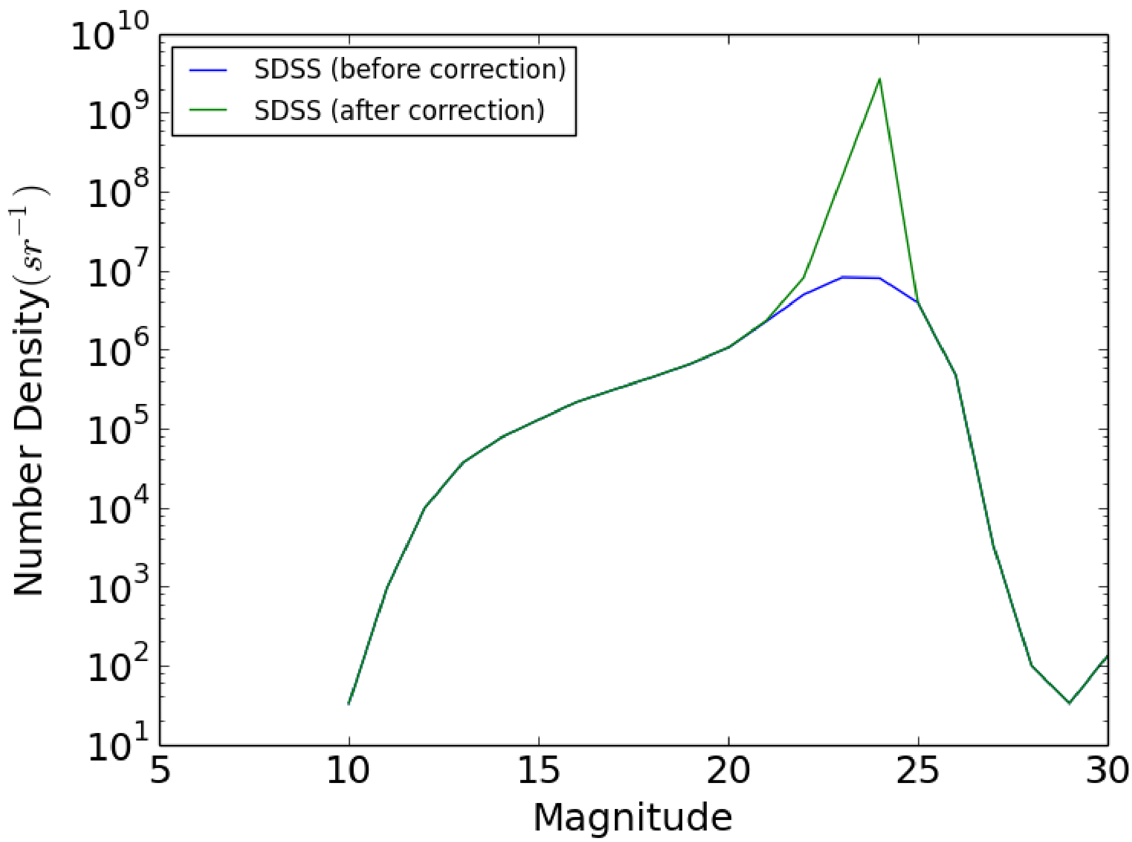

Figure 3.3: Luminosity function of SDSS stars in u band magnitudes before correction and after correction for completeness.

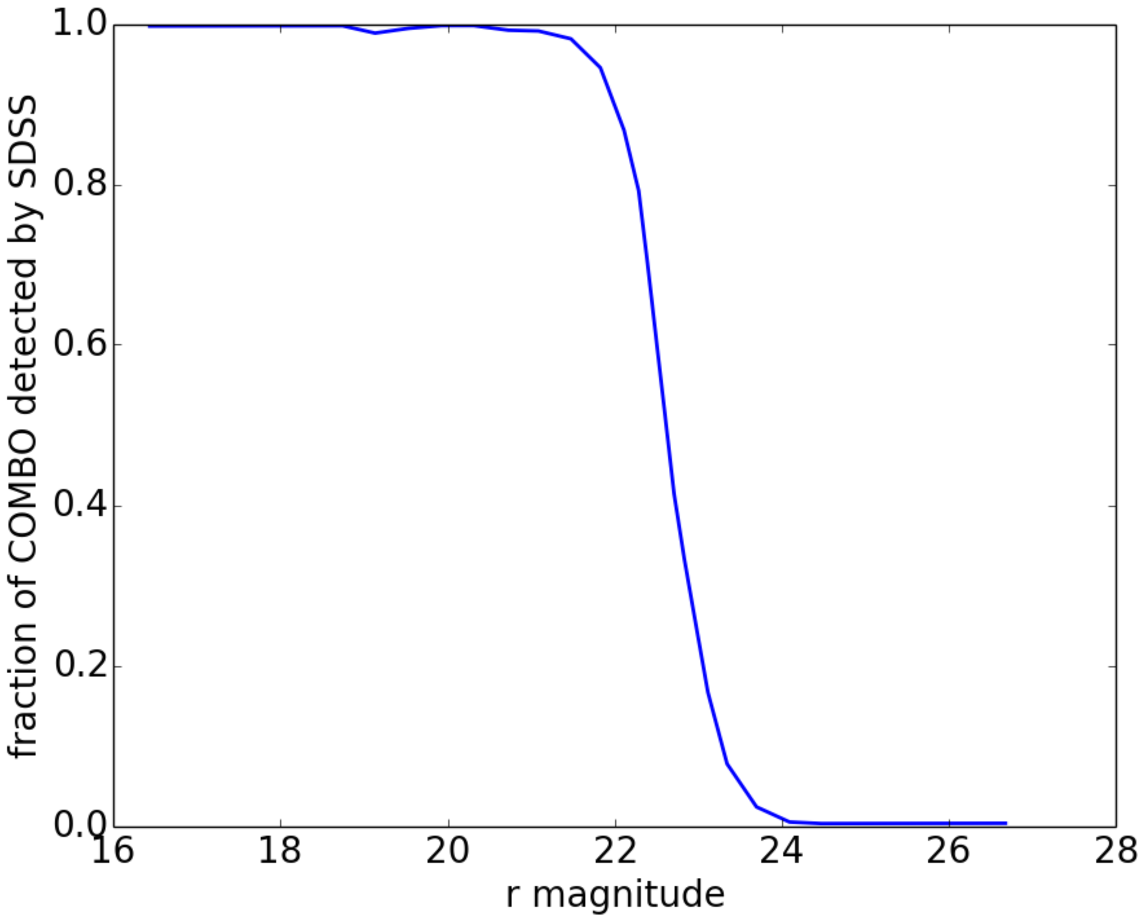

Figure 3.4: Fractional Completeness of Stars in SDSS r magnitude. Data adapted from [11].

magnitude 24 in u band. However, there may be more faint stars in the field due to detection limits. I will show later in this section that these extremely faint stars have negligible effect on the Lyα signals. I will use the corrected magnitude distribution as the best number estimate in the thesis.

The mean surface brightness of Lyα is 1.66×10^{-12}W m^{-2}nm^{-1}sr^{-1} [98], which is comparable with the average flux density from stars of magnitude 19. Therefore on average, stars brighter than magnitude 19 affect the direct mapping of Lyα signals. Since stars are unresolved point sources, fainter stars may yield greater flux than Lyα in their respective pixels depending on the pixel scale. For instance, the flux from Lyα is comparable with a magnitude 27 star inside a pixel of size $5'' \times 5''$. For the $74''$ pixels we will use at the end of this section, such dim stars make negligible individual contributions.

In addition to the detection of the Lyα signal, the Lyα power spectrum is also affected by the bright stars. Power spectrum describes the variance in the density field as a function of scale. It is the Fourier transform of the two point autocorrelation function. The correlations and structures of the density field can be analyzed through the power spectrum. The power spectrum from stars is calculated as if their spectra resulted from Lyα emitters at redshift z=2, and is compared with theoretical Lyα power spectrum. More specifically, a 3D flux density field was created and the SDSS field was used for the star distribution in the first two dimensions x, y. Then we generated uniformly distributed stars for number corrections based on Fig.3.3, assuming all stars are uniformly distributed on the 2D sky. For the third dimension, we used the identical M-star spectrum template [15] for all stars because M-star is the most common type. At a given redshift z, a tiny wavelength range $\Delta\lambda_{star}$ is chosen around the redshifted wavelength of Lyα $\lambda_{Ly\alpha}(z)$. The range $\Delta\lambda_{star}$ is then converted to the physical distance along the line of sight based on the redshift of Lyα. So I create a 3D flux density field that can be used to calculate the star power spectrum. The flux is in the unit of $I_\lambda\lambda$[nW m^{-2}sr^{-1}]. The synthetic field is $10° \times 10°$, which is turned into angular diameter distance based on Eq.3.3:

$$d_A^{flat} = \frac{\chi}{1+z} \tag{3.3}$$

where χ is the comoving distance out to an object at redshift z. Specifically, the physical size of this box is 307Mpc × 307Mpc × 307Mpc at $z = 2$.

The box is described by flux density $F(\mathbf{x})$, and the overdensity is:

$$\delta(\mathbf{x}) = F(\mathbf{x}) - < F(\mathbf{x}) > \tag{3.4}$$

where $< \cdot >$ is the average operator. Then the Fourier transform of the overdensity $\delta(\mathbf{x})$ is calculated by:

$$\delta(\mathbf{k}) = \int \delta(\mathbf{x}) \exp(-i\mathbf{x} \cdot \mathbf{k}) \mathrm{d}\mathbf{x} \tag{3.5}$$

And the power spectrum of the star flux density is [44]:

$$P(k) = \frac{1}{V} < |\delta(\mathbf{k})|^2 > \tag{3.6}$$

where V is the volume of the box. The calculated power spectrum from corrected SDSS catalog is plotted in Fig.3.5, together with the theoretical estimate of the Lyα power spectrum [45]. The error bars are estimated using jackknife method. We used flat sky approximation and ignored projection effect during the power spectrum calculation. Obviously, the power spectrum from stars is about three orders of magnitude greater than Lyα power spectrum at redshift $z = 2$. Stars will dominate the power spectrum if there are bright stars in the intensity map. There are also two curves indicating the power spectra of star flux after masking masking all stars brighter than $m_* = 12$ and $m_* = 13$ respectively. Although the power spectra after masking are still greater than Lyα power spectrum, they can be improved by filtering in the anisotropic power spectrum.

3.3.2 Masking Stars

Given the contamination on power spectrum, bright stars need to be masked for intensity mapping to recover the signal power spectrum. The question is how many stars should be masked? What magnitudes of stars should be masked? Can we use a current catalog for masking? To answer these questions, we again used the synthetic flux density field from the corrected SDSS catalog to simulate masking results.

Bright stars contribute more to the star power spectrum and affect the Lyα power spectrum. Most current catalogs are complete at these bright magnitudes. Thus there are no bright stars left in the sky when we mask stars according to these catalogs. The masking scheme is then straightforward: A threshold magnitude m_* is defined for masking, where all stars bright than m_* are masked in the field. Star power spectra can be compared for various masking threshold magnitudes m_*. And the best threshold magnitude can then be determined according to observation criteria.

Notice that stars are randomly located on the sky, while their spectra are not random. Thus the star power spectrum is anisotropic. The power spectrum has different shapes between modes perpendicular to line-of-sight $k_\perp = \sqrt{k_x^2 + k_y^2}$, and modes parallel to line-of-sight $k_\parallel = k_z$. It is helpful to compare the power spectrum in terms of $P(k_\perp, k_\parallel)$. The anisotropic power spectra $P(k_\perp, k_\parallel)$ for Lyα and stars are shown in Fig.3.6. The same color scales are used for all four plots.

The Lyα power spectrum is shown in Fig.3.6a. It is isotropic and most of the power is concentrated at lower left corner, which corresponds to low k. The other three plots in Fig.3.6 are the power spectrum of stars when all the stars brighter than threshold magnitude m_* are masked. I use the same color scale for all four plots. Fig.3.6b shows the star power spectrum if stars brighter than $m_* = 12$ are masked. It is anisotropic and has a stripe along the $k_\perp$ direction for a given $k_\parallel$. The power from

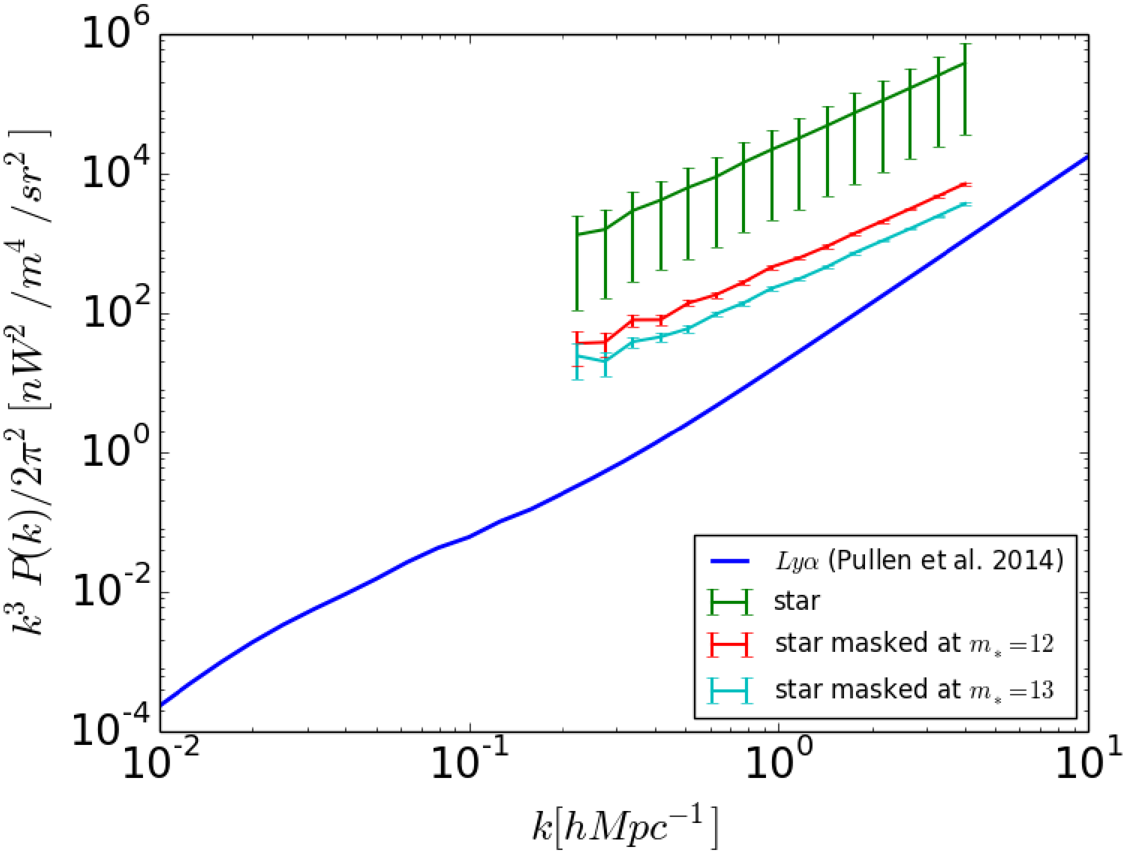

Figure 3.5: Power spectrum of star flux from corrected SDSS catalog at redshift $z = 2$, compared with theoretical Lyα power spectrum from Pullen et al. The power spectra of star flux after masking all stars brighter than $m_* = 12$ and $m_* = 13$ are also shown in the plot respectively.

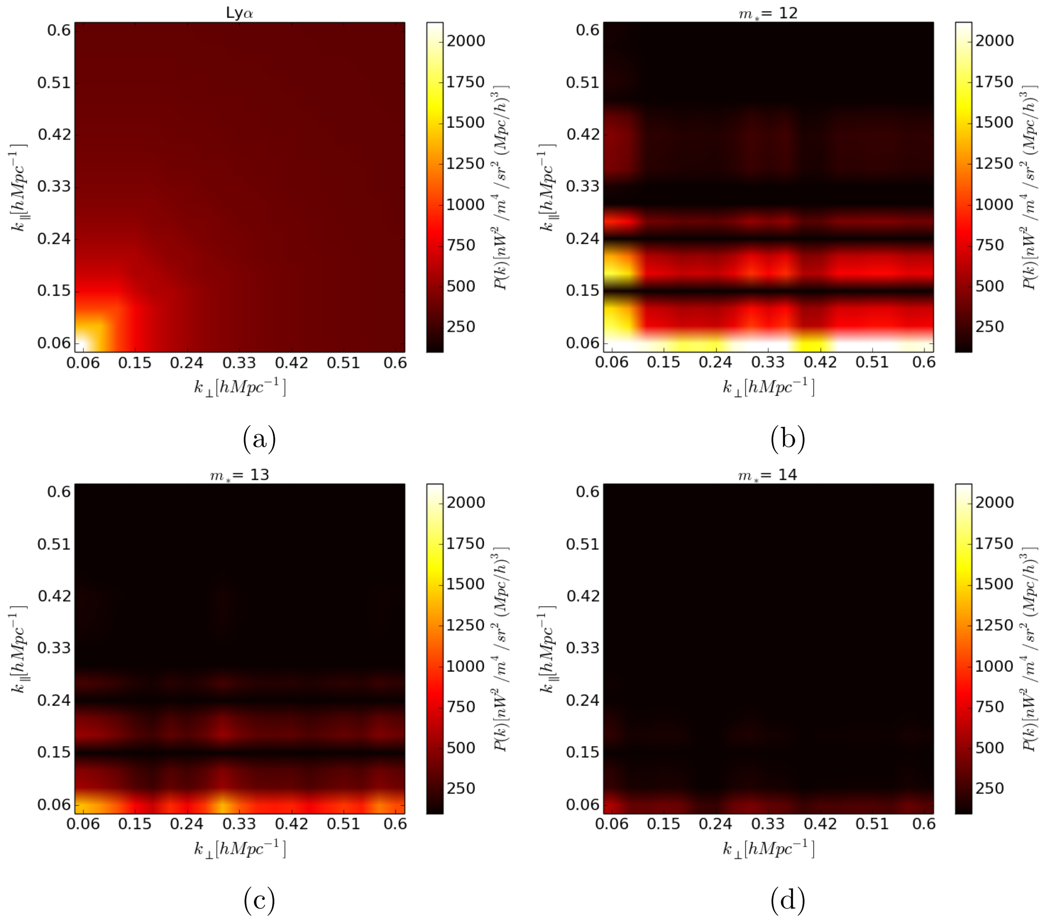

Figure 3.6: (a) Lyα power spectrum from Pullen et al. (b) Star power spectrum after masking at $m_* = 12$. (c) Star power spectrum after masking at $m_* = 13$. (d) Star power spectrum after masking at $m_* = 14$

Fig.3.6b is greater than Lyα power at small $k_\parallel$ in the plot where Lyα is concentrated. So it is not enough to mask at $m_* = 12$. Fig.3.6c and Fig.3.6d show the star power spectrum if the masking threshold magnitudes are $m_* = 13$ and $m_* = 14$ respectively. The power from Fig.3.6c is close to Lyα power, and is even fainter than Lyα at lower left corner. And Fig.3.6d shows less star power at all scales. As a comparison, the 3D power spectrum P(k) of stars after masking is also shown in Fig.3.5, where stars power is greater than Lyα even after masking. This is mainly because the power is large at small $k_\parallel$ modes for stars. So examining power spectrum in $P(k_\perp, k_\parallel)$ is a better way to extract Lyα power.

The comparisons of $P(k_\perp, k_\parallel)$ indicate that masking at threshold magnitude $m_* = 13$ is required to reveal Lyα power. Since Lyα power is concentrated at the corner, it is better to use a filter that keeps only the lower left corner of the power spectrum. The filter is aiming at further enhancing Lyα signal compared to star signal. The filter has a shape of a quarter circle in $P(k_\perp, k_\parallel)$. A stripe along $k_\perp$ at low $k_\parallel$ is removed from the quarter circle, because stars yield large power in this low $k_\parallel$ stripe. The shape of the filter is shown in Fig.3.7. A flat filter function is assumed, and everything outside the filter region is thrown away.

$$H(k) = \begin{cases} 1 & \text{if } k \text{ is inside the filter} \\ 0 & \text{if } k \text{ is outside the filter} \end{cases} \tag{3.7}$$

Fig.3.7 shows the example filter in the range of $0.06 \leq k_\perp \geq 0.5, 0.06 \leq k_\parallel \geq 0.5$. A stripe at $k_\parallel$=0.06 h/Mpc is removed and the quarter circle perimeter is zigzag due to coarse pixels. The actual filter range can be determined by experiments and scales of interest. Several filtering tests were made with various k ranges and various threshold magnitudes.

To compare the results of various filtering and threshold magnitudes, we integrated the total power in Fourier space after filtering. It is the total variance in the map after filtering. The results are shown in Fig.3.8, where the ratio of Lyα power to star power is plotted against various threshold magnitudes m_*. Five threshold magnitudes $m_{1/2} = 21, 22, 23, 24, 25$ were used for masking respectively. Three different k ranges were also tested in Fig.3.8, all starting from 0.06 h/Mpc. The ratio of power can be treated as the square of 'signal-to-noise' ratio. If the ratio is much greater than 1, then Lyα is dominating the power spectrum. Otherwise, the star foreground dominates the power spectrum. Fig.3.8 tells that masking stars brighter than $m_* = 17$ yields a ratio greater than 100. A wider k range can improve the ratio. Since the y-axis is in log scale, this ratio growth follows power law at bright magnitudes. At fainter magnitudes, this ratio grows slower mainly because the great number of stars in these magnitudes compensate for the drop in intensity. Overall, the ratio of Lyα power to star power can achieve 1000 if the threshold magnitude $m_* = 18$ is used.

To summarize, a threshold magnitude $m_* = 18$ is required to obtain a high 'signal-to-noise' Lyα power spectrum, where the star contamination is negligible. And a filter with the shape of a quarter circle in Fourier space is used to select the modes with high Lyα power.

The masking scheme also determines the angular resolution of the intensity mapping instrument. Since masking stars cause information loss in those pixels, we would like to limit this loss to 10%. In the worst case, every star is in a different pixel, and the number of masked pixels is equal to the number of stars. We estimated the maximum pixel scale that could retain 90% pixels after masking with SDSS catalog and corresponding field. Specifically, the count of stars from the corrected SDSS catalog is used to estimate how many stars are masked for different threshold magnitudes. Then the field is divided into equal size pixels. Assuming every star is in a different pixel, the maximum pixel scales are calculated from the 10% loss threshold. The pixel scales for various masking schemes are shown in Fig.3.9. It provides an upper bound for pixel scale when masking at different threshold magnitude m_*. Based on previous analysis, the Lyα intensity mapping instrument should have a maximum

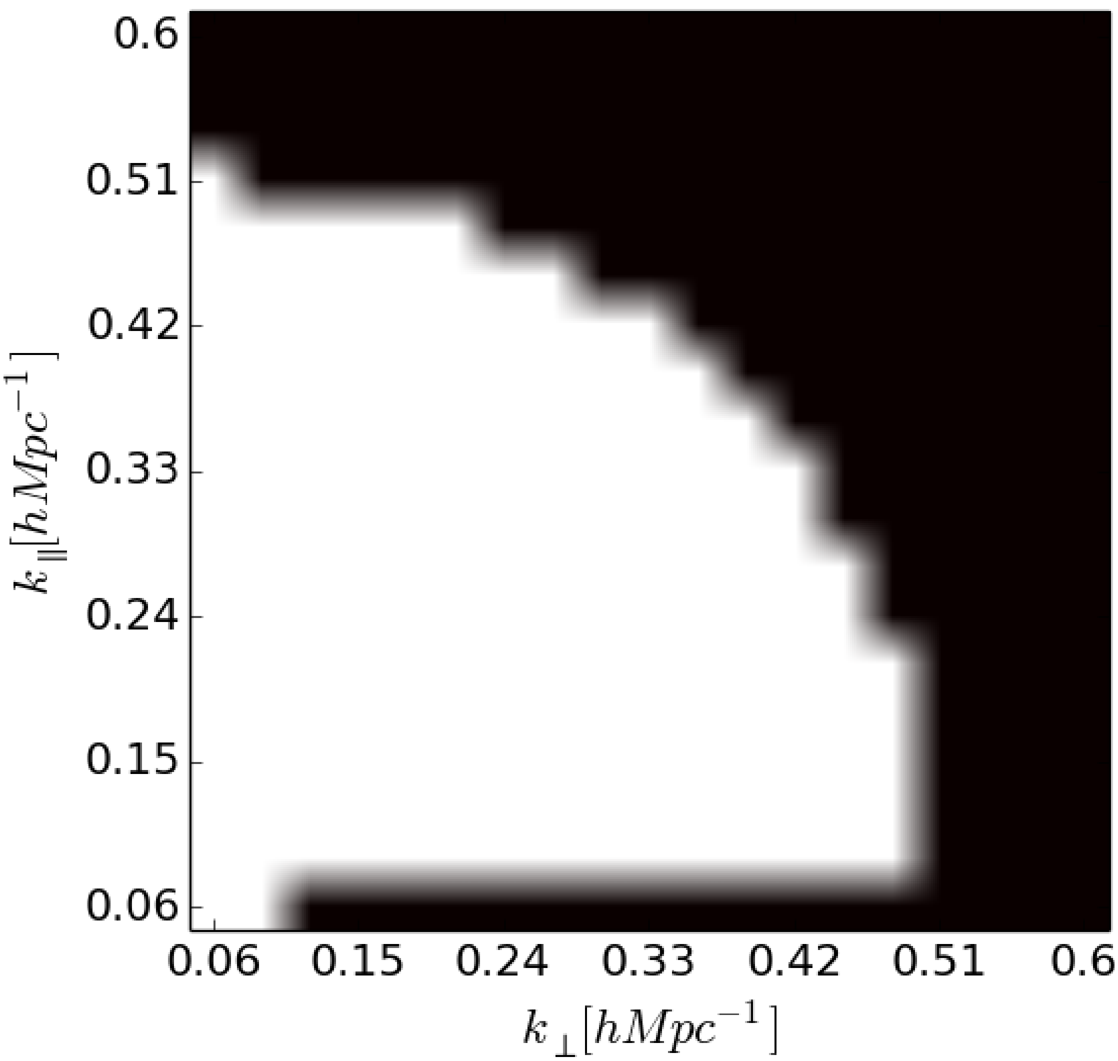

Figure 3.7: The shape of the filter in $(k_{\perp}, k_{\parallel})$ space. The white region is inside the filter, while the black region is thrown away.

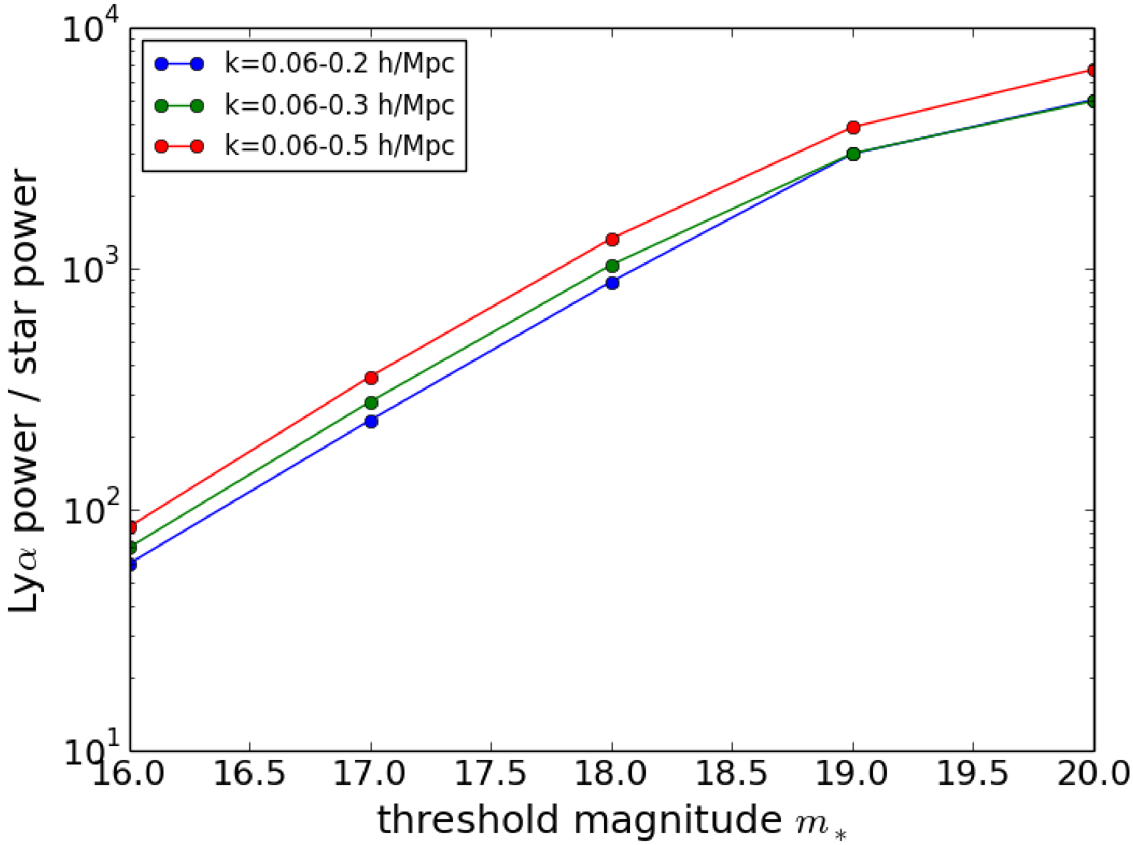

Figure 3.8: Ratio of total Lyα power and total star power at various masking threshold magnitudes m_*. The three curves show the results of three different k ranges.

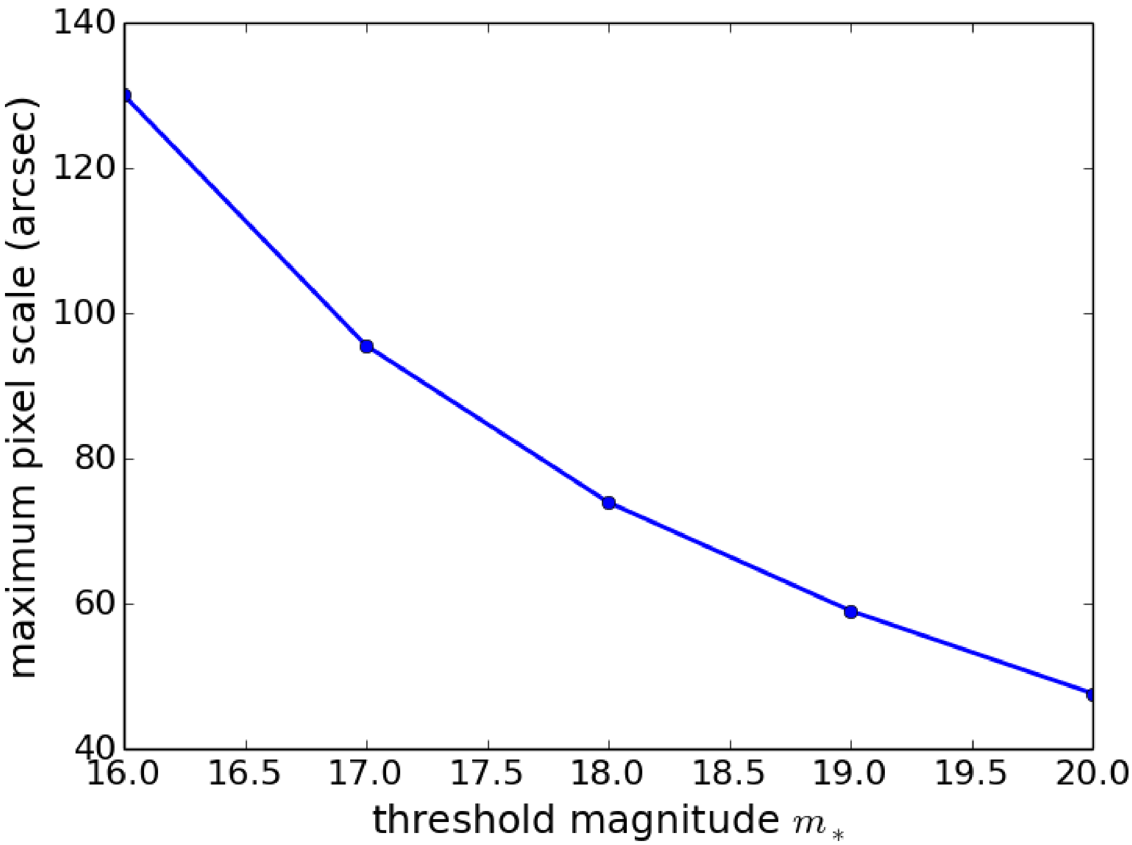

Figure 3.9: Maximum pixel scales to ensure 90% pixels are retained after masking. Different m_* corresponds to different masking threshold magnitudes.

angular resolution of 74″ if stars brighter than $m_* = 18$ are masked.

3.3.3 Discussion

The ratio of Lyα power to star power can achieve 1000 if we mask all stars brighter than magnitude $m_* = 18$. Since SDSS catalog is almost complete around magnitude 18, its completeness curve does not need to be taken into account. However, if the intensity mapping experiment is conducted in longer wavelength such as r band or i band, the completeness curve may come into play. Fig.3.10 shows M1 and M3 star templates from SDSS data release 2 [12]. We can notice that i band (centered at 765nm) intensity is about 40 times greater than u band (centered at 380nm) intensity, which corresponds to 4 magnitudes brighter. As the number of bright stars increases in i band, more stars need to be masked to reduce their contamination. When the threshold magnitude m_* is close to the detection limit, we need to estimate the number of stars that are not detected by the catalog. That is because stars around the threshold magnitude m_* which are not masked according to the catalog contribute most to the star power spectrum. And it is important to estimate the number of stars remained on the sky at each magnitude to properly determine the star power spectrum.

For actual masking, SDSS catalog is not enough alone because it is incomplete for bright stars. One solution is to use catalogs that have bright stars. Yale Bright Star Catalog consists of stars brighter than magnitude 6.5, which is roughly every star visible to the naked eye from Earth [99]. The HIPPARCOS and TYCHO catalogs have limiting magnitudes around $V \approx 12$ [100]. Smithsonian Astrophysical Observatory (SAO) Star Catalog is also more or less complete to magnitude $V \approx 12$ [101]. These catalogs can be used to mask bright stars along with SDSS catalog. Another solution to find bright stars is to observe and locate them with the telescope. These stars brighter than magnitude 13 can be detected using low sensitivity instruments with short exposure time. For example, I can use my GSTI without the grism on to locate these bright stars before intensity mapping experiments.

The pixel scales in Fig.3.9 provide us with important information to design a new intensity mapping telescope. If we mask all stars brighter than $m_* = 18$ using the SDSS catalog, the pixel size of the instrument can not be larger than $74''$. The Baryon Acoustic Oscillations (BAO) ring has a diameter of $9.2°$ at redshift 2, and the telescope with an FOV of $10° \times 10°$ must be designed to enclose the whole ring. Taking both the pixel scale and the FOV into account, the sensor is required to have approximately 500×500 pixels. These are many pixels for non-multiplex integral field spectroscopy instruments, because they need more than one spectrometer to obtain the spectrum for each pixel simultaneously. For example, if one column of the pixels on the sensor are fed into one spectrometer with fibers, then 500 spectrometers are required to obtain the spectrum of the entire field of the instrument described above. 500 spectrometers and fiber bundles are difficult tasks for any intensity mapping experiment at this time. So an intensity mapping instrument with multiplex advantage must be used, such as the GSTI.

3.4 Conclusion

In this chapter, I discussed three types of foreground contamination: continuum foreground, line foreground, and star foreground. We can remove continuum foreground by fitting and subtracting the components. For line foreground, we can remove it by cross-correlation or by masking bright pixels. Finally, I studied star foreground contamination and its removal techniques. I developed a masking and filtering scheme to remove star foreground. We can use the SDSS catalog or any all-sky survey catalog with a similar completeness to mask the bright stars in an intensity mapping experiment. In addition, we also need to locate bright stars on the sky with either bright stars catalog or direct observation. All stars brighter than magnitude 18 have to be masked to make star power negligible. The masking is necessary because most stars are bright enough to affect the power spectrum and the detection of Lyα sources.

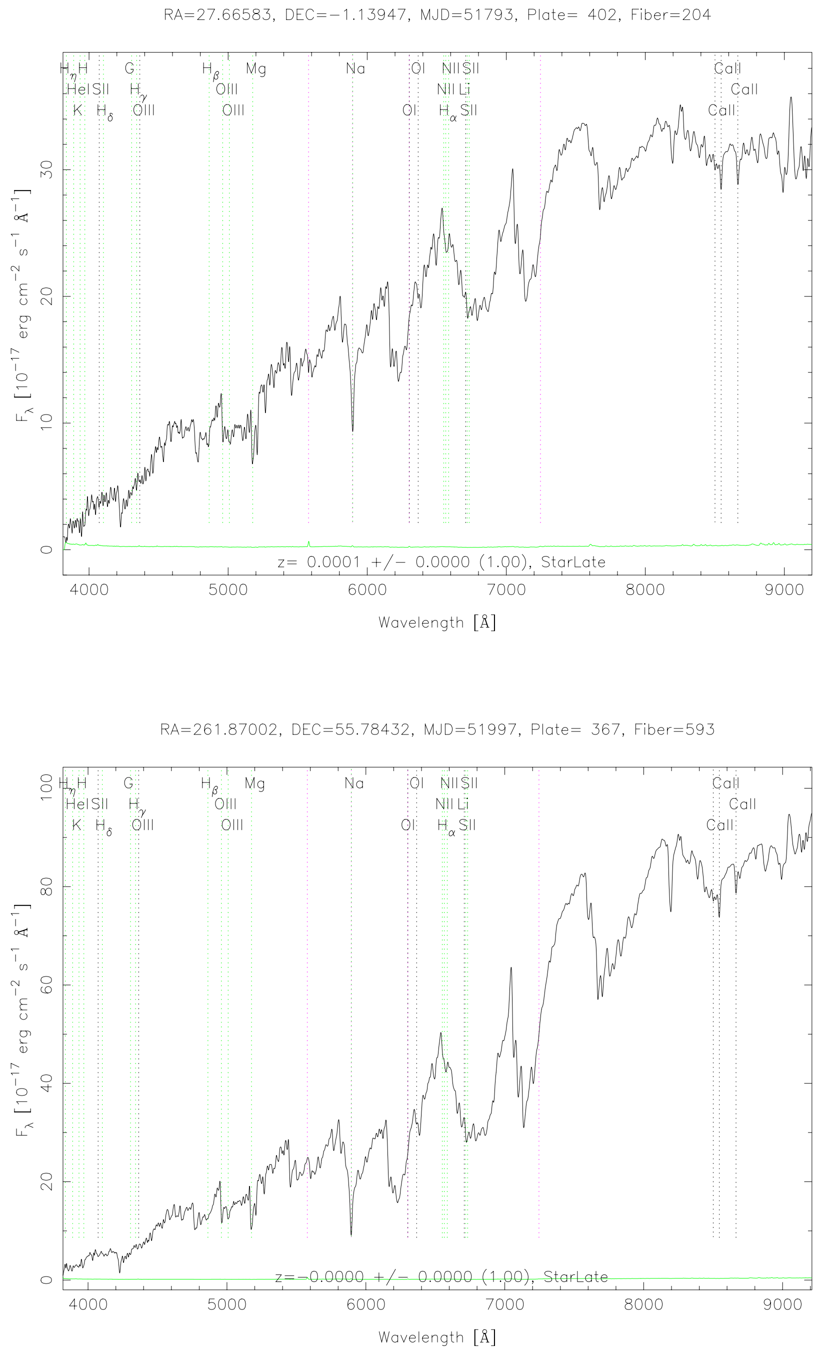

Figure 3.10: M1 star and M3 star template from SDSS data release 2. [12]

A filter in $(k_\perp, k_\parallel)$ Fourier space is used to keep the modes with large Lyα power. The masking scheme also provides an upper bound for the pixel scale in an intensity mapping experiment. The pixel scale cannot be larger than $74''$ if we want to retain 90% pixels after masking with the SDSS catalog. This pixel scale also implies instruments which require multiple spectrographs are not feasible for wide field intensity mapping. Only integral field units with multiplex advantages are suitable for intensity mapping experiment, including Grism Spectrotomography and Imaging Fourier Transform Spectroscopy.

Chapter 4

Apparatus

In this Chapter, I describe in details the Grism Spectrotomographic Imager I built. Specifically, I list the major components and the specification of my telescope. I also describe the optics design and the operation of the telescope. Sample images from the telescope are displayed as the raw data. An alternative design is also proposed to implement pixel masking at the image plane.

4.1 Grism Spectrotomographic Imager

My telescope consists of a camera, a lens, a grism, and a field stop, as shown in Fig.4.1. The body of the telescope is Nikon D800 camera with a CMOS sensor and lens with focal length $f = 200$mm. The grism is the combination of a wedge prism and a 100 lines/mm grating. A 5 feet 11 inches long, 4 inches diameter High-density polyethylene(HDPE) corrugated tube serves as the field stop. My telescope can be supported on a telescope equatorial mount as shown in Fig.4.2. The mount has a tracking motor that allows tracking fields. The telescope parameters are listed below in Table.4.1.

The spectral data is obtained by taking a set of images as the grism rotates. Specifically, I set an angular step size α for each rotation and perform the grism rotation of α clockwise using the stepper motor controller. Right after each rotation α, the camera is commanded to take one picture of the current grism-dispersed image. When the grism rotates back to its original location, our full dataset consists of N_{proj} images of different angles, where $N_{proj} = 360/\alpha$. I implemented this control system with the driver from stepper motor controller and Nikon. I wrote the program in C language to control the rotating stage and camera in sequence to acquire a complete set of images.

I built a laboratory test target to test the GSTI. The target has 5 LEDs, of which three are yellow and two are green. They are attached to white cardboard and connected to direct current power supply in parallel with each other. The 5 LEDs are each mock stars on the sky and show what stars' spectra look like in our

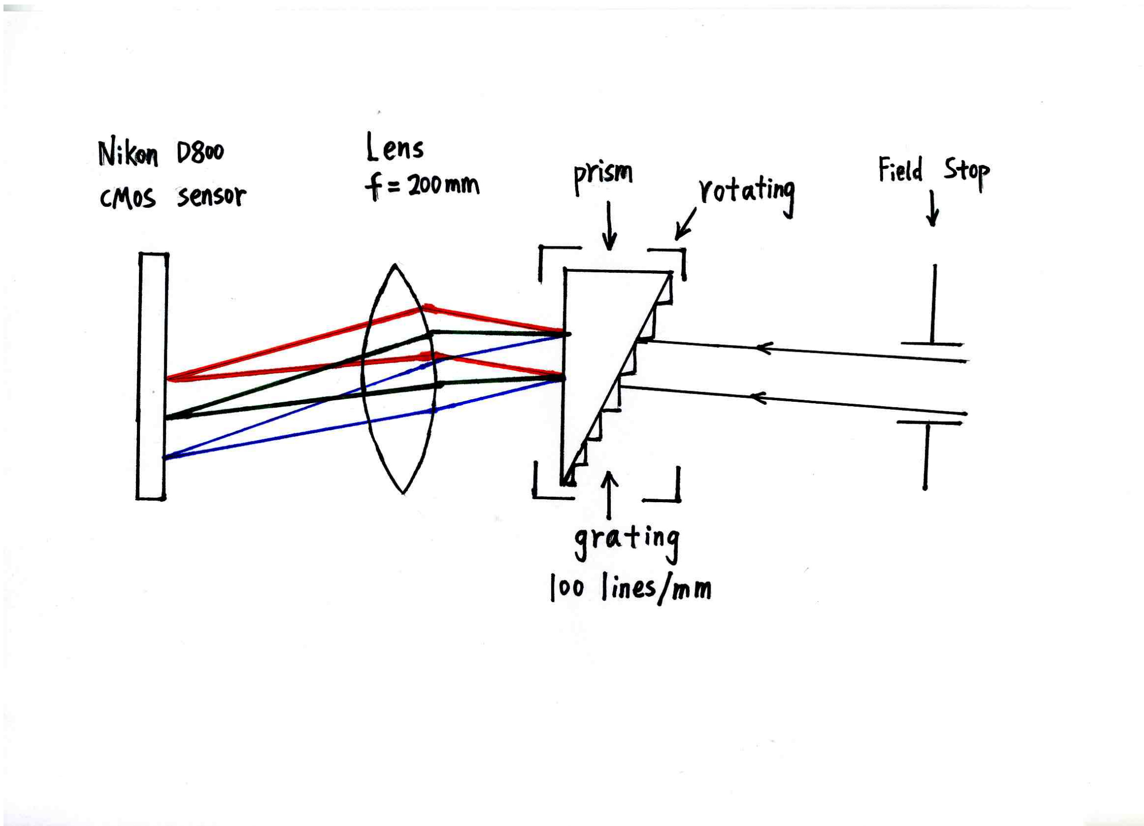

Figure 4.1: Telescope Schematic: The light rays first go through the field stop which can make sure all spectra lie in the range of our sensor. The next element is a grism which consists of a wedge prism and a 100 lines/mm grating. Grism is fixed on 2 inches aperture Oriel rotation stage controlled by Phidget stepper motor controller and can be rotated about the optical axis. Finally, the light is focused on the sensor through the lens.

Figure 4.2: Telescope setup in the lab. Top: Nikon camera and grism in the back, preceded by a white tube as the field stop. Bottom: Phidget stepper motor controller connected with the rotational stage. Grism is placed on the stage and is covered by the 1-inch white aperture stop.

Sensor	CMOS (rgb filter)
Focal length(f)	200 mm
Aperture (d)	25 mm
f/d	8
grating	100 lines/mm blazed for 1st order
sensor FOV	$8.6° \times 6.9°$
Pixel scale	4.9”
Prism refractive index	1.5
Prism wedge angle	8°
Prism deflection angle	4°
Undeflected wavelength	706 nm
Field stop angle	3°
Field stop length	5 feet 11 inches

Table 4.1: Telescope Specification

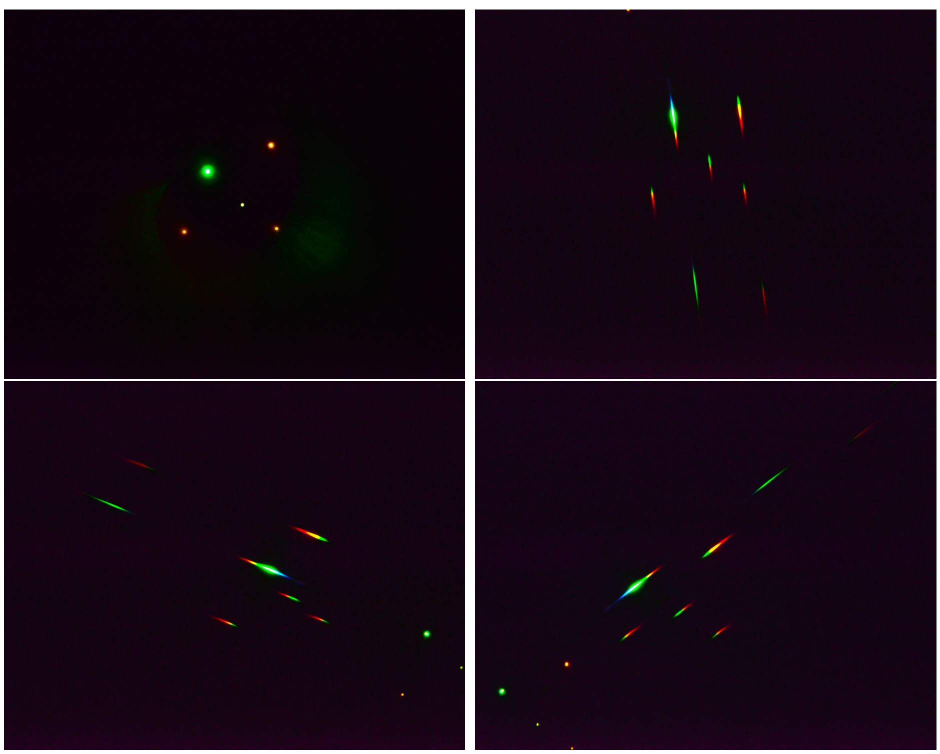

Figure 4.3: 5 LEDs and their spectra at different angles. The upper left images show the locations, colors and brightness of all LEDs with the grism removed. The other three images show spectra at three different orientations of the grism, which are 120° apart.

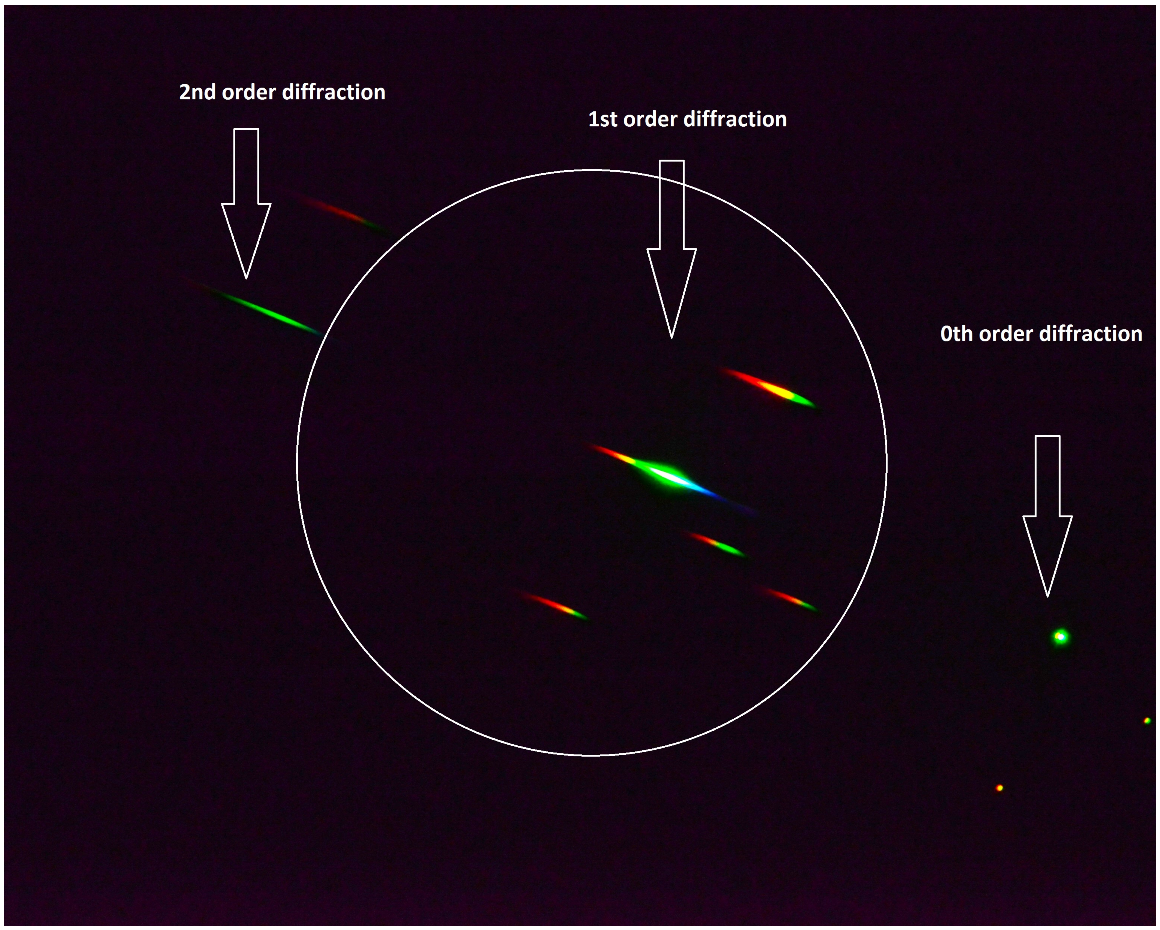

Figure 4.4: Three diffraction orders can be seen in the grism-dispersed image. The 5 brightest stripes in the center are due to 1st order diffraction, which are used for reconstruction. Only the circular region at the center of the image is retained for reconstruction.

telescope. Images for a sample data set are shown in Fig.4.3 and the diffraction orders are explained in Fig.4.4.

Notice the spectra are aligned at various directions for different grism angles. The brightest spectral stipes in Fig.4.3 are due to first order diffraction in the grism. Also visible are occasionally zero order and second order images appearing on the sensor. The rotation of the grism causes the spectra to rotate about the source, which provides us with the way of reconstructing the three dimensional hyperspectral data cube.

My telescope, GSTI, operates based on the idea of Grism Spectrotomography. Grism Spectrotomography is different from Grism Spectroscopy, which is the ordinary technique that uses only one grism orientation and a direct image without grism. Grism Spectroscopy usually aims at obtaining spectra for a few objects previously isolated in the non-dispersed image. It uses a direct image to locate the sources and determine the source sizes, and uses the dispersed image to extract the spectra directly. It is often difficult for Grism Spectroscopy to retrieve the spectral information of overlapping spectra. In contrast, our technique GST aims at recovering the spectral information of every object in a region simultaneously rather than a few objects. Tomographic reconstructions need to be carried out to extract the spectrum of each object.

4.2 General Design for Masking Pixels

In general, a GST telescope can follow the design in Fig.4.5. The field stop is placed inside the optics at the image plane of the objective lens. So the long tube field stop in front of the lens is no longer required and the length of telescope can be made shorter. Another advantage of this design is that the mask can be placed together with the field stop. Unwanted stars or line contamination are masked at the image plane before being dispersed into spectra. Furthermore, this masking scheme can be applied to any intensity mapping telescope besides the GST. This is the telescope I refer to when I discuss masking star foregrounds. I did not implement this design in the thesis due to its complexity.

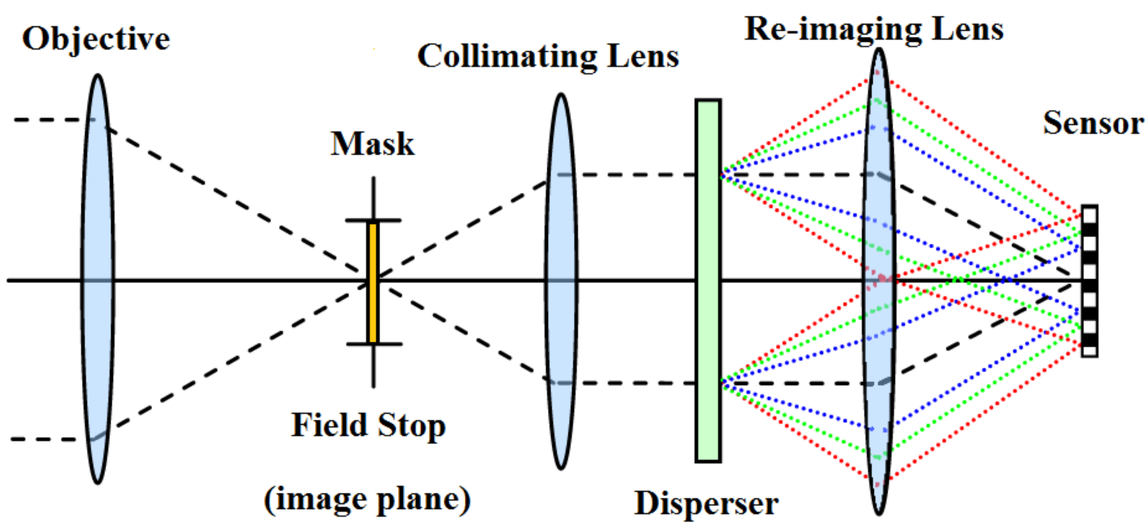

Figure 4.5: Telescope schematic with masking and field stop inside the optics. The mask and field stop is placed at the image plane. The figure is adapted from a paper by Kudenov et. al. [13].

Chapter 5

Reconstruction – Back projection

In this Chapter, I describe the grism imaging process as the projection from the hyperspectral data cube. Based on the imaging model, I discuss the spectral resolution of my telescope. Then I explain the first part of my reconstruction algorithm: back projection. I show examples of back projection using synthetic sources. Moreover, I describe the back projection in Fourier space in terms of Fourier Slice Theorem, which indicates the incomplete information problem for the grism technique. I choose the projection angle to be 45° for the thesis.

5.1 Imaging Model

In X-ray computed tomography for medical imaging, an X-ray source rotates around the object and the X-ray sensor is placed at the opposite side of the circle from the X-ray source. The raw image acquired by the scanner is the projection of the object being scanned, as the X-ray intensity is reduced by the tissue inside the object. Regarding mathematics, the projection is described as the Radon transform(2D) or X-ray transform(3D) of the object structure. Then the raw images are processed using tomographic reconstruction.

In analogy, I treat each grism-dispersed image as the projection of the data cube from parallel rays onto our sensor plane. After recording a set of grism-dispersed images (projected images set), our next goal is to reconstruct the 3-D hyperspectral data cube (x, y, λ) of a region on the sky. x, y corresponds to 2-D cartesian coordinates on the sky and λ corresponds to the wavelength coordinate at each location. This 3-D data cube is a convenient way to show the spectral information of a region rather than a point source.

This projection model is depicted in Fig.5.1, which shows the projection of three point source with different wavelength and locations. These two projections correspond to two different grism rotation angle α. The nature of grism shifts the first order to the center and makes the longer wavelength closer to the source, which explains why λ axis pointing downwards.

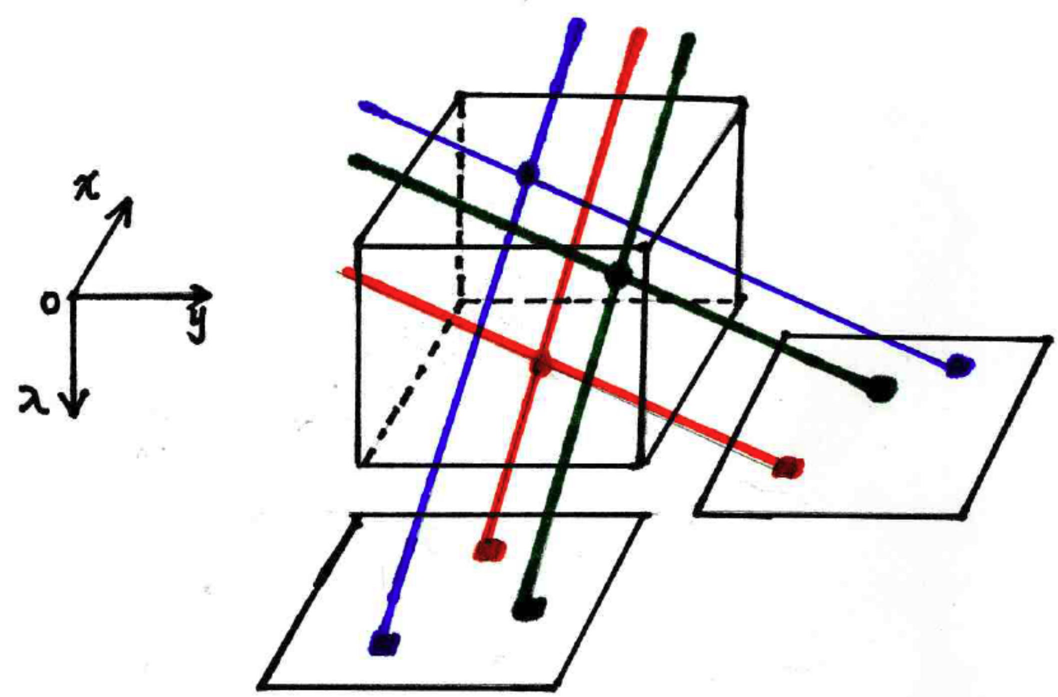

Figure 5.1: Projection model: There are three monochromatic point sources in the 3-D hyperspectral data cube, with red being longer wavelength and blue being shorter wavelength. The projection of this hyperspectral cube onto sensor is shown at two different orientations, corresponding to two different grism rotation angles.

Since the imaging processes of my GSTI and X-ray computed tomography are similar, I designed a reconstruction technique closely related to filtered back projection used in medical imaging. I divide the reconstruction into a two step process: 1) simple back projection, 2) point spread function (PSF) deconvolution. I focus on simple back projection in this Chapter and will discuss the PSF deconvolution in Chapter.6.

5.2 Resolution of Grism Spectrotomography

Before I explain the back projection, I would like to discuss the resolution of my telescope and how it is related to the back projection. The geometry of the grism optics is described in Fig.5.2. Given the prism wedge angle A, the refractive index of prism n and the grating constant $d_{grating}$, we can write equations for each relevant angle. We only focus on the first order of diffraction.

$$\lambda = d_{grating} \sin\theta \tag{5.1}$$

$$n = \frac{\sin(\theta + A)}{\sin\alpha} \tag{5.2}$$

$$\phi = \alpha - A \tag{5.3}$$

$$n = \frac{\sin\gamma}{\sin\phi} \tag{5.4}$$

Eq.5.1 is the basic grating equation for perpendicular incident light [102]. Eq.5.2 is the snell's law on the first surface, and Eq.5.4 describes the snell's law at the second surface when the light exits the prism [103]. Eq.5.3 gives the relation between wedge angle and refraction angles. Combining Eq.5.2 - Eq.5.4, I derive the expression of deflection angle γ in Eq.5.5 and its relation with λ by using approximate form of Eq.5.1, $\lambda = d_{grating}\theta$ in Eq.5.6.

$$\sin\gamma = \sin(\theta + A)\cos A - n\sin A\sqrt{1 - \frac{\sin^2(\theta + A)}{n^2}} \tag{5.5}$$

$$\sin\gamma = \sin(\frac{\lambda}{d_{grating}} + A)\cos A - n\sin A\sqrt{1 - \frac{\sin^2(\frac{\lambda}{d_{grating}} + A)}{n^2}} \tag{5.6}$$

If we assume $(\theta+A)$ is sufficiently small, the approximation can be used is $\sin x \approx x$ and $\sqrt{1-x} \approx 1 - x/2$. The result after approximation is shown in Eq.5.7. It is then a quadratic equation of θ.

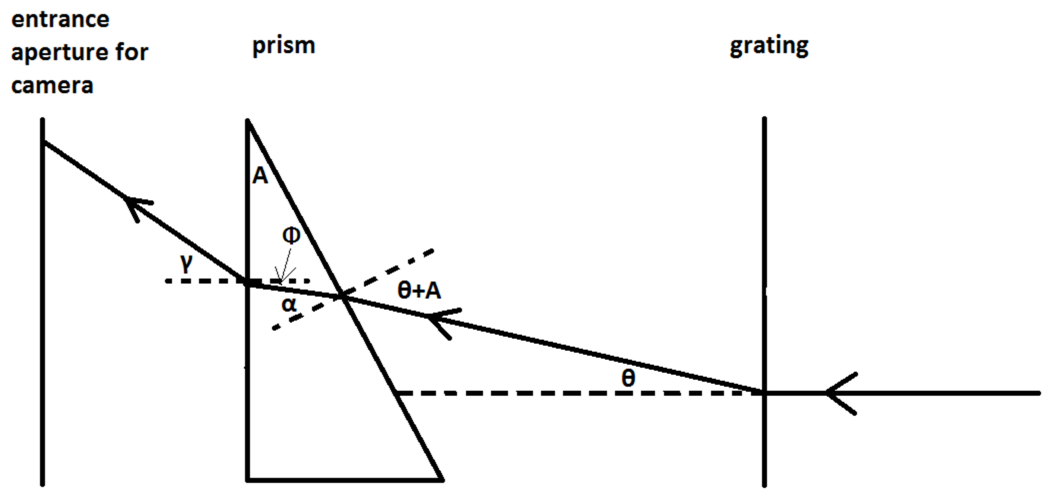

Figure 5.2: Schematic grism deflection. The diffraction angle when the light passes grating is θ. Then the light will be refracted twice at two surfaces of the prism. The final deflection angle due to the imaging system is γ.

$$\begin{aligned}\sin\gamma &\approx (\theta + A)\cos A - n\sin A(1 - \frac{(\theta+A)^2}{2n^2}) \\ &\approx \frac{\sin A}{2n}\theta^2 + \theta(\frac{A\sin A}{n} + \cos A) + \frac{A^2}{2n}\sin A + A\cos A - n\sin A \end{aligned} \tag{5.7}$$

We can again substitute λ in with approximate form of Eq.5.1 to derive $\sin\gamma$ as a function of λ. It has not only quadratic term λ^2, but also λ-dependent index $n(\lambda)$. The linear term dominates the deflection angle in Eq.5.8.

$$\begin{aligned}\sin\gamma \approx \frac{\sin A}{2n(\lambda)}\frac{\lambda^2}{d_{grating}^2} + \frac{\lambda}{d_{grating}}(\frac{A\sin A}{n(\lambda)} + \cos A) \\ + \frac{A^2}{2n(\lambda)}\sin A - n(\lambda)\sin A + A\cos A \end{aligned} \tag{5.8}$$

We plot the diffraction angle γ using both Eq.5.6(accurate) and Eq.5.8(approximate) in Fig.5.3. The deflection angle is plotted with the wavelength in the range $300nm < \lambda < 700nm$ and a fixed refractive index $n = 1.5$ is considered. Both plots show a significant linearity between two parameters. Although the formula indicates a

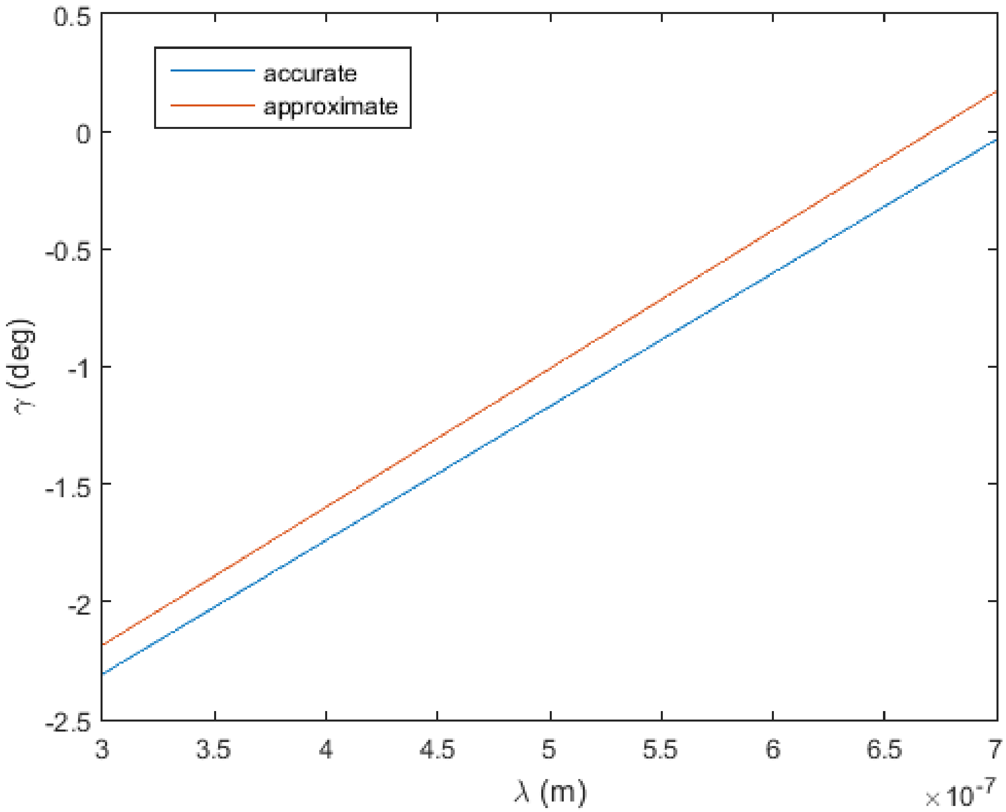

Figure 5.3: Deflection angle γ as a function of λ at constant $n = 1.5$, for both the precise formula Eq.5.6 and the approximate formula Eq.5.8

quadratic relation between γ and λ, our wavelength range is too small to show any parabolic effect. But we still need to take into account the effect of the refractive index varying with the wavelength $n(\lambda)$.

The material of our prism is assumed to be Borosilicate glass BK7, whose refractive index is given in Eq.5.9 for SCHOTT BK7 [104]. The change of n in the visible light band is plotted in Fig.5.4. The larger slope at shorter wavelength implies a possible deviation from linearity. As we can see from Fig.5.5, the resulting deflection angle relation is more curved and deviates more from the original straight line at a shorter wavelength.

$$n^2 = 1 + \frac{1.03961212\lambda^2}{\lambda^2 - 0.00600069867} + \frac{0.231792344\lambda^2}{\lambda^2 - 0.0200179144} + \frac{1.01046945\lambda^2}{\lambda^2 - 103.560653} \tag{5.9}$$

Since the model assumption is the parallel rays projection of the spectrum, the

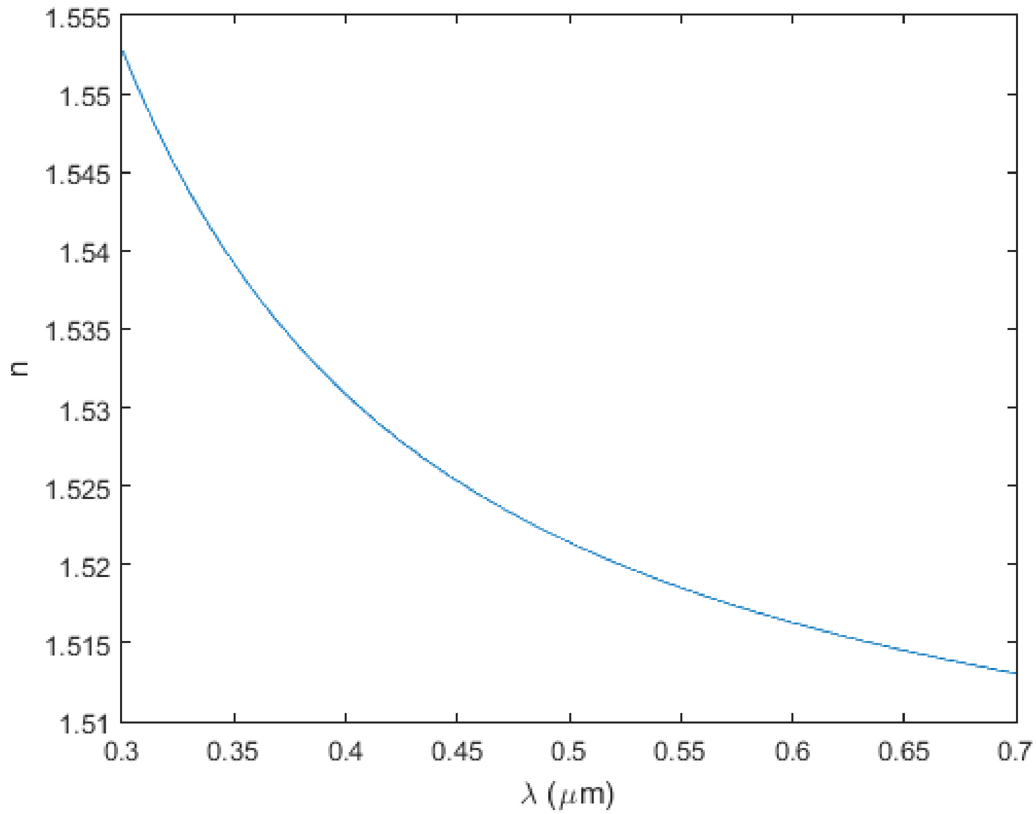

Figure 5.4: Refractive index of BK7 at various wavelengths

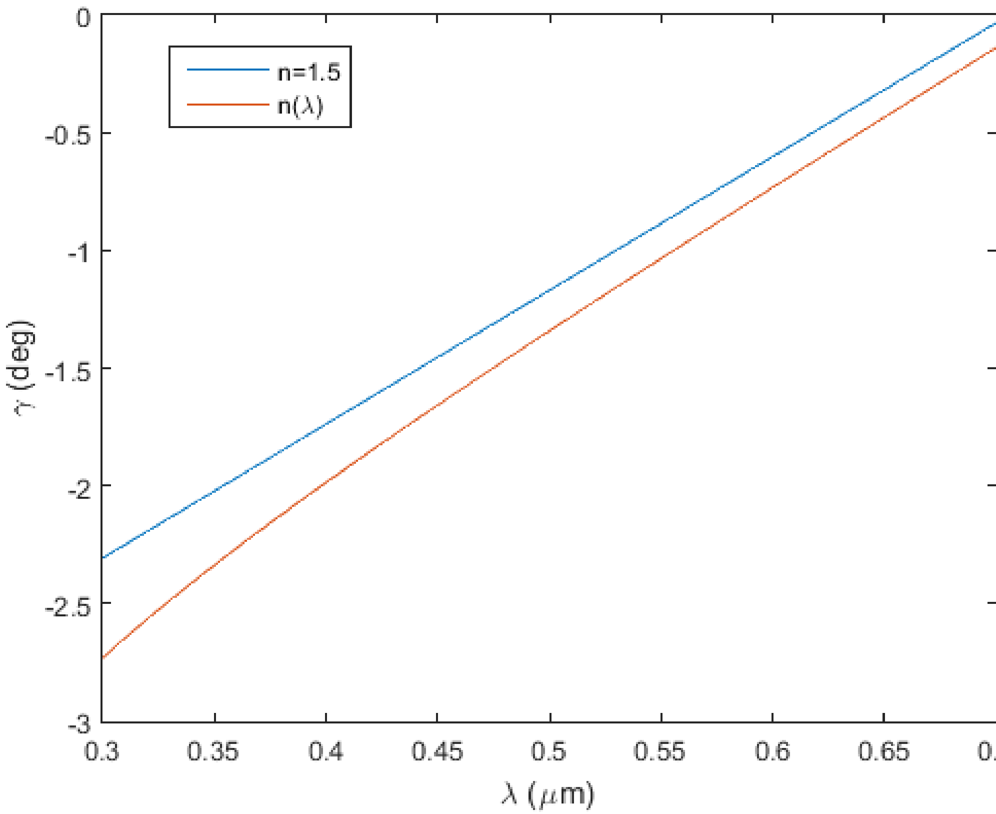

Figure 5.5: Deflection angle γ as a function of λ for constant n and varying n of BK7 using the precise formula Eq.5.6

underlying assumption also involves a linear relation between deflection angle γ and wavelength λ. This assumed linearity fails to hold in reality due to grism imaging system. We use the equations given above to find the accurate deflection angle for each wavelength. Then its deviation from linearity can be obtained by linearly fitting the curve and extracting the residuals, shown in Fig.5.6. Apparently, the accurate deflection angle lies closely around the fitted line and has a concave shape in terms of the residuals. According to the fitting results, the Nikon D800 sensor has a resolution $\Delta\lambda_{pixel} = 0.22nm$ over the entire wavelength range. And the effect of the curvature on resolution can be adjusted according to Fig.5.7. The resolution from the grism, along with the back projection, determines the true spectral resolution of the system.

I define the projection angle β used in the model as the angle between projection direction and the normal direction of our sensor, as depicted in Fig.5.8. Although β is geometrically related to the deflection angle $\gamma(\lambda)$, we can take the liberty of choosing an appropriate back projection angle β. Because spatial coordinates x, y have different units from wavelength coordinates λ, and we can scale λ axis independently of x, y. This choice of β affects the final resolution of the spectrum in the hyperspectral data cube. This effect is shown in Fig.5.9. It shows the spectrum shape of a synthetic monochromatic source reconstructed with different β, ranging from 10 to 90. The spectral resolution is usually determined by the Full Width at Half Maximum (FWHM) of the spectrum of a monochromatic source. Although the spectrum becomes narrower as we increase the projection angle β, it does not simply mean the resolution is improved. The scale of the voxel is also altered for different β, as depicted in Fig.5.8. For a point source with uniform spectrum, it has a spectrum width d on the grism-dispersed image(sensor), while it has a spectrum width L in the back-projected cube. Given the β we choose, their relation is described by Eq.5.10.

$$L = \frac{d}{\tan(\beta)} \tag{5.10}$$

We notice the critical angle here is $\beta = 45°$. When $\beta < 45°$, it is the same as $L > d$. This means one pixel on the sensor is mapped to more than one voxel in the reconstructed cube. So a finer voxel scale can be achieved on the reconstructed cube by interpolation. On the other hand, when $\beta > 45°$, it is the same as $L < d$. More than one pixel is mapped to one voxel in the reconstructed cube. Therefore the pixel scale is finer on the sensor. The spectral resolution $\delta\lambda$ in this case can be defined by Eq.5.11.

$$\begin{aligned} \delta\lambda &= \text{FWHM} \times \text{voxel scale in the reconstructed cube} \\ &= \text{FWHM} \times \frac{d \times \Delta\lambda_{pixel}}{L} \\ &= \text{FWHM} \times \tan(\beta) \times \Delta\lambda_{pixel} \end{aligned} \tag{5.11}$$

where FWHM is Full Width at Half Maximum and $\Delta\lambda_{pixel}$ is the pixel scale on the sensor as defined in Section 5.2. Since the pixel scale is determined by the system,

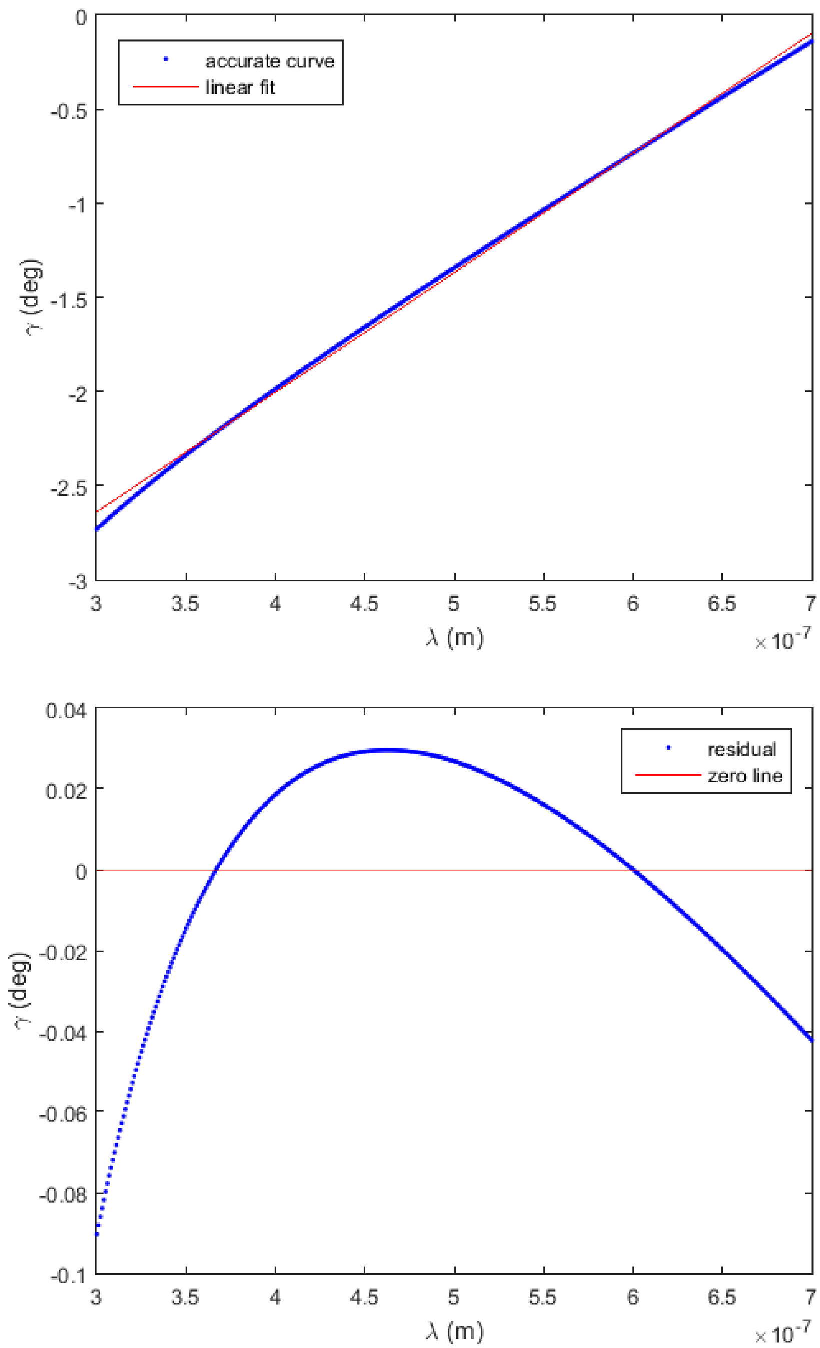

Figure 5.6: Linear fit on deflection angle γ as a function of wavelength λ. Top: Red line is the linear fit of the calculated deflection angle (blue dots). Bottom: Residuals(blue) of the linear fit

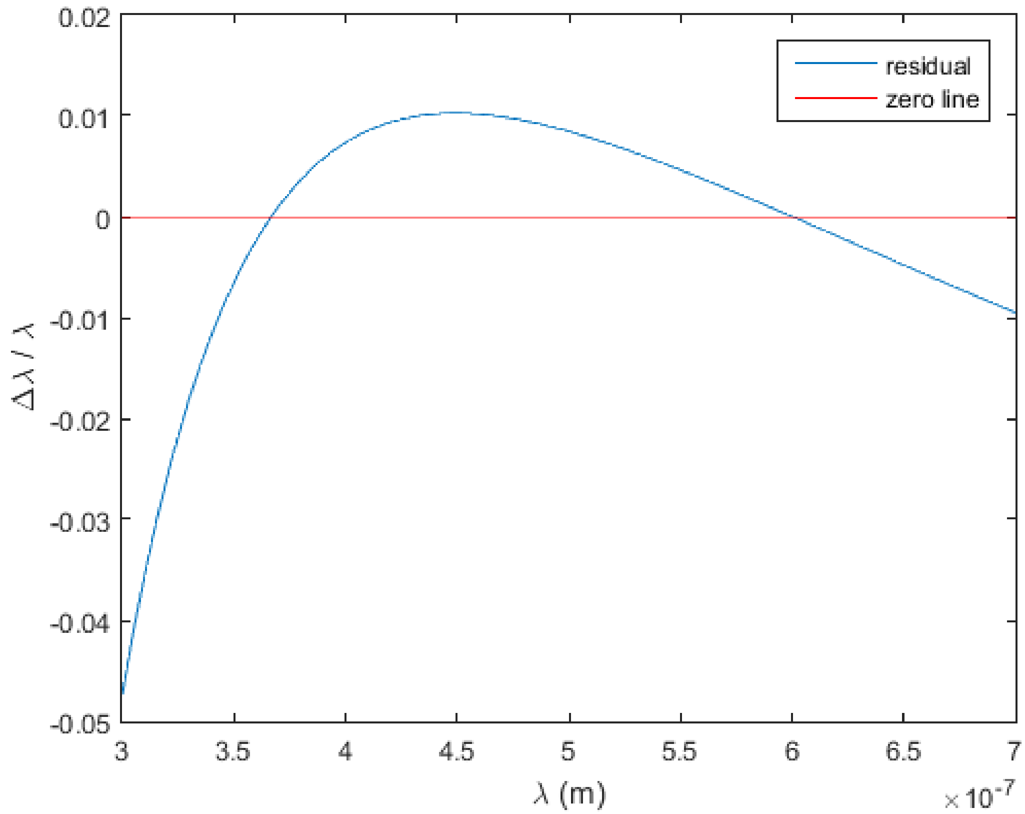

Figure 5.7: Resolution correction curve: the wavelength difference $\Delta\lambda$ between true λ and linear fit λ_{fit}.

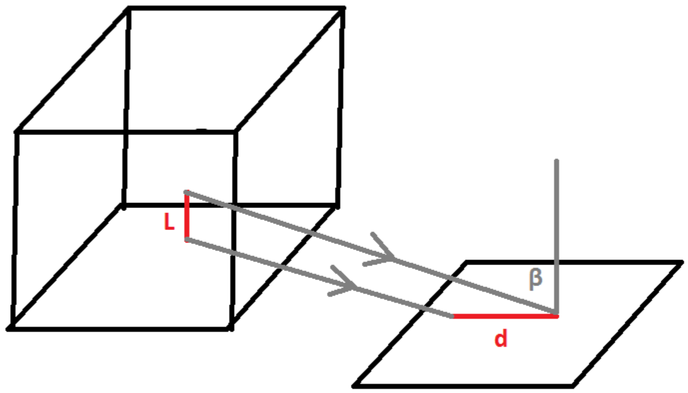

Figure 5.8: The relation between spectrum width d of the projected image and spectrum width L of the reconstructed cube. Given a projection angle β, the spectrum of width L from a point source in the cube is projected onto the sensor plane with a spectrum width d. The back projection is the reverse process and can be interpreted in the same way.

$\delta\lambda$ depends only on FWHM and β. The combined information from Fig.5.8 and Fig.5.9 shows a delicate trade-off between FWHM and β. As β increases, $\tan(\beta)$ also increases while FWHM decreases, making the change of $\delta\lambda$ uncertain. It is the same situation when β decreases. Notice that FWHM is at least 1 and is limited by the size of the reconstructed cube. So β cannot be too large nor too small. I will discuss another important factor that affects the choice of β later in this Chapter.

5.3 Back Projection Algorithm

Back projection is a linear reconstruction method shown in Fig.5.10. The fundamental idea is to project back along its path for every point on a projection image, which will form a line in the reconstructed data cube. More lines will be added to the reconstructed data cube as we continue to back-project all the projections. These lines intersect at the location of actual object wavelength. In the simplest case of a monochromatic source, the lines intersect to form a double cone in the reconstructed hyperspectral cube after basic back projection, shown in Fig.5.10.

The double cone is the PSF for a point (monochromatic source) in the original data cube. Based on the back projection algorithm, the double cone will have the

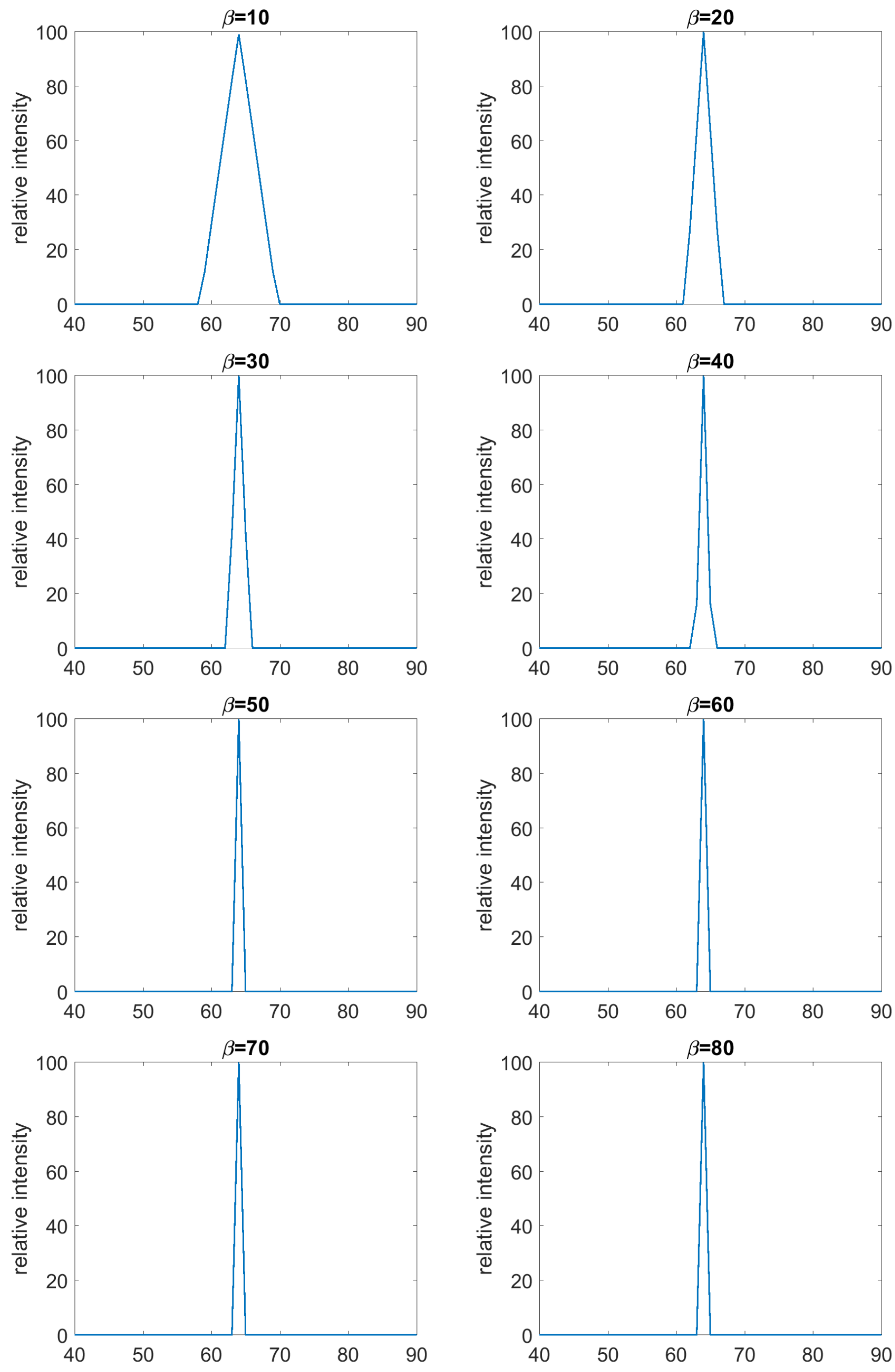

Figure 5.9: Reconstructed spectrum of an one-pixel monochromatic point source using different β $(10°, 20°, 30°, 40°, 50°, 60°, 70°, 80°)$

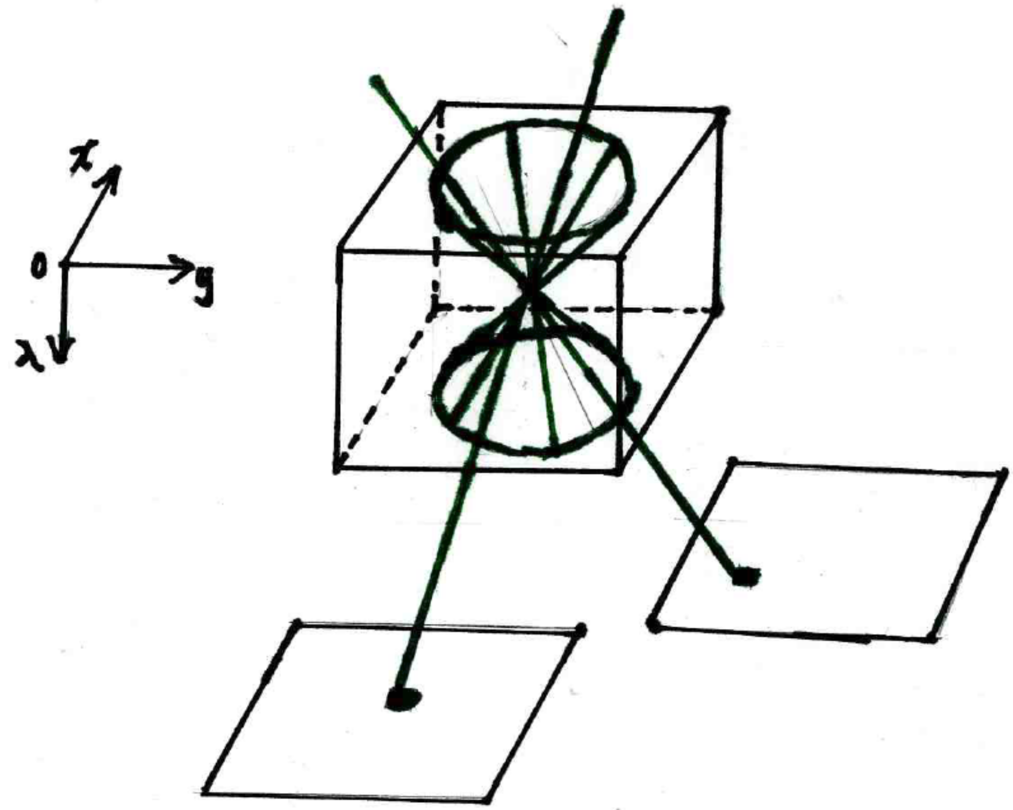

Figure 5.10: Back projection model: Back projection is the reverse process of projection. Monochromatic point source in the 3-D spectrum data cube is projected as a point in projected images. The back projection from all these points in projected images forms a double cone in real space, with the intersection being the point source.

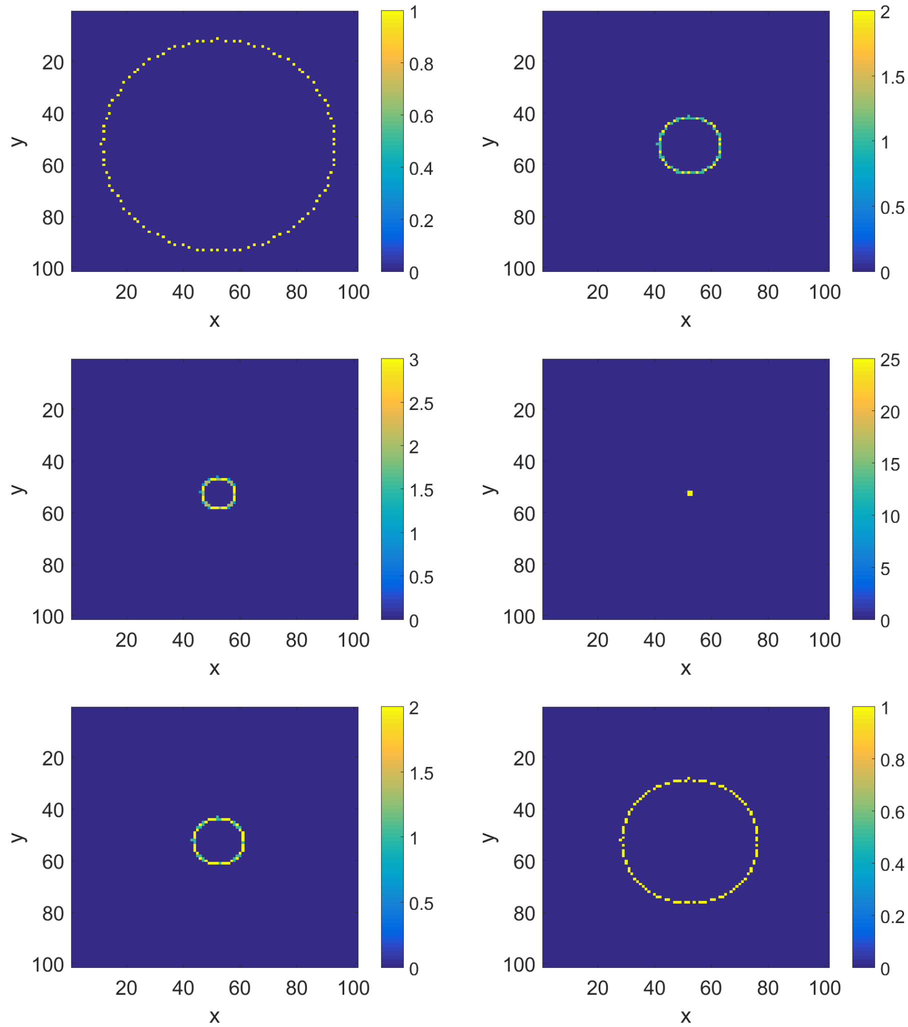

Figure 5.11: Double cone PSF Illustration: Slices of double cone at six different wavelengths are shown for the reconstruction from a synthetic monochromatic point source.

same amount of total flux at each wavelength slice λ. At any given wavelength λ^*, the slice of a double cone (x, y, λ^*) has a ring with uniform intensity, except at the wavelength λ_0 of the source where it is a point on the slice. The double cone structure is illustrated by reconstructing a synthetic monochromatic point source at the center of a cube in Fig.5.11, in the form of hyperspectral cube slices at various λ. The slice with only one bright spot is the true location of this point source. All slices come from the reconstruction of a synthetic source. This double cone structure can be removed by deconvolving the reconstructed data cube with this PSF. Specifically, in computation, the PSF is modeled as a double cone whose vertex is located at the center of a cube. The details of PSF deconvolution are discussed in Chapter 6.

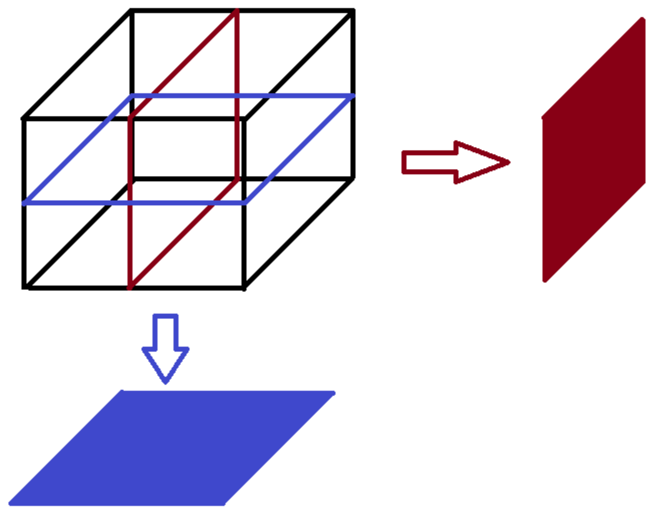

Figure 5.12: Central Slice Theorem schematic: Two slices correspond to two projections at different directions. The 2-D Fourier transform of the red image is equal to the red slice through the origin of the 3-D Fourier transform of the data cube that is also perpendicular to the projection direction. Same for blue image and blue slice.

The back projection can also be analyzed in Fourier space. According to Fourier slice theorem (central slice theorem), the 2-D Fourier transform of each projection is equal to a slice through the origin of the 3-D Fourier transform of the original data cube. The slice in the Fourier space is perpendicular to the direction of projection, as shown in Fig.5.12. Mathematically, we can show without loss of generality that we can choose the Cartesian coordinates system in a way such that the projection is along the z direction, and the projection can be described by Eq.5.12.

$$p(x, y) = \int I(x, y, z)\,\mathrm{d}z \tag{5.12}$$

$I(x, y, z)$ is the original data cube, whose 3-D fourier transform is shown in Eq.5.13

$$F(k_x, k_y, k_z) = \iiint I(x, y, z)\mathrm{e}^{-2\pi i(xk_x + yk_y + zk_z)}\,\mathrm{d}x\mathrm{d}y\mathrm{d}z \tag{5.13}$$

Then the slice that is perpendicular to the projection and across the origin of Fourier space is $S(k_x, k_y)$

$$
\begin{aligned}
S(k_x, k_y) = F(k_x, k_y, 0) \\
&= \iiint I(x, y, z) \mathrm{e}^{-2\pi i (x k_x + y k_y)} \, \mathrm{d}x \mathrm{d}y \mathrm{d}z \\
&= \iint \left(\int I(x, y, z) \, \mathrm{d}z \right) \mathrm{e}^{-2\pi i (x k_x + y k_y)} \, \mathrm{d}x \mathrm{d}y \\
&= \iint p(x, y) \mathrm{e}^{-2\pi i (x k_x + y k_y)} \, \mathrm{d}x \mathrm{d}y \\
&= F_2[p(x, y)]
\end{aligned}
\tag{5.14}
$$

where $F_2[p(x,y)]$ indicates the 2-D Fourier transform of the projection $p(x,y)$. Eq.5.14 gives a simple proof of the Fourier slice theorem for a particular choice of coordinate systems. And general choices of coordinate systems can be thought of a rotation of the data cube object or a change of basis, which is still subject to our proof [105].

According to Fourier slice theorem, the back projection of a grism-dispersed image is equivalent to adding a central slice in Fourier space. Since the projection angle β is a constant for the projection and back projection process, all grism-dispersed images will form slices in Fourier space with the same tilted angle, as shown in Fig.5.13. There are only five slices in Fourier space in Fig.5.13 which corresponds to the reconstructed cube from 5 projections. A lot of regions in the Fourier space are still missing, and the information is incomplete. As we start to increase the number of projections N_{proj}, the slices will gradually fill up the Fourier space except for two conical regions in the center. These slices become the envelope of the missing conical regions in Fourier space. A direct result is that there is an inevitable information loss due to the missing conical regions in Fourier space no matter how many projections we use.

I want to clarify that the missing conical regions in Fourier space are different from the double cone PSF mentioned earlier in this Chapter. First, the missing conical regions are discussed in Fourier space, while the double cone PSF is discussed in real space. Second, although both are double conical structures, the missing conical regions are filled double cones, while the PSF is the surface of double cones.

The Fourier slice theorem also states in our case that, the missing conical regions are larger if we choose a small projection angle β. By our definition, the missing cone angle ψ and the projection angle β are complementary $\psi + \beta = 90°$. A smaller β and larger ψ results in a larger missing cone and more missing information, reducing the FWHM as shown in Fig.5.14. The larger the missing cone angle ψ, the wider the spectrum of a monochromatic point source. So we want a larger β to reduce the missing information.

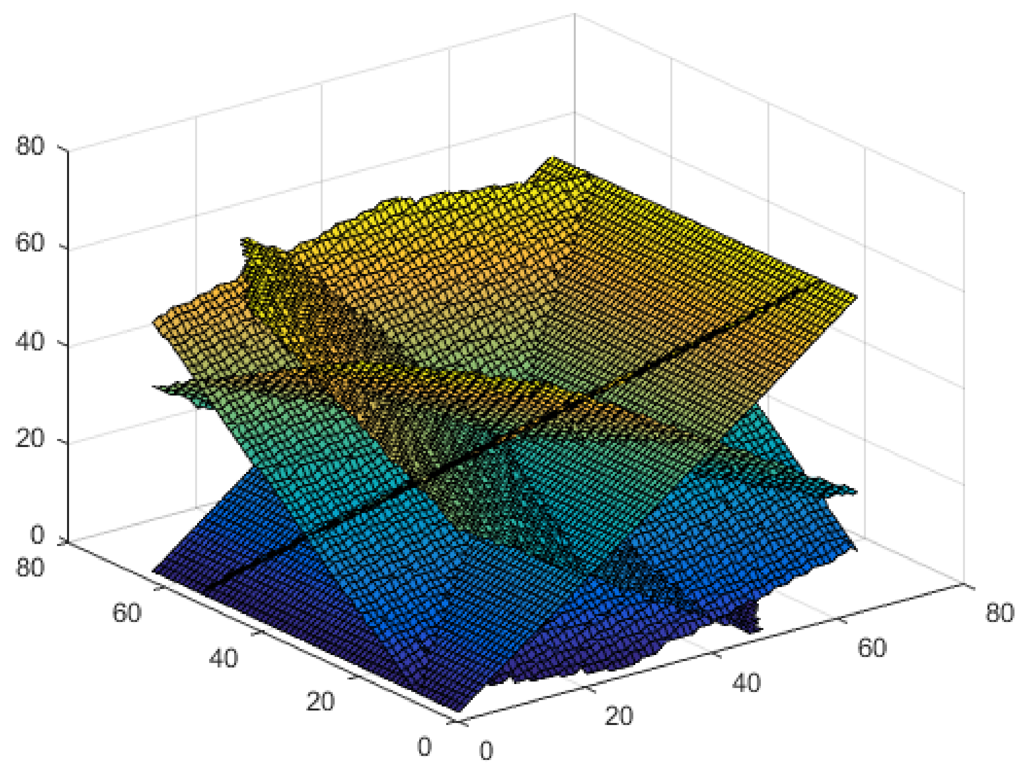

Figure 5.13: Missing information due to Fourier Slice Theorem, with only five projection slices. Each slice in the Fourier space corresponds to a projection in real space. The empty part in the Fourier space is the missing information. A missing double cone will be built up as slice density increases.

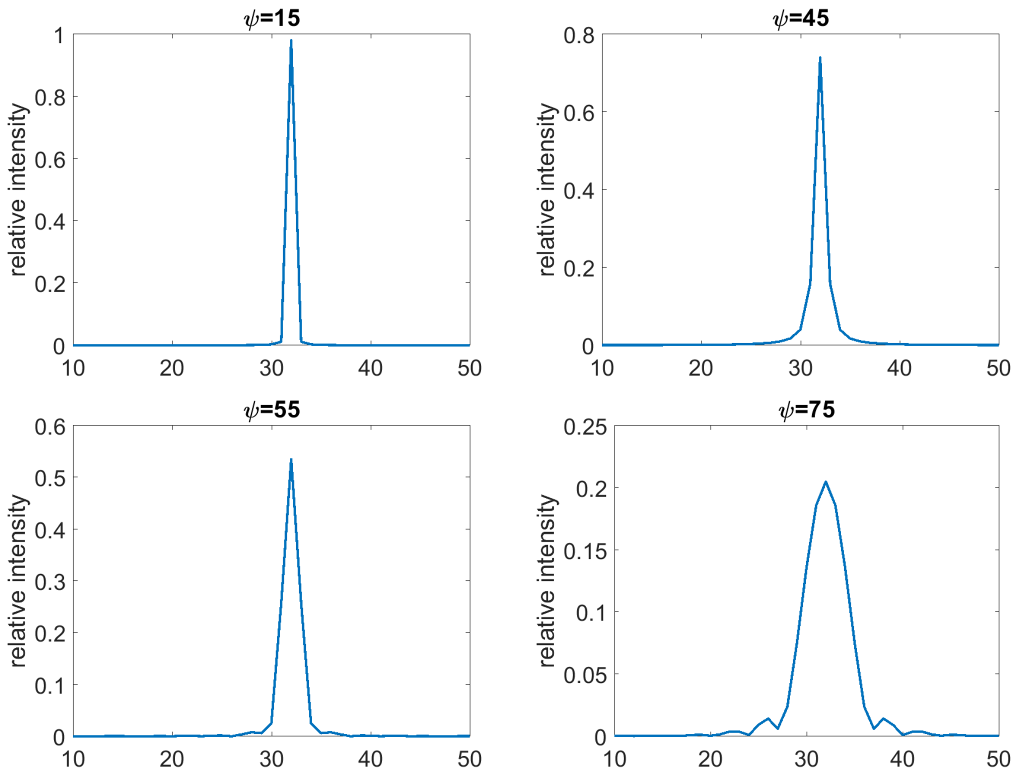

Figure 5.14: Spectrum of monochromatic point source spectrum with missing conical regions in Fourier space. In the Fourier space of this synthetic one-voxel-large source, a double cone of angle $\psi = 15°$, $45°$, $55°$ and $75°$ is set to zero respectively. This corresponds to projection angle $\beta = 75°$, $45°$, $35°$ and $15°$.

5.4 Conclusion

In this chapter, I discussed the imaging model of my GSTI and the back projection algorithm. A grism-dispersed image can be modeled as the projection of the data cube from parallel rays onto the sensor plane, which is closely related to tomography. I proposed a two-step algorithm for the reconstruction: the back projection and the PSF deconvolution. I focused on the back projection algorithm in this chapter, which directly inverts the projection process and tries to put the source at the right location. However, I explained using Fourier slice theorem that this grism technique suffers from incomplete information during the image acquisition process. Finally, I calculated the spectral resolution based on the model and the back projection algorithm. To combine the argument of missing conical region and Eq.5.11, I choose $\beta = 45°$ as the projection angle for all the later analysis in this thesis. A better choice may be attained through further analysis of FWHM and Fourier space.

Chapter 6

Deconvolution Techniques

Two deconvolution techniques are discussed and analyzed in this Chapter, the direct Fourier deconvolution and the Richardson-Lucy (RL) deconvolution. I also tried other common deconvolution techniques including Wiener deconvolution, regularized deconvolution, and blind deconvolution. Wiener deconvolution is the general case of the Fourier method, and it does not yield good results in the experiments when there is no noise present. Regularized deconvolution can impose sparsity on the solution and achieves similar results as RL method, but it requires more computation resources. Blind deconvolution usually works well when the PSF is not known, but the PSF is modeled accurately using double cone in this Chapter. I chose RL deconvolution in the thesis because it gives best results with fast computation, and it proves effective when applied to Hubble Space Telescope images [106].

This chapter is outlined as follows:

- I describe the Fourier deconvolution and the Richardson-Lucy deconvolution.
- I test the deconvolution techniques with simulated monochromatic point sources. There are three scenarios: 1) single point source with different intensities; 2) single point source at different locations; 3) double point sources with different intensity ratios.
- I define and calculate recovery factor and RMS scattered intensity after deconvolution, based on deconvolution results at different locations in the cube.
- I define the truncation factor and show that it affects the recovery factor after deconvolution. And calibration needs to be carried out to correctly recover the intensity of the source.
- I test the deconvolution techniques with simulated Lyα emitters from MassiveBlack-II(MBII) simulation and stars using a model M-star template. There are two scenarios for stars: 1) only one star at the center of the cube with a range of brightnesses; 2) stars using observed positions and brightness from SDSS.

- I describe and test two star masking methods: 1) masking stars on grism-dispersed images; 2) masking stars at the image plane.

A typical deconvolution problem can be described by the following equation:

$$O = P * I + \epsilon \tag{6.1}$$

where P is the PSF, I is the underlying true image, $*$ stands for the convolution operator, ϵ is the noise added to the image, and O is the image we observe. The problem is to find I, given observed image O and an assumed PSF P. In this thesis, O is obtained either by back-projecting the set of grism-dispersed images or simulated based on the PSF, and P is the double-cone PSF described in Chapter 5.

For images or data cubes, Eq.6.1 can be discretized into the following form:

$$O(i) = \sum_j P(i,j)I(j) + \epsilon \tag{6.2}$$

where $O(i)$ is the ith pixel of the observed image O, $I(j)$ is the jth pixel of true image I, and the PSF $P(i,j)$ can be viewed as the fraction of light at j being scattered into pixel i.

6.1 Fourier Deconvolution

Fourier deconvolution is based on the fact that convolution in the real domain is mathematically equivalent to multiplication in Fourier domain, which is stated as the convolution theorem:

$$\mathcal{F}(f * g) = \mathcal{F}(f) \times \mathcal{F}(g) \tag{6.3}$$

where $\mathcal{F}$ stands for Fourier transform operator, so $\mathcal{F}(f)$ and $\mathcal{F}(g)$ are the Fourier transform of f and g respectively. Applying the convolution theorem to Eq.6.1, the solution can be written as:

$$I = \mathcal{F}^{-1}(\frac{\mathcal{F}(O) - \mathcal{F}(\epsilon)}{\mathcal{F}(P)}) \tag{6.4}$$

where $\mathcal{F}^{-1}$ is the inverse Fourier transform operator. Often, the noise term is not known well and an estimate is usually made by ignoring the noise:

$$\tilde{I} = \mathcal{F}^{-1}(\frac{\mathcal{F}(O)}{\mathcal{F}(P)}) \tag{6.5}$$

This is the formula for Fourier deconvolution, which states the deconvolved data cube $\tilde{I}$ is obtained simply through dividing the back-projected data cube O by PSF P in Fourier domain and then transforming it back to the real domain. A major problem of this technique is, as can be seen from Eq.6.5, the noise is ignored, which results in many artifacts especially in low signal-to-noise images. Another common problem of Fourier deconvolution is the ringing artifact that results from the sharp edges of images. Thus Fourier deconvolution is not usually the best method for deconvolution, but a benchmark for other techniques.

In general, if we do not ignore the noise term, we can derive Wiener deconvolution by minimizing the mean square error between the actual image and estimate image. The Wiener deconvolution is shown in Eq.6.6.

$$\tilde{I} = \mathcal{F}^{-1}(\mathcal{F}(O) \times \frac{1}{\mathcal{F}(P)}\Big[\frac{|\mathcal{F}(P)|^2}{|\mathcal{F}(P)|^2 + \frac{1}{\mathcal{F}(SNR)}}\Big]) \tag{6.6}$$

where SNR stands for the signal-to-noise ratio. When the noise is zero, the signal-to-noise ratio is infinite and the term inside the square brackets equals 1. Thus in the noiseless case, Wiener deconvolution is just the inverse of the system depicted in Eq.6.5. On the other hand, a nonzero signal-to-noise ratio indicates the signal attenuation at that frequency.

6.2 Richardson-Lucy

Richardson-Lucy deconvolution is an iterative method for recovering a latent image blurred by a known PSF, William Richardson and Leon Lucy [107, 108]. Richardson-Lucy method maximizes iteratively the likelihood of the resulting image given the observed convolved image and the PSF, converging to maximum likelihood estimate only if the iteration converges [109].

Following the derivation of R. L. White [110], L.A Shepp and Y. Vardi [109], let's denote the noiseless image after convolution as N based on Eq.6.2:

$$N(i) = \sum_j P(i,j)I(j) \tag{6.7}$$

where $N(i)$ is the ith pixel of the noiseless blurred image. If we assume the noise in images follow Poisson distribution, the observed photon counts for each pixel have the following conditional probability:

$$P(O(i)|N(i)) = \frac{e^{-N(i)}N(i)^{O(i)}}{O(i)!} \tag{6.8}$$

So the joint likelihood and corresponding log-likelihood function of observed images given true images are:

$$\mathcal{L} = \prod_i P(O(i)|N(i)) = \prod_i \frac{e^{-N(i)}N(i)^{O(i)}}{O(i)!} \tag{6.9}$$

$$\ln \mathcal{L} = \sum_i [O(i) \ln N(i) - N(i) - \ln O(i)!] \tag{6.10}$$

The likelihood function can be maximized through the Expectation Maximization (EM) algorithm [111]:

$$\begin{aligned} I_{new}(j) &= I_{old}(j)\frac{\sum_i P(i,j)\frac{O(i)}{N(i)}}{\sum_i P(i,j)} \\ &= I_{old}(j)\frac{1}{\sum_i P(i,j)}\sum_i \frac{P(i,j)O(i)}{\sum_j P(i,j)I_{old}(j)} \end{aligned} \tag{6.11}$$

It has been shown that EM algorithm under Poisson statistics is equivalent to Richardson-Lucy algorithm [109], and the iterative algorithm converges to the maximum likelihood estimate (MLE) of Poisson distribution. This can also be seen from the Eq.6.11, where the correction factor approaches unity as the iteration converges to MLE.

Richardson-Lucy method has the advantage of forcing the reconstructed image to be non-negative and conserving the total flux at each iteration. It also shows robustness against small errors in PSF. Despite these advantages, RL has serious noise amplification and numerical instability problems, because it attempts to reproduce the data as closely as possible.

One solution to prevent noise amplification is to use a damped RL iteration [110]. The damped RL iteration chooses a threshold at which the damping turns on and makes the likelihood function close to constant in the vicinity of a good estimate. If the difference between the restored image and the observation is less than the threshold, the correction is damped; otherwise the correction follows the standard RL iteration described in Eq.6.11. It is essentially reducing the changes in regions where the restored image fits the data well, while continuing to update the regions where it fits badly. Acceleration techniques can also be applied to damped RL method to speed up the iterations [112].

There are no automatic methods of choosing the damping threshold for damped RL iteration, so several experiments are performed to determine this parameter. I created a simulated back-projected data cube with only a double-cone truncated by the edge of data volume for testing, which corresponds to the convolution of a single-voxel point source with the PSF as shown in Fig.6.3. The data cube has a size of 300*300*300 voxels, and the point source locates at (135,135,135) under Cartesian coordinates with two cones extending along z directions. The test assumes back projection angle $\beta = 45°$, which is also the cone angle. The test also assumes reconstruction from 100 discrete grism angles, i.e., 100 projections based on my back projection model.

The source intensity against iterations for different damping thresholds are plotted in Fig.6.1 and Fig.6.2. We notice that when the threshold is set large, the resulting intensity does not converge or it converges to an incorrect value, because some necessary updates are damped due to large thresholds. On the other hand, when the threshold is small as 10^{-9}, it does not help to slow down the updates and intensity

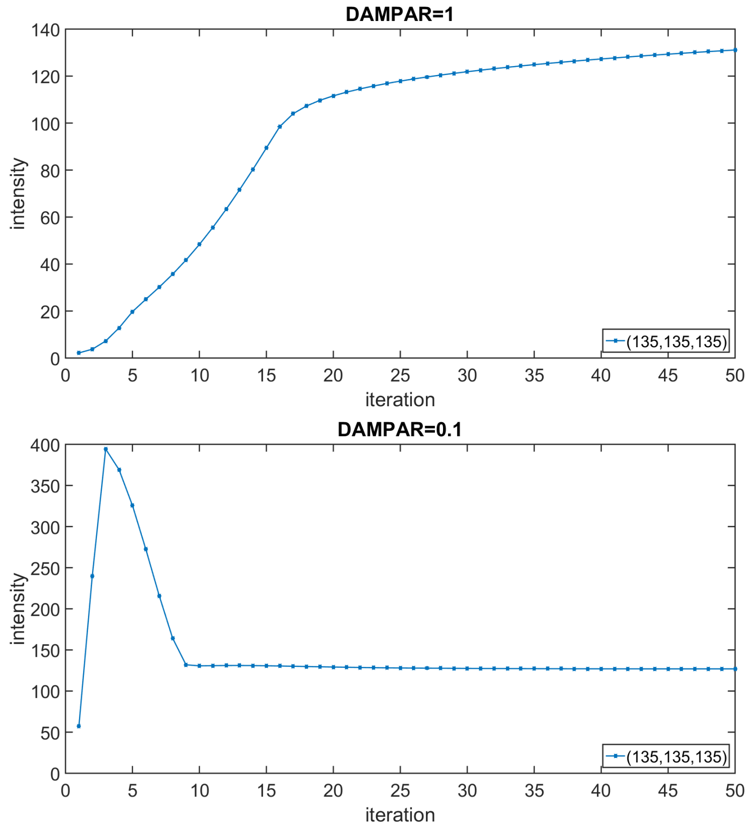

Figure 6.1: The source intensity vs. iterations of RL method for different damping thresholds denoted by DAMPAR $= 1, 0.1$ respectively. The source is located at (135,135,135) with initial intensity 1, and there are 50 iterations for each figure.

vanishes due to numerical instability. I choose the threshold to be 10^{-4} which shows stable convergence. And all other RL deconvolutions performed later in this thesis are set to stop at 10 iterations because of fast convergence.

6.3 Test with Simulated Point Sources

To better understand how the deconvolution techniques work for different sources, such as galaxies, stars, and Lyman alpha emitters, I tested the techniques under several basic scenarios. I start with a monochromatic point source and analyze the deconvolution results for different initial locations and intensities. Back-projected point sources are created from putting double-cones at source locations, which is almost equivalent to the convolution of a single-voxel point source with the PSF depicted in Fig.6.3. The difference is that double-cones are truncated by the edge of data volume when the source is located closer to the edge of the data volume. As we will see in the later analysis, this double-cone is the major issue for the whole

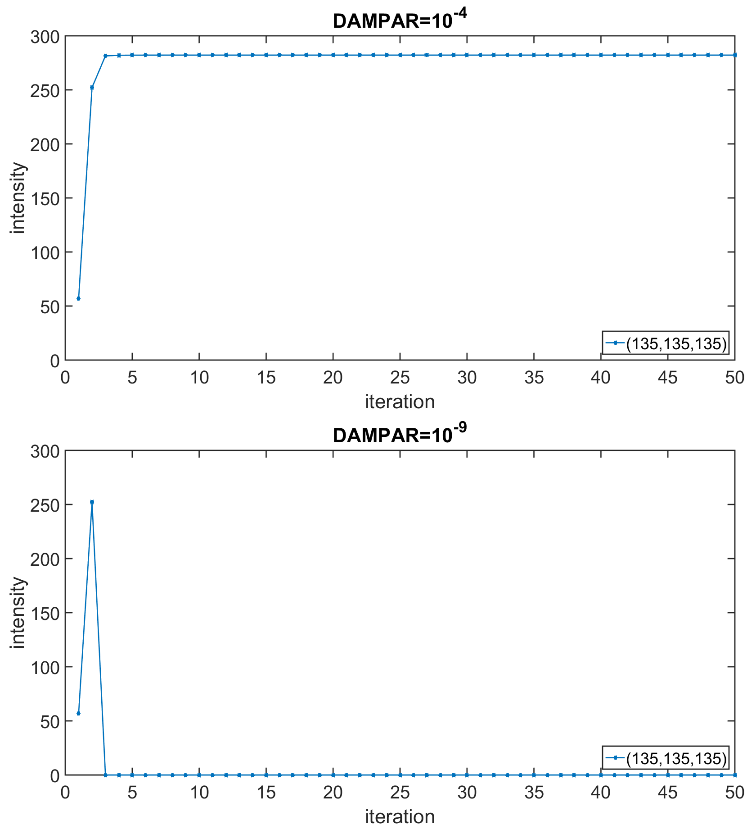

Figure 6.2: The source intensity vs. iterations of RL method for different damping thresholds denoted by DAMPAR $= 10^{-4}, 10^{-9}$ respectively. The source is located at (135,135,135) with initial intensity 1, and there are 50 iterations for each figure.

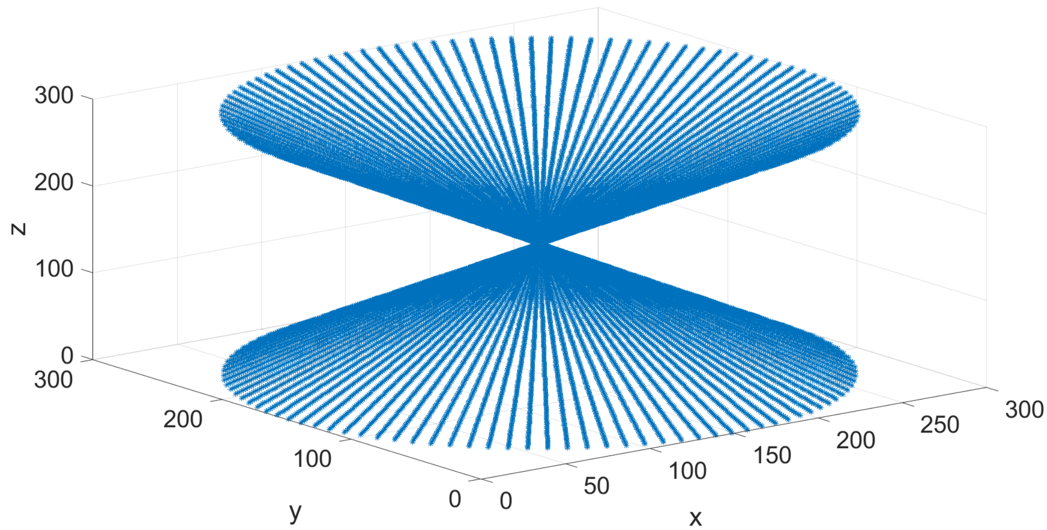

Figure 6.3: A double-cone PSF with source located at (150,150,150).

deconvolution problem. Since the back projection puts the same amount of intensity at each z for any monochromatic point source, it brings $(L_z - 1)$ times more intensity into the cube if the cube's length in z direction is L_z. In other words, there are $(L_z - 1)$ units of intensity at wrong voxels, for each unit at the correct voxel. It is extremely hard to remove or restore this extra amount of intensity. The steps of testing with simulated point sources are:

1. Create simulated back-projected point sources by putting double-cones at source locations.

2. Conduct deconvolution using both techniques on a single point source that has various intensities.

3. Conduct deconvolution using both techniques on a single point source that is at different locations.

4. Calculate calibration factors for intensity after deconvolution.

5. Conduct deconvolution using both techniques on two point sources that have various intensity ratios.

Two metrics are used to measure the performance of the deconvolution: recovery factor and Root-Mean-Square (RMS) value of scattered intensity.

6.3.1 Recovery Factor

I define recovery factor as the ratio of point source intensity after deconvolution to intensity before deconvolution:

$$\text{recovery factor} = \frac{\text{source intensity after deconvolution}}{\text{source intensity before deconvolution}} \times \frac{1}{L_z} \tag{6.12}$$

where L_z is the normalization factor defined as the length of the cube in z direction. Back-projection places an equal amount of intensity at each z for a given monochromatic point source in the form of PSF, and deconvolution attempts to recover its true intensity from the back-projected data. Ideally, deconvolution should put all the intensity in the double cone back at the actual source location, and give rise to the same recovery factor for all locations in the data cube. Thus the normalization factor is $L_z = 300$, and the perfect deconvolution should have a recovery factor of 1 at all voxels, given the cube size $300 * 300 * 300$. But the truncation of the double cone and flaws in deconvolution techniques prevent this perfect recovery factor from happening.

6.3.2 RMS Value of Scattered Intensity

RMS value of scattered intensity indicates the average intensity at locations other than the source location due to scattering of our reconstruction techniques. It is computed by taking the average of squared intensity in all voxels other than the point source, and taking the square root of the average. In the case of a single point source, it takes the average over $300^3 - 1$ voxels in our tests.

For simulated data, the scattered intensity comes from flaws in deconvolution techniques, and shape mismatch between back-projected double cone and PSF due to truncation. For observed data, there is also noise contribution to the scattered intensity. I mainly focus on simulated data in this Chapter.

6.3.3 Truncation Factor

I define the truncation factor of a point source as the fraction of PSF intensity remained in the cube due to truncation. An example of truncation is shown in Fig.6.4

$$\text{truncation factor} = \frac{\text{PSF intensity remained in the cube}}{\text{source intensity} \times L_z} \tag{6.13}$$

where L_z is the same normalization factor defined above, and PSF intensity means the sum of the intensity over the double-cone PSF. The denominator is equivalent to the intensity of a PSF that is not truncated in x, y dimension. When the source is located closer to the sides of a cube, some parts of the PSF may be cut off by the sides. The truncation factor is 1 if there is no truncation, and is less than 1 otherwise.

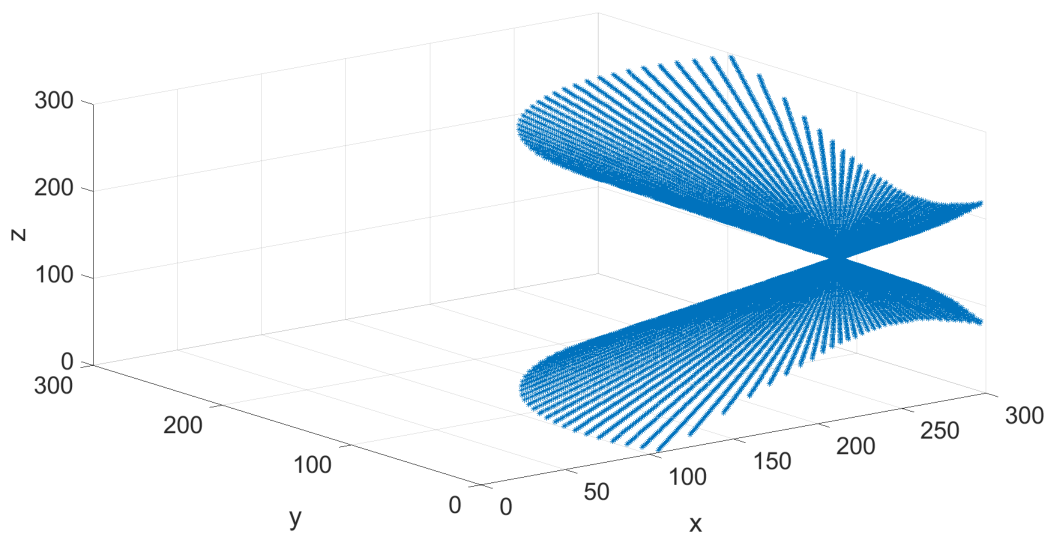

Figure 6.4: A double-cone PSF with source located at (250,50,150). Parts of the PSF are missing due to truncation

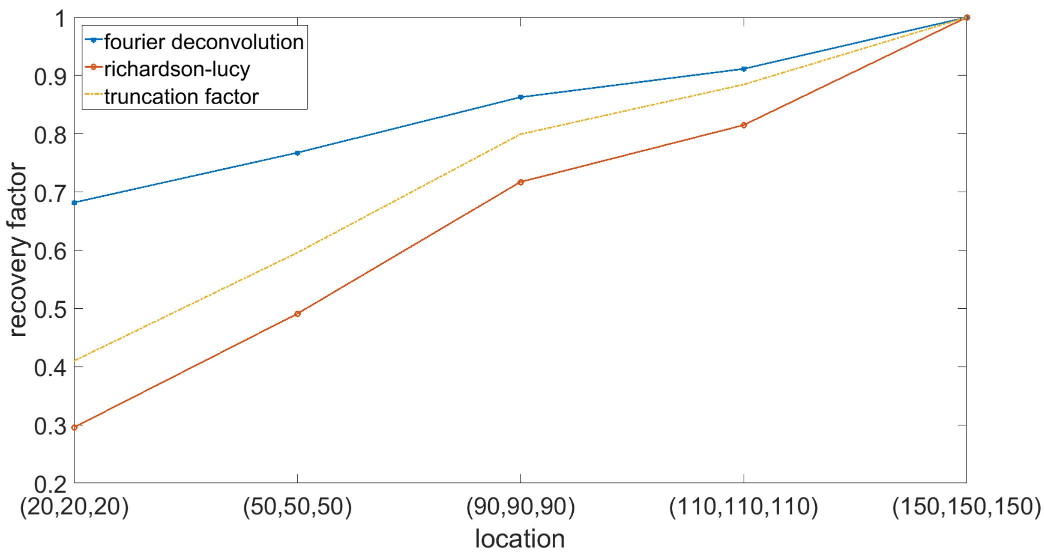

Figure 6.5: The recovery factor of a single PSF after deconvolution with two techniques, where various source locations are used. The recovery factor plot also includes the truncation factor as a comparison.

6.3.4 Test Results

Results of a single point source are not surprising. The double cone located at (150,150,150) results in a recovery factor of 0.99 and an RMS scattered intensity of 0, which means both deconvolution techniques successfully put the scattered intensity back to the actual location of the source and leave no more scattered intensity elsewhere in the cube. The perfect number should be 1, and the difference is accounted for by the numerical accuracy of fast Fourier transform (FFT) in MATLAB. Increasing or decreasing the intensity does not affect the recovery factor and RMS scattered intensity, implying both techniques are linear transforms for a single source.

Recovery factor and RMS scattered intensity start to change as the point source is moving away from the center, shown in Fig.6.5 and Fig.6.6. This is because the double cone is cut off by the boundaries of the cube as the double cone moves closer to the sides of the cube. The cutoff of the double cone also leads to the shape mismatch between the double cone and PSF, causing the deconvolution techniques to scatter the intensity to other voxels while failing to place that intensity at the source location.

This cutoff issue of the double cone results in an intensity deficit which must be corrected, for example, a source located at the center of the cube has a different measured intensity from that same source located at the edge of the cube after deconvolution. Fig.6.7 shows how the truncation factor of the double cone varies at different locations assuming the source has intensity 1. The truncation factor is greatest with a value 1 when the point source is at the center of the cube (150,150,150),

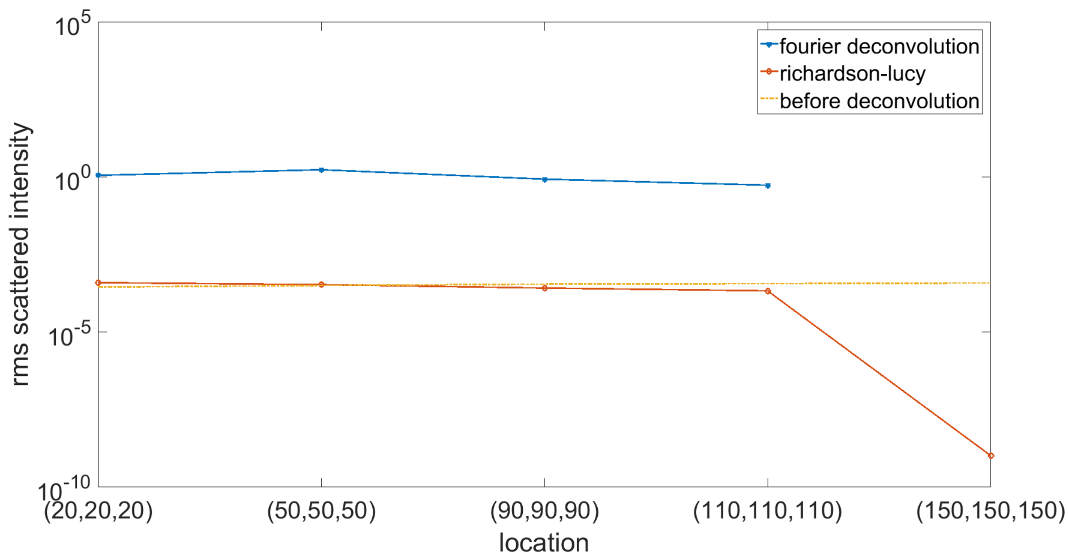

Figure 6.6: The RMS value of the scattered intensity of a single PSF after deconvolution with two techniques, where various source locations are used. The scattered intensity before the deconvolution is also plotted. The 0 RMS value of scattered intensity cannot be displayed on the plot for Fourier deconvolution at location (150,150,150) because the y-axis is log scale.

and decreases non-linearly as the source moves radially away from the center. A calibration factor is required for intensities at every location. If the deconvolution can recover all the scattered intensity in the cube under truncation situations, the calibration can be easily achieved by calculating the remaining intensity of the double cone for a point source at every location. But there is a significant difference between truncation factor and the recovery factor for both deconvolution techniques, shown in Fig.6.5. Calibration needs to be carried out separately for Fourier deconvolution and Richardson-Lucy. It can also be noticed that RMS value of scattered intensity after deconvolution does not vary a lot at different locations except center.

Recovery factor calibration results for Fourier method are shown in Fig.6.8, in a similar fashion as the truncation factor plot in Fig.6.7. Recovery factor calibration results for RL deconvolution are shown in Fig.6.9. Both recovery factors decrease when moving away from the center of the cube, but at different slopes.

Location, rather than intensity, exerts significant influence on the deconvolution performance for a monochromatic point source. However, multiple sources can affect each other during deconvolution, and I test the deconvolution techniques with two point sources located at symmetric locations: dim source at (151,151,140) and bright source at (151,151,160). To test the effect of intensity ratio between two sources, I fix the dim source at intensity 1 and vary the bright source intensity from $1 - 10^9$. The intensities for both dim source and bright source after deconvolution are shown in Fig.6.10. We first notice that the scattered intensity is proportional to the bright source intensity for both techniques, and RL method yields a smaller RMS scattered intensity. For Fourier deconvolution, the intensity of dim source comes mainly from scattered intensity when the bright source is brighter than 1000, which indicates the dim source can not be discovered after this ratio. For the Richardson-Lucy method, the dim source vanishes after the bright source becomes brighter than 1000, implying that dim source is treated as random noise during the deconvolution. Further tests show that results of two point sources experiments rely on their locations, and exhibit a critical point at ratio 1000 on average. As a conclusion, if the intensity ratio of two sources is greater than 1000, then the dim source does not have a high enough signal-to-noise to be discovered or extracted.

6.4 Test with Simulated Lyα Sources

I then use the galaxy star formation rate (SFR) from the MassiveBlack-II (MBII) simulation [113] to test deconvolution techniques with simulated Lyα sources. Experiment steps are outlined as follows:

1. Select a volume in MBII simulation that has the same size as my simulated cube.

2. Build simulated back-projected Lyα sources using SFRs and locations of subhaloes from MBII.

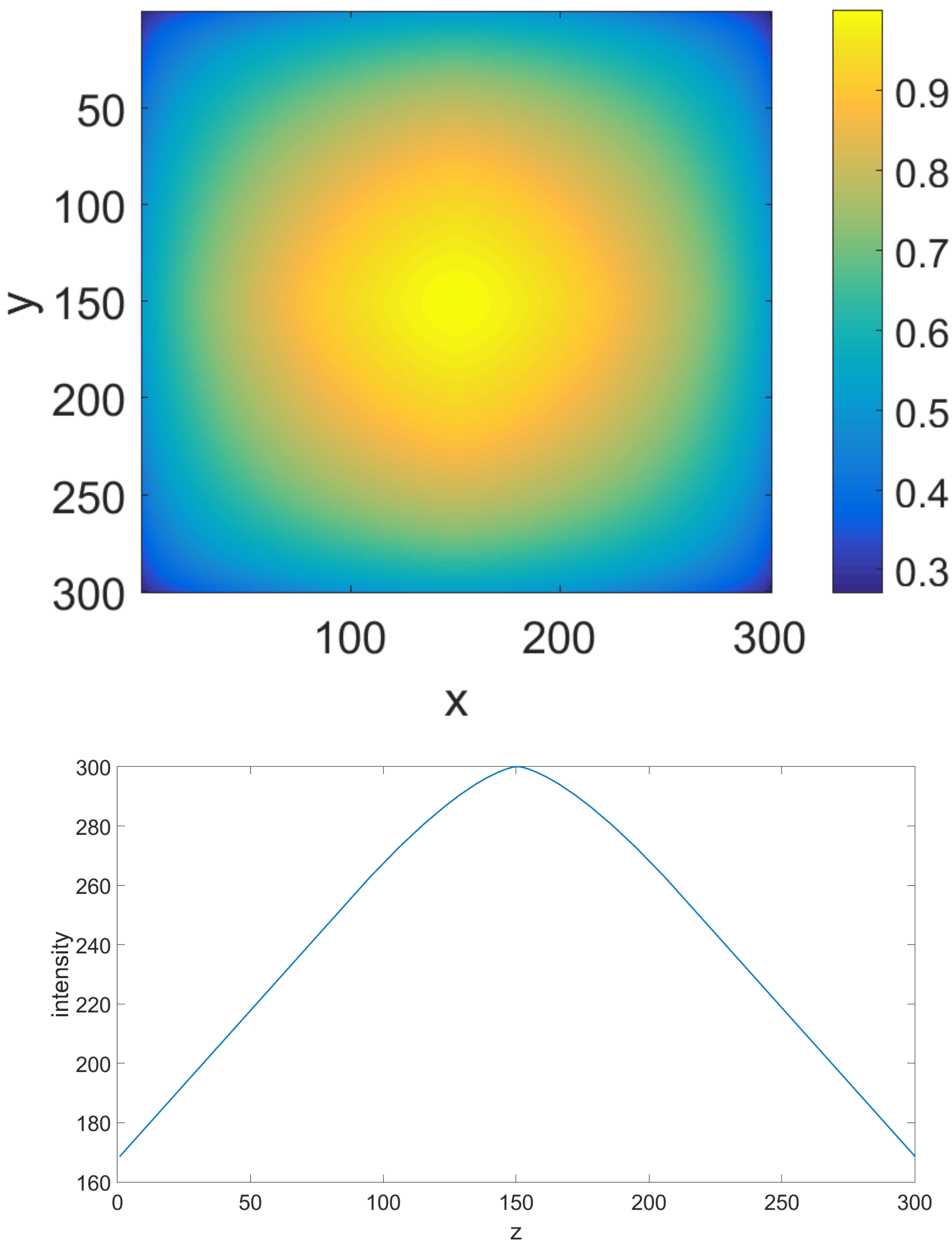

Figure 6.7: The truncation factor due to the cutoff of the cube. The first figure shows the truncation factor if the source locates on a plane where $z = 150$. The second figure plots the truncation factor of the source sits at $x = 150, y = 150$ and along z.

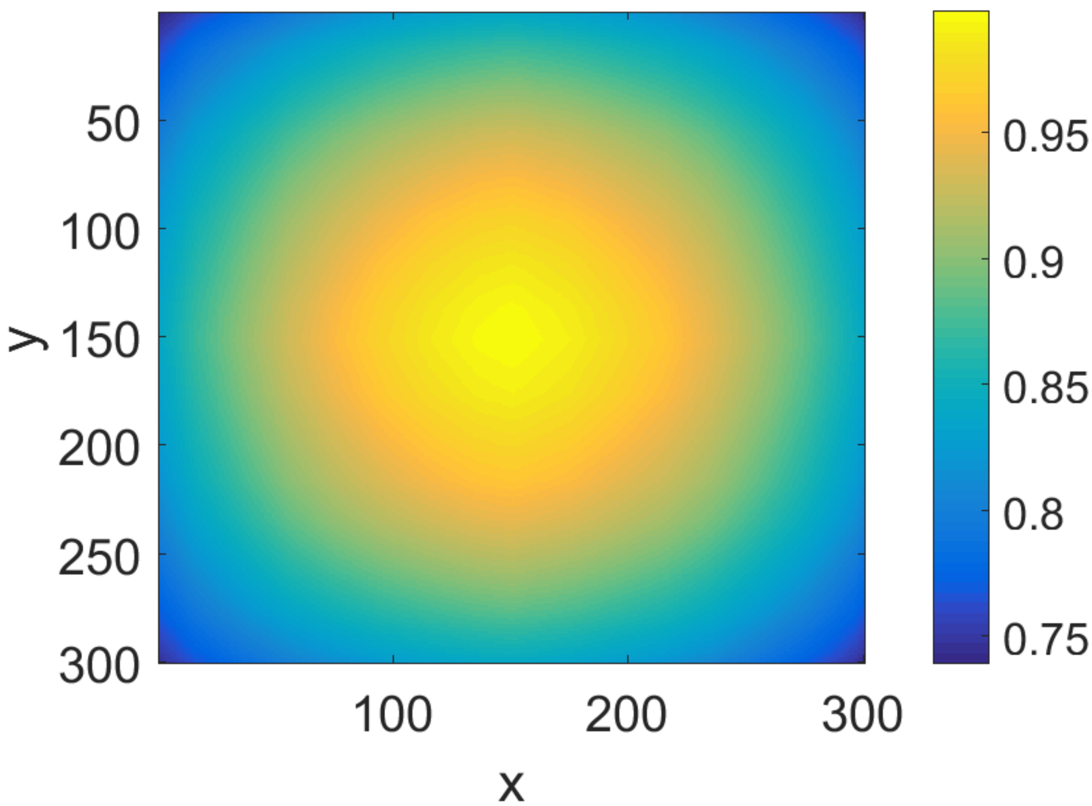

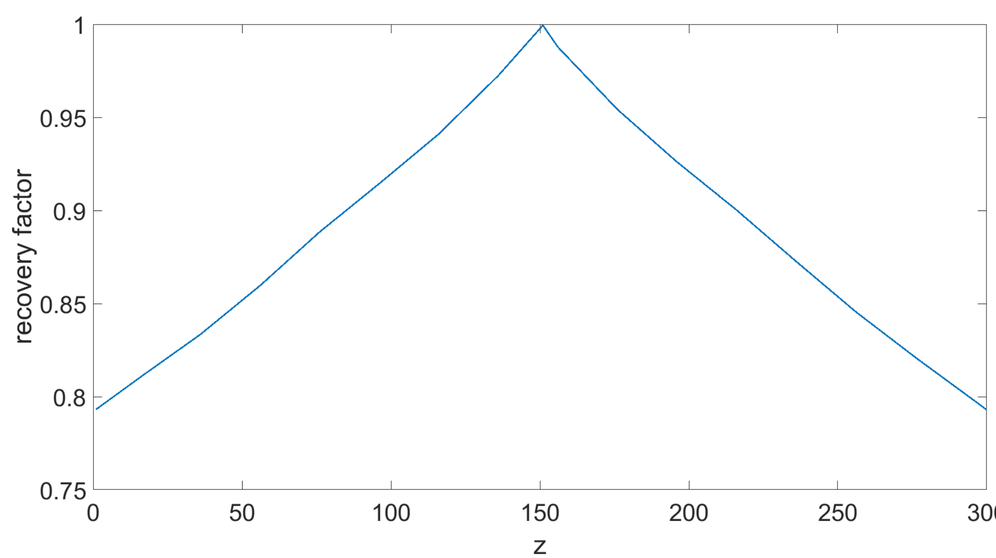

Figure 6.8: Recovery factor calibration result for Fourier method. The first figure shows the recovery factor if the source locates on a plane where $z = 150$. The second figure plots the recovery factor of the source sits at $x = 150, y = 150$ and along z.

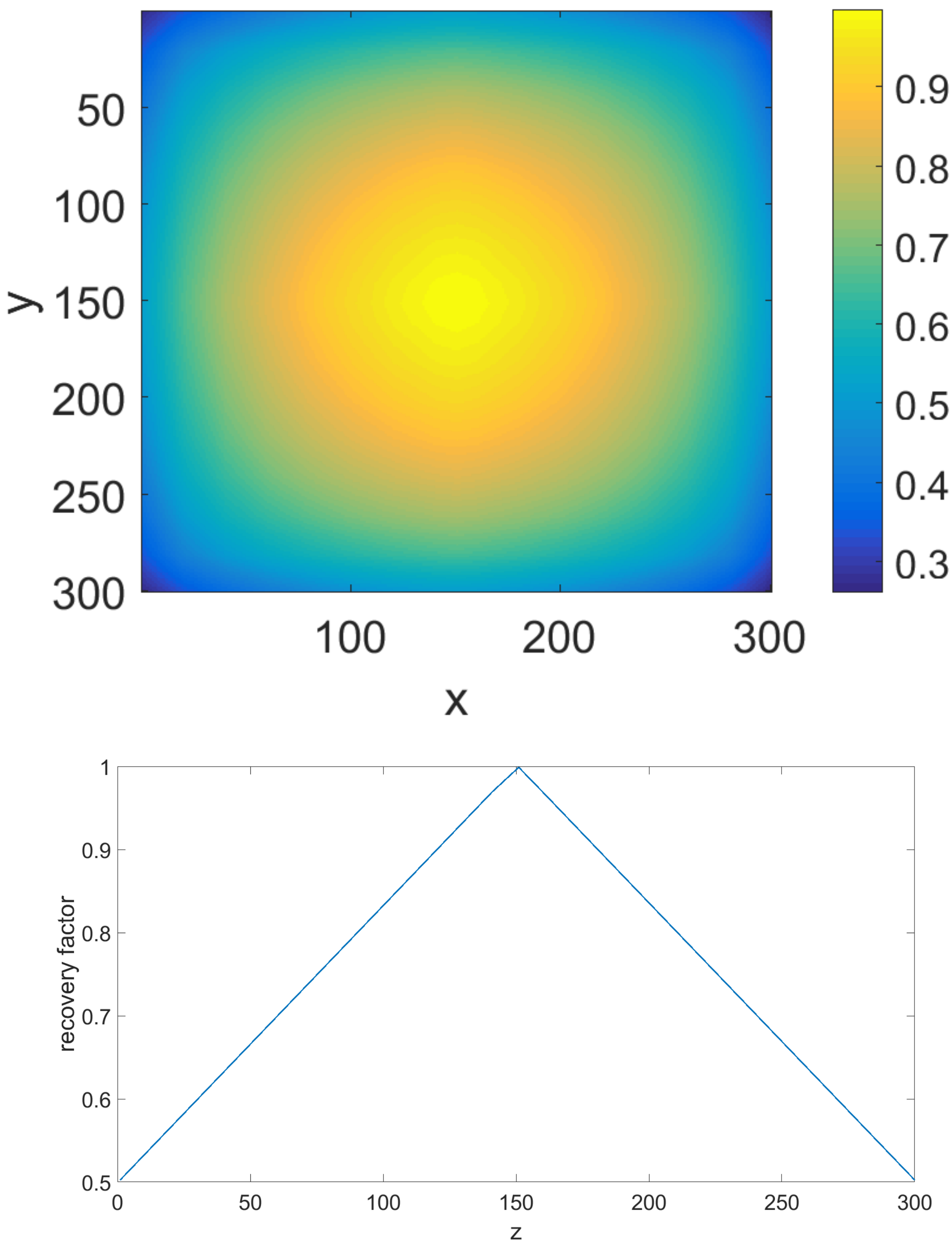

Figure 6.9: Recovery factor calibration result for RL method. The first figure shows the recovery factor if the source locates on a plane where $z = 150$. The second figure plots the recovery factor of the source sits at $x = 150, y = 150$ and along z.

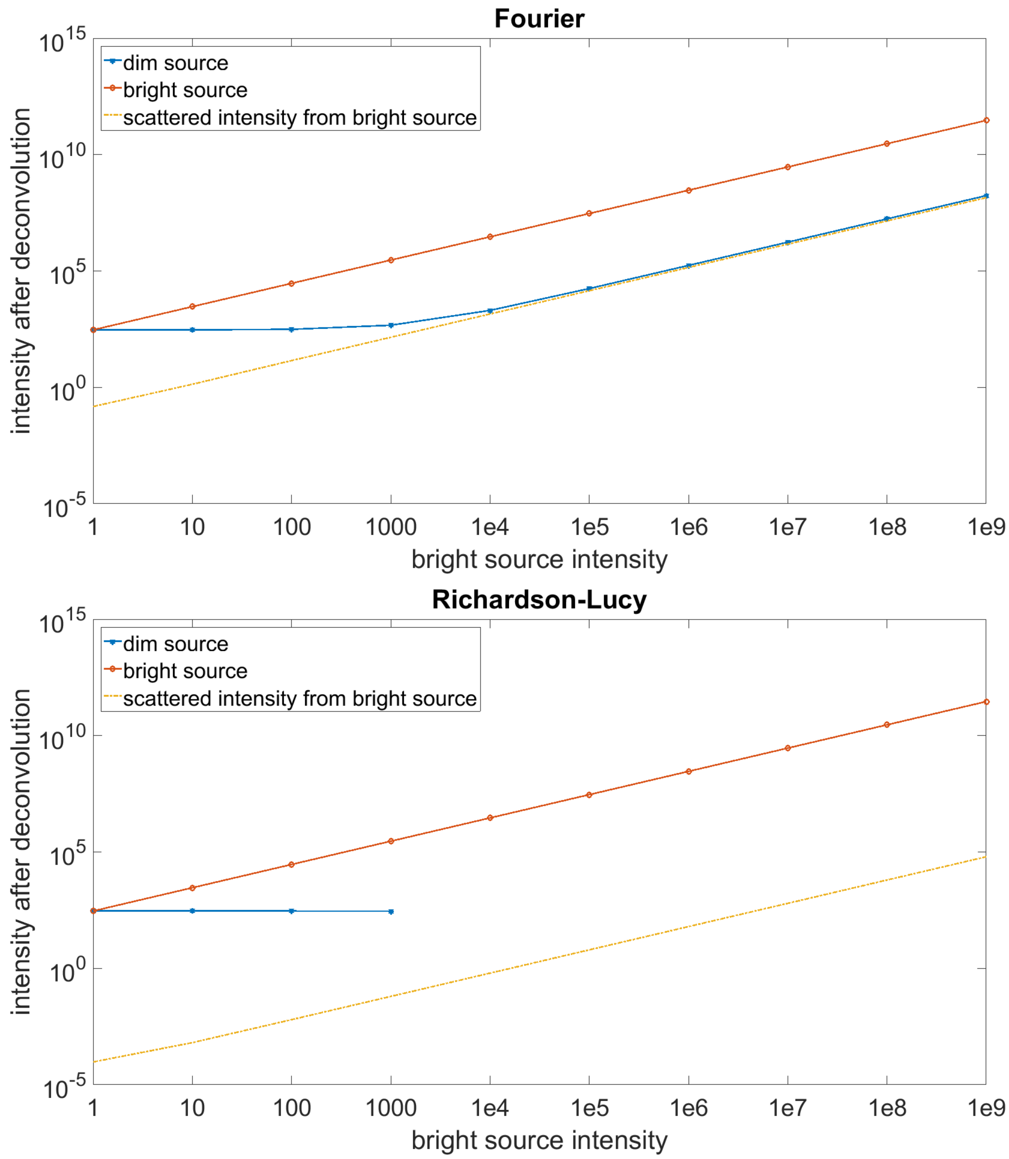

Figure 6.10: The dim source intensity and bright source intensity after deconvolution using Fourier deconvolution(Top) and Richardson-Lucy(Bottom), with different bright source initial intensities. The RMS scattered intensity from bright source is also considered as a comparison. In the bottom plot, dim source intensity vanishes when the bright source intensity is greater than 1000. The 0 intensity cannot be seen in the plot because y-axis is log scale.

3. Conduct deconvolution using both techniques on simulated Lyα sources.

4. Intensity calibration is done after deconvolution.

MBII is a high-resolution hydrodynamical simulation that evolves a Λ cold dark matter cosmology in a comoving volume $V_{box} = (100 \text{ Mpc } h^{-1})^3$. The SFR is proportional to Lyα emission and hence can be used to provide the Lyα intensity. If the star-forming galaxies dominate Lyα emission, the estimated Lyα surface brightness according to Croft et al. is $\mu = (3.9 \pm 0.9) \times 10^{-21} \text{ergs}^{-1}\text{cm}^{-2}\text{Å}^{-1}\text{arcsec}^{-2}$ and corresponding to SFR density $\rho_{sfr} = (0.28 \pm 0.07)\text{M}_{\odot}\text{yr}^{-1}\text{Mpc}^{-3}$ [98]. I used the positions of subhaloes and their corresponding star formation rates from the MBII to describe the distribution of Lyα emitters on the sky as well as their brightness.

Based on the resolution of reconstructed images, I chose a cube of size 23 Mpc from the MBII, which I scaled to a 300*300*300 cube described before. There are a total of 26585 subhaloes in this volume, and a simulated back-projected data cube is built from them. The average intensity of back-projected subhaloes is scaled to match the result of Croft et al. results [98] in units of pW $\text{m}^{-2}\text{nm}^{-1}\text{sr}^{-1}$. The distributions and deconvolution results of these simulated Lyα sources are shown below in Fig.6.11-Fig.6.13.

Fig.6.11 shows the simulated Lyα emitters in xy plane by projecting the data cube in the z-direction. The bubble plot on the top comes from the true data cube we are hoping to reconstruct, while the figure on the bottom is the simulated back-projected data cube we reconstruct from. Most of the bright sources are located at the top left of the image. The lines in the right figure of Fig.6.11 are from the double-cone structures, which also make the regions surrounding Lyα emitters brighter.

The Fourier deconvolution results for this simulated Lyα emitters are shown in the Fig.6.12. The figure at the top is again the projection of the deconvolved data cube in the z-direction. The stripes in the images are the artifacts from the Fourier methods, and only a few bright sources can be spotted with confidence. A majority of the dim sources are confused with the scattered intensity in the cube, which can also be shown by the plot at the bottom. A few brightest sources are properly reconstructed and have intensity before deconvolution proportional to intensity after deconvolution. The perfect deconvolution reference line describes the best deconvolution result of any source, which is 300 times the intensity before deconvolution in this experiment. Brightest sources lie close enough to this line, but they do not reach the perfect deconvolution because of the scattered intensity from other sources. On the other hand, Lyα emitters with intensity lower than 10^2 are around the RMS scattered intensity, so that they can not be distinguished from the scattered intensity. The strange shape at the left sides of the plot indicates most dim sources are dominated by scattered intensity. Fourier deconvolution is an intensity conservation process that cannot remove extra intensity, so the intensity from PSF is scattered to the wrong locations. The scattered intensity mainly comes from a few brightest sources and are 1000 times dimmer than the brightest source, which is consistent with the results

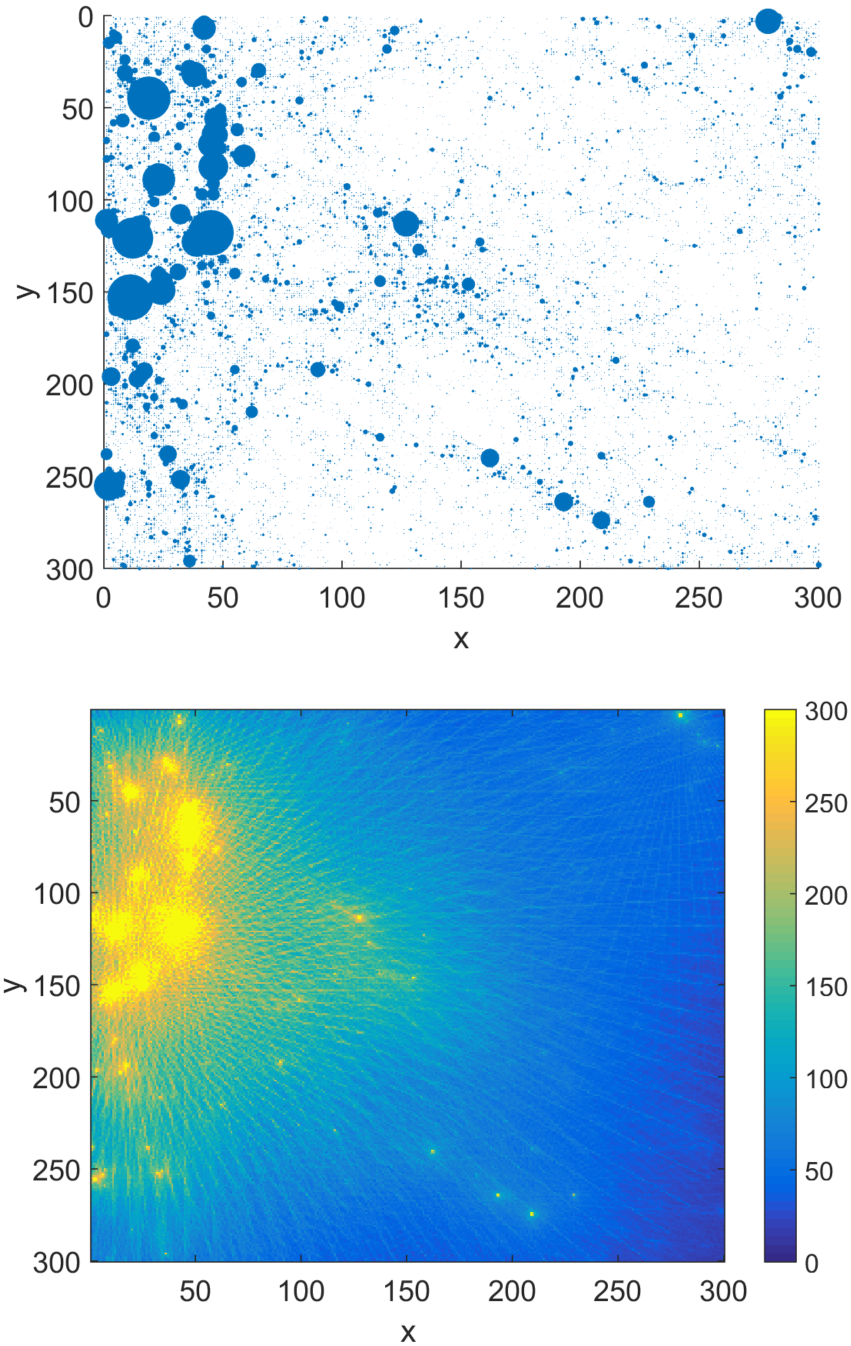

Figure 6.11: Simulated Lyα sources from MBII. **Top**: The bubble plot of true data cube containing Lyα sources summed up in the z-direction. Area of the circle is proportional to the brightness. **Bottom**: The simulated back-projected data cube with Lyα sources is summed up in z-direction.

about recovery factor and RMS value of scattered intensity in Section 6.3. There are negative voxels in the resulting cube, which are not shown in the plots.

In Fig.6.13, I show the Richardson-Lucy deconvolution results which are much better regarding scattered intensity. On the top plot, we can spot a lot of sources that are present in the true data cube. Although the reconstructed data cube is less blurred after deconvolution, there are still visible lines from double cone structures remaining in the cube. These lines are the major components of scattered intensity and also come from the brightest sources. The plot on the right indicates that RMS value of scattered intensity is three orders of magnitude less than the results of Fourier deconvolution. The Lyα sources form an overall linear shape in the plot, indicating the final intensity is proportional to the initial intensity, and the scattered intensity does not affect most of the sources. This shape is different from Fourier deconvolution results because RL method does not conserve the total energy during the process. Thus some extra intensity is removed from the data cube, and the scattered intensity is smaller. The perfect deconvolution reference line is defined the same as above, 300 times the source intensity before deconvolution. And we can again spot the line on the right, formed by a few brightest sources. The fact that these bright sources are close to the perfect deconvolution line indicates they are properly reconstructed despite the effect of scattered intensity. Lyα emitters with an intensity greater than 10 can be distinguished from the scattered intensity, again consistent with the result from Section 6.3.

The deconvolution results of only simulated Lyα emitters imply that dim Lyα emitters can not be detected even without the presence of other bright objects. Although RL technique is more promising in removing scattered intensity and recovering true intensities, it is not good enough to handle bright and dim sources together.

6.5 Test with Simulated Lyα Sources and Stars

One more step closer to the reality is to bring stars into my simulation. Since red dwarf is the most common type of star in Milky Way, I use an M-star spectrum template [15] to simulate the star in my experiments. The M-star spectrum is tailored to span wavelength range $350nm - 614nm$. The star appears as a line in the hyperspectral data cube, where the intensity variation along the z-direction(λ-direction) corresponds to its spectrum. In the simulated back-projected data cube, a double-cone is placed at each λ of the star, and its intensity is converted to the same unit as Lyα emitters. Without loss of generality, the simulated star is placed at the center of the cube, as shown in Fig.6.14. Experiment steps are outlined as follows:

1. Select a volume in MBII simulation that has the same size as my simulated cube.

2. Build simulated back-projected Lyα sources using SFRs and locations of subhaloes from MBII.

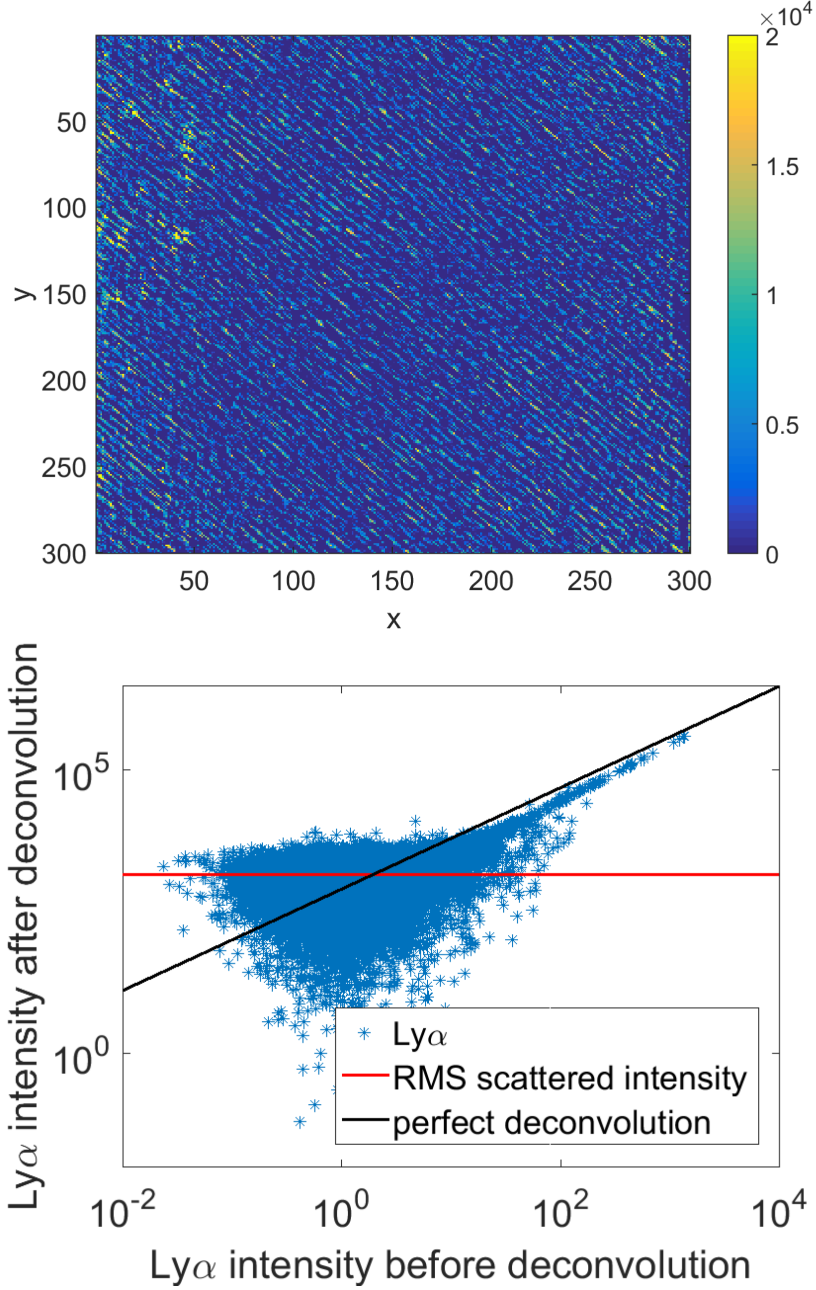

Figure 6.12: Fourier deconvolution of simulated Lyα sources. **Top**: The deconvolved data cube using Fourier method is shown as a summed image in the z-direction. Brightest sources are overexposed to reveal the underlying structure. **Bottom**: The scatter plot of Lyα intensity after deconvolution vs. Lyα intensity before deconvolution for all sources. The horizontal red line indicates the RMS value of scattered intensity in the cube. The black reference line corresponds to intensities after a perfect deconvolution.

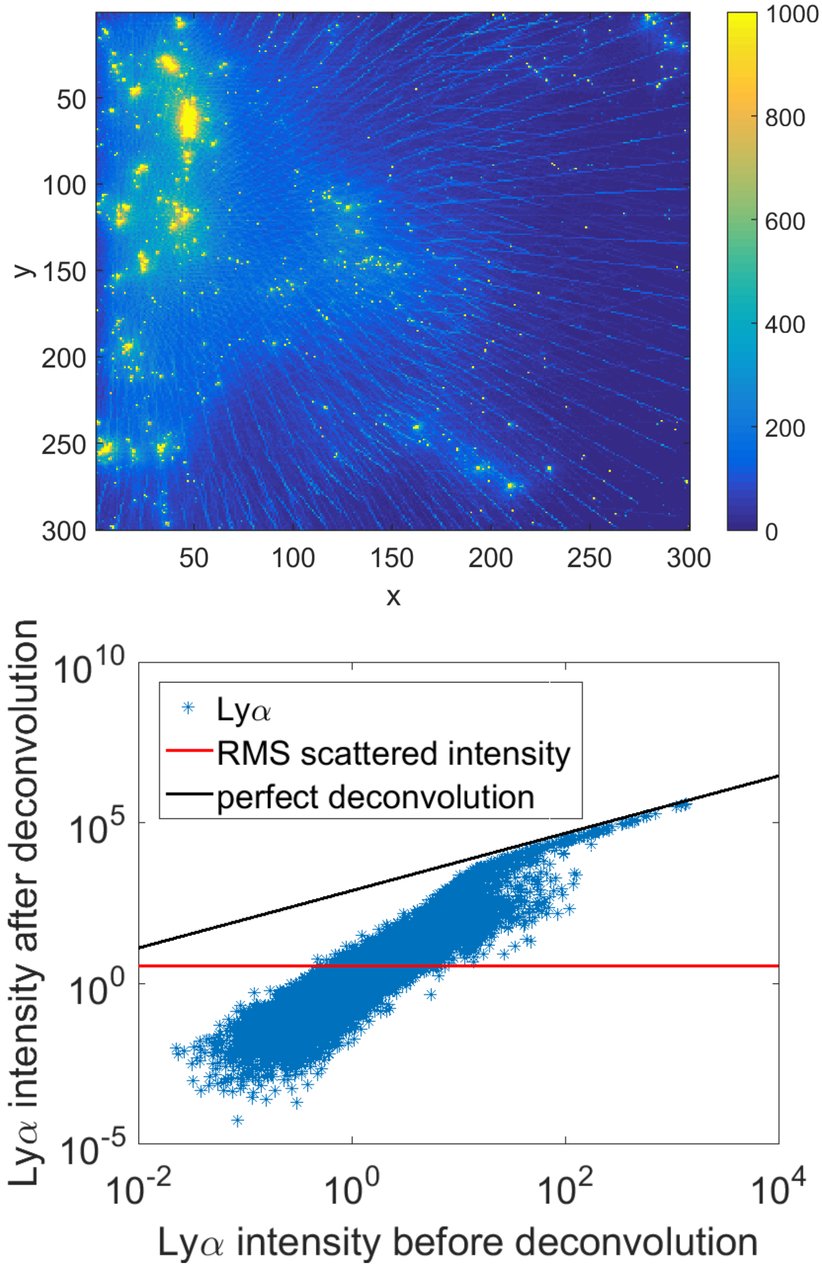

Figure 6.13: Richardson-Lucy deconvolution of simulated Lyα sources. **Top**: The deconvolved data cube using RL method is shown as a summed image in the z-direction. **Bottom**: The scatter plot of Lyα intensity after deconvolution vs. Lyα intensity before deconvolution for all sources. The horizontal red line indicates the RMS value of scattered intensity in the cube. The black reference line corresponds to intensities after a perfect deconvolution.

3. Add simulated back-projected stars using M-star spectrum template

4. Conduct deconvolution using both techniques on simulated Lyα sources.

5. Calibration is done after deconvolution.

The deconvolution results of Lyα sources and M-star with different magnitude are shown in Fig.6.15. The star is masked by setting the corresponding voxels to zero after the deconvolution. Since the scattered intensity in the cube comes from both Lyα sources and M-star, the RMS value of scattered intensity rises as I increase the magnitude of M-star. We can observe from Fig.6.15 that fraction tends to converge as the star becomes brighter than a certain magnitude. This fraction does not converge to 1 under Fourier method, because scattered intensity is randomly distributed around RMS and a certain portion of sources are brighter than RMS. For RL method, the fraction converges to 1 because Lyα sources are removed as scattered intensity as the star becomes brighter. It can also be noticed that the plateau due to a dim star is formed by the RMS scattered intensity from Lyα sources. Even though a lot of Lyα sources are dimmer than RMS value of scattered intensity, a few bright sources accounting for most of the intensity are still brighter than RMS when the star is dimmer than 15 magnitude.

The scattered intensity plots for Lyα emitters are displayed in Fig.6.16 and Fig.6.17. For Fourier method, as the star increases its brightness, we can notice that the RMS scattered intensity is also increasing and the few brightest sources cease to form a linear relation in the plot. This is because the intensity of these brightest sources is affected by the scattered intensity from the star. When the star magnitude is less than 15, RMS scattered intensity is the same level as the brightest sources, and hence none of the sources can be discovered. For RL method, the linear shape of the plot starts to deform as the star increases its brightness. Even the brightest stars vanish when the star magnitude is less than 15, which again indicates the unsuccessful reconstruction of this technique.

The results of simulated Lyα sources and stars show that Lyα sources can not be properly reconstructed if there is one star in the field which is brighter than magnitude 15.

6.6 Masking Stars in Grism-dispersed Images

The above analysis indicates that bright sources in the fields are major problems for the deconvolution. Although bright stars are masked after deconvolution, their scattered intensity can not be perfectly removed and severely reduce the signal-to-noise of Lyα sources. One possible solution is to remove bright stars before the deconvolution.

In grism-dispersed images, light from sources is dispersed into a spectrum by a grism. We can identify which spectra come from bright stars by locating the stars in

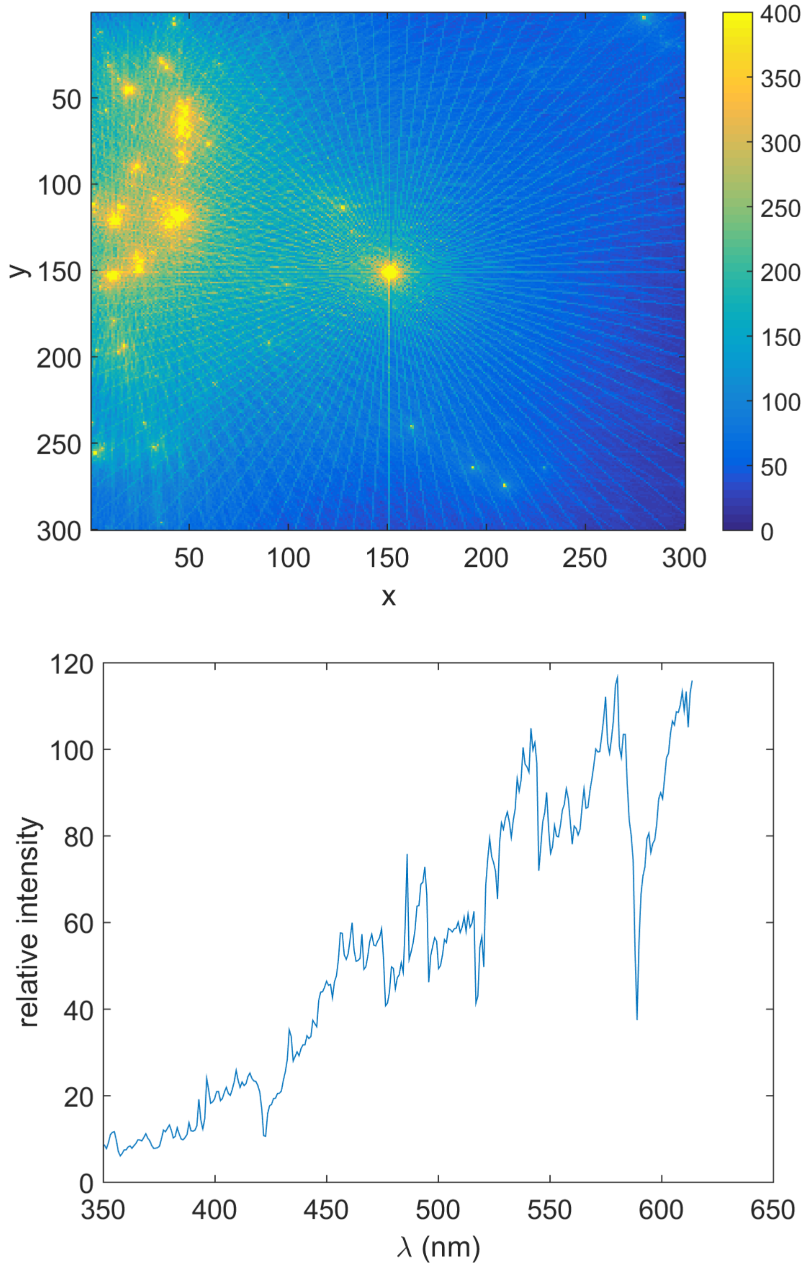

Figure 6.14: **Top**: The simulated back-projected data cube with Lyα sources and a single M-star at the center of the image is summed up in the z-direction. **Bottom**: spectrum of M-star

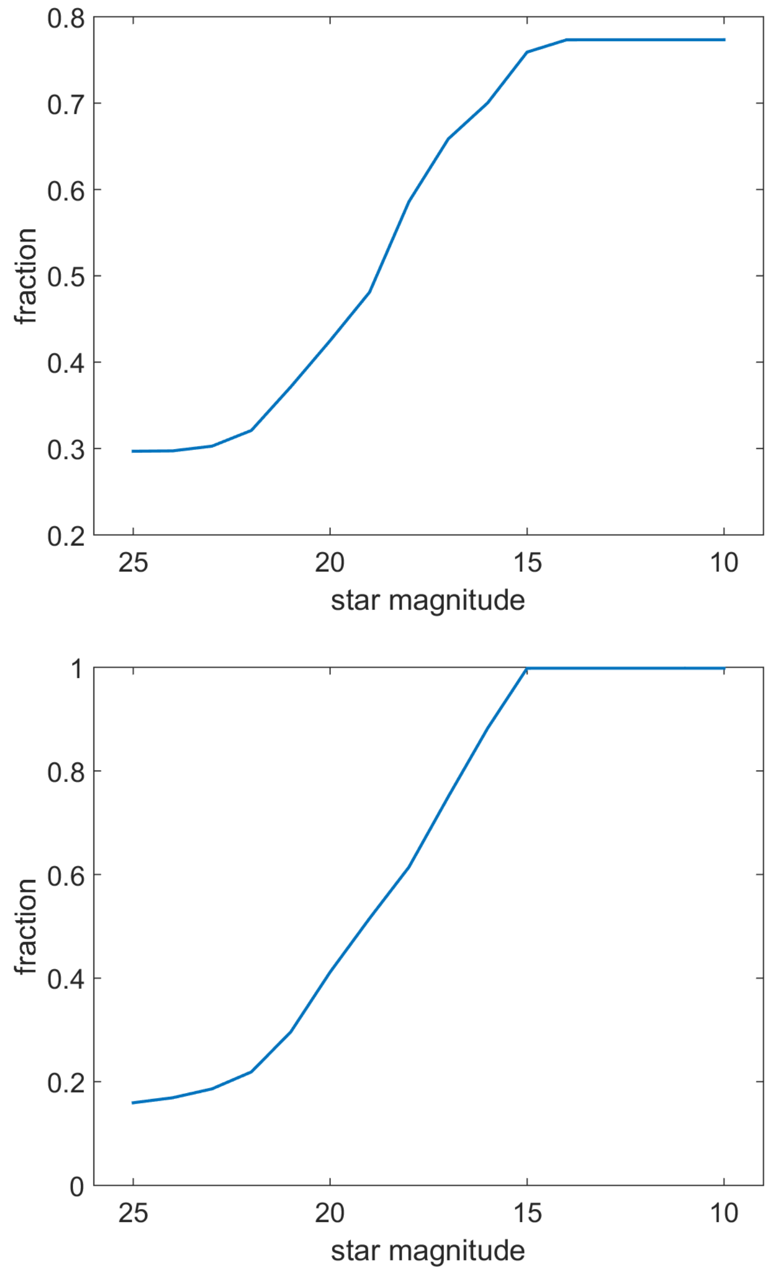

Figure 6.15: The fraction of total Lyα intensity that comes from Lyα emitters who are **dimmer** than the RMS value of scattered intensity, at different magnitudes of the simulated M-star. **Top**: Fourier method. **Bottom**: RL method

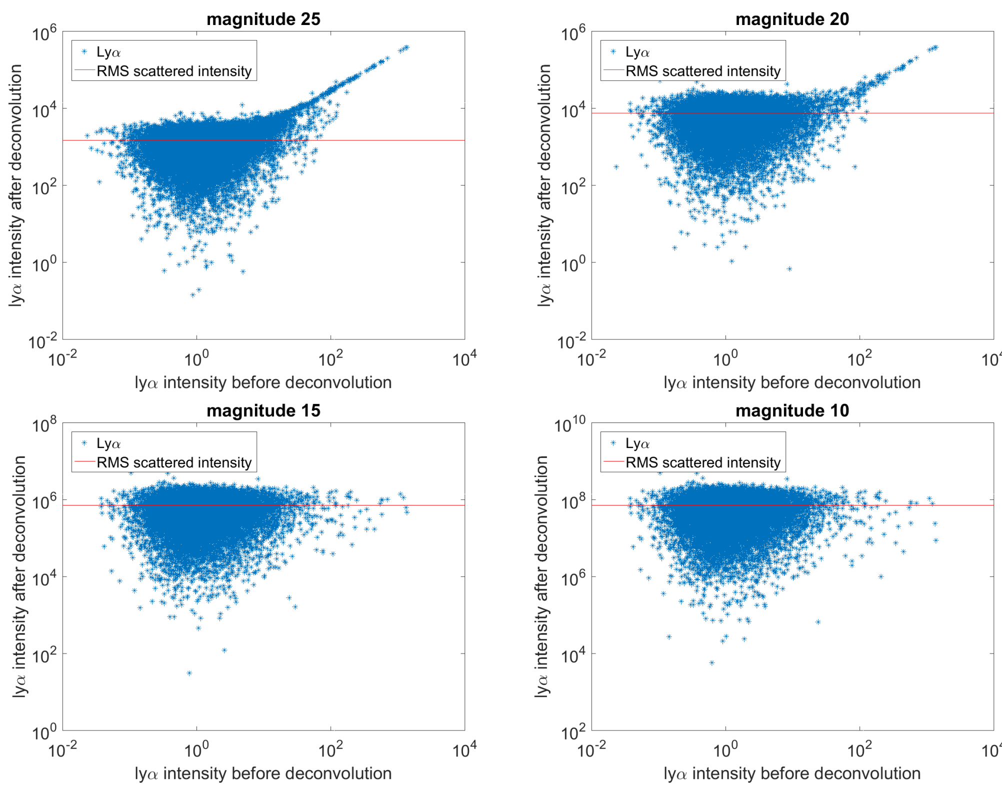

Figure 6.16: The scatter plot of Lyα intensity after deconvolution vs. Lyα intensity before deconvolution for all Lyα sources, using **Fourier method**. The simulated star is set to magnitude 25, 20, 15 and 10 respectively. The clouds of points denote the failure of deconvolution for faint sources.

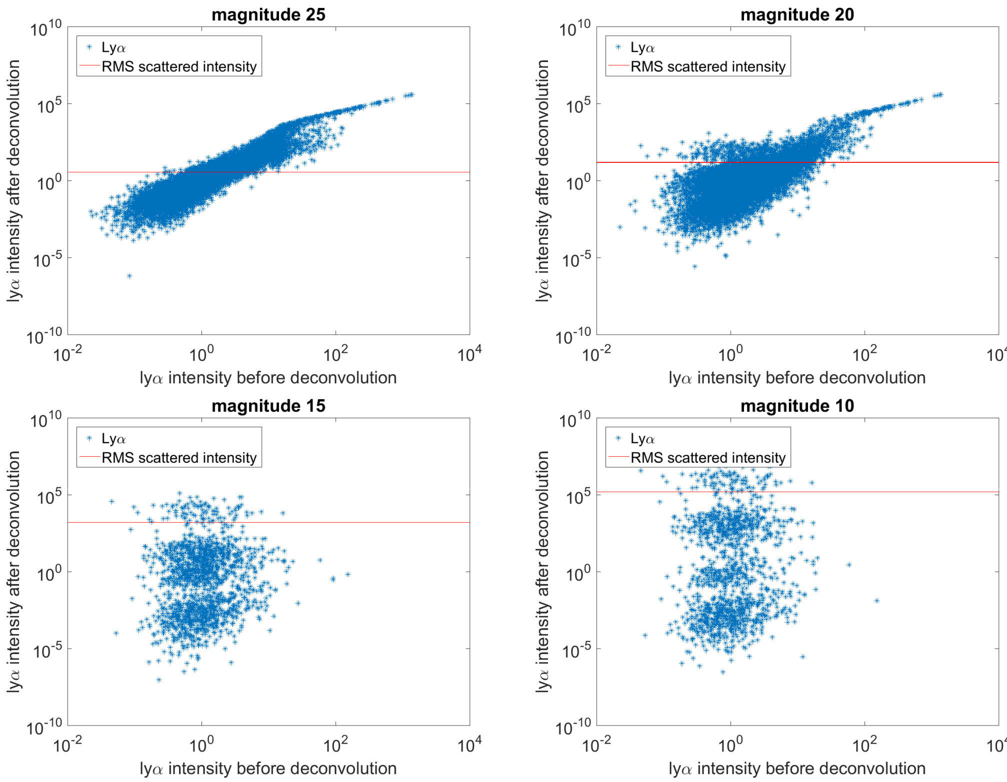

Figure 6.17: The scatter plot of Lyα intensity after deconvolution vs. Lyα intensity before deconvolution for all sources, using **RL method**. The simulated star is set to magnitude 25, 20, 15 and 10 respectively. The clouds of points denote the failure of deconvolution for faint sources.

our field. The next step is to remove these spectra from stars by completely masking the pixels they fall onto. We hope to reconstruct the hyperspectral data cube using these grism-dispersed images with missing pixels, which is possible if there are few pixels missing. To summarize the idea, here are the steps of masking stars in grism-dispersed images:

1. Locate bright stars and identify their spectra in grism-dispersed images.

2. Mask the spectra of bright stars by setting their pixel values to zero.

3. Conduct back-projection and deconvolution on these masked grism-dispersed images.

Fig.6.18 shows the luminosity function and spatial distribution of stars from a randomly picked SDSS field that has the same size as our 300*300*300 cube in x, y dimension. There are 9169 stars in this field, which are too many to be masked entirely. Because all pixels will be missing if we mask every star in the field. Therefore it is possible to mask only a few brightest stars. Calculations must be done to estimate the number of stars that can be masked before we lose half of the pixels.

Based on the discussion in Section 5.2 and our simulation, one pixel in the grism-dispersed images corresponds to $0.44nm$. The bandwidth of U band is usually $66nm$, so the length of the spectrum of a star is about $L_{spectrum} \approx 150$ pixels on grism-dispersed images. In fact, the spectrum could fall onto more than 150 pixels if it is not aligned with x or y direction on the images. But it is reasonable to use 150 pixels as a lower limit.

Fig.6.19 shows the relation between the fraction of pixels being masked and the magnitude of brightest star remained in the image. The plot assumes no overlaps among spectra of different stars. The fraction grows linearly after 15 magnitude, which makes it hard to further lower the intensity in the images. We can only get down to 17.5 magnitude when we mask 50% of the pixels. But stars of 18 magnitude would fail the deconvolution according to previous analysis.

Overall, masking the spectra of bright stars in grism-dispersed images is not improving the reconstruction of Lyα sources. We are not able to significantly lower the scattered intensity in the reconstructed cube because the number of masked spectra is limited. Meanwhile, we are also facing problems with missing pixels.

6.7 Masking Stars at the Image Plane

Instead of masking half of the pixels on grism-dispersed images, we can also mask the stars on the focal plane. This is the main masking scheme I discussed in Chapter 3 and its relevant design is discussed in Chapter 4.

The masking can be done in following steps:

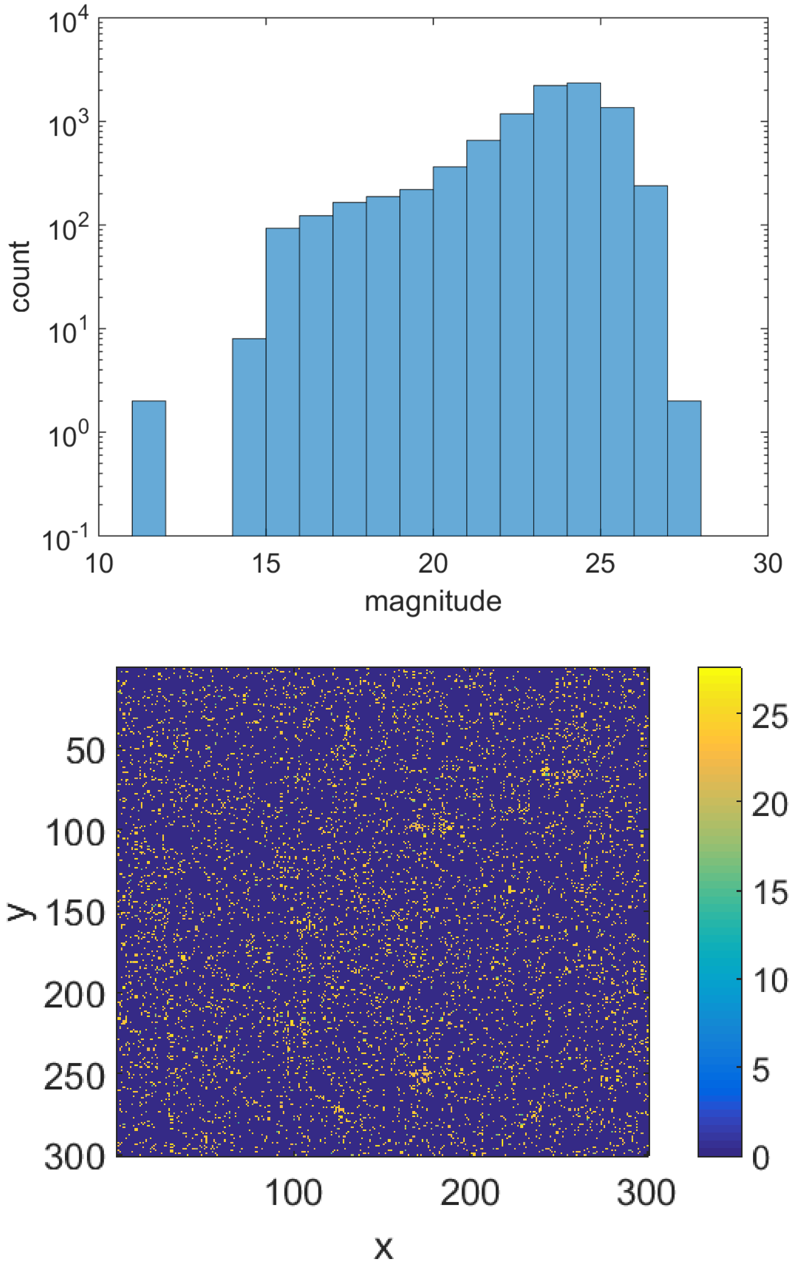

Figure 6.18: Luminosity function and spatial distribution of stars from a randomly picked SDSS field. **Top**: Luminosity function. **Bottom**: Spatial distribution, where the value corresponds to the magnitude of star.

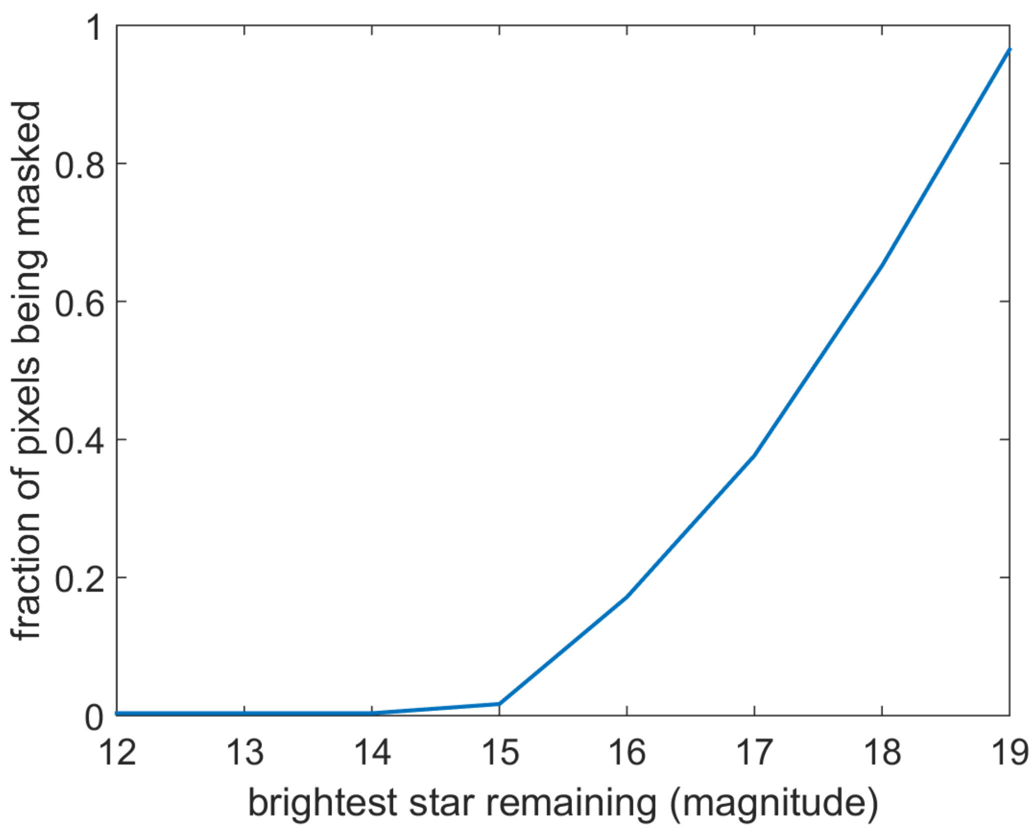

Figure 6.19: The fraction of pixels that are masked against the magnitude of the remaining brightest star that is not masked.

1. Locate bright stars in the field of view either by taking a picture or using SDSS catalog.

2. Make a mask at the image plane to block the light from the locations of these stars.

3. Take the standard set of grism-dispersed images, which now get rid of star spectra.

4. Conduct back-projection and deconvolution on these grism-dispersed images.

This masking idea can be tested with the randomly picked SDSS field and simulated Lyα sources mentioned in the preceding sections. I created a back-projected cube for these stars and Lyα sources using the double-cone PSF. Masking stars in the simulation is carried out simply by creating a new back-projected cube without the masked stars. I masked stars in the field using a cutoff magnitude, which means only stars that are brighter than the cutoff magnitude are masked. Cutoff magnitude is a threshold for masking stars and affects the tradeoff between the number of pixels being masked and scattered intensity from stars.

The results are shown in Fig.6.20, which describes the fraction of the total intensity contained in those Lyα sources that are brighter than RMS value of scattered intensity, after I masked stars at each cutoff magnitude. It is calculated by first locating Lyα sources that are brighter than RMS value of scattered intensity after deconvolution, and then determining their percentage of total original intensity. I use this fraction of intensity to roughly measure how much Lyα intensity can be identified given the presence of stars. The upward trend in both plots indicates the scattered intensity due to stars is effectively reduced as we continue masking stars. If all the stars are masked, Fourier method can recover 70% Lyα intensity and RL method can recover 85% Lyα intensity. The slope is greatest at 24 and 25 magnitude because there is the most number of stars around these magnitudes. The curve is not smooth and monotonic for RL method, mainly due to the overlap between stars and Lyα sources. As can be observed in Fig.6.21, a great number of stars at 24-26 happen to appear along the same line of sight as Lyα sources. When stars and Lyα emitters appear in the same pixels, it is hard to distinguish them and their intensities are tied together after deconvolution. These Lyα sources are either measured as bright stars, or ignored due to masking stars, resulting in the bumpy curve for RL method.

Given the good performance of the simulation results, we also want to make sure the missing information due to masking is limited to a reasonable range. In Fig.6.22, the fraction of pixels not being masked is plotted against the cutoff star magnitude. It is calculated through the SDSS data set and the 300*300 field of view consistent with our preceding simulations. Only 10% of pixels are lost even when I masked every star in the field.

As we look at the results from Fig.6.20 and Fig.6.22 together, it is obvious that masking stars can recover more than 50% of intensity only after reaching 24 magni-

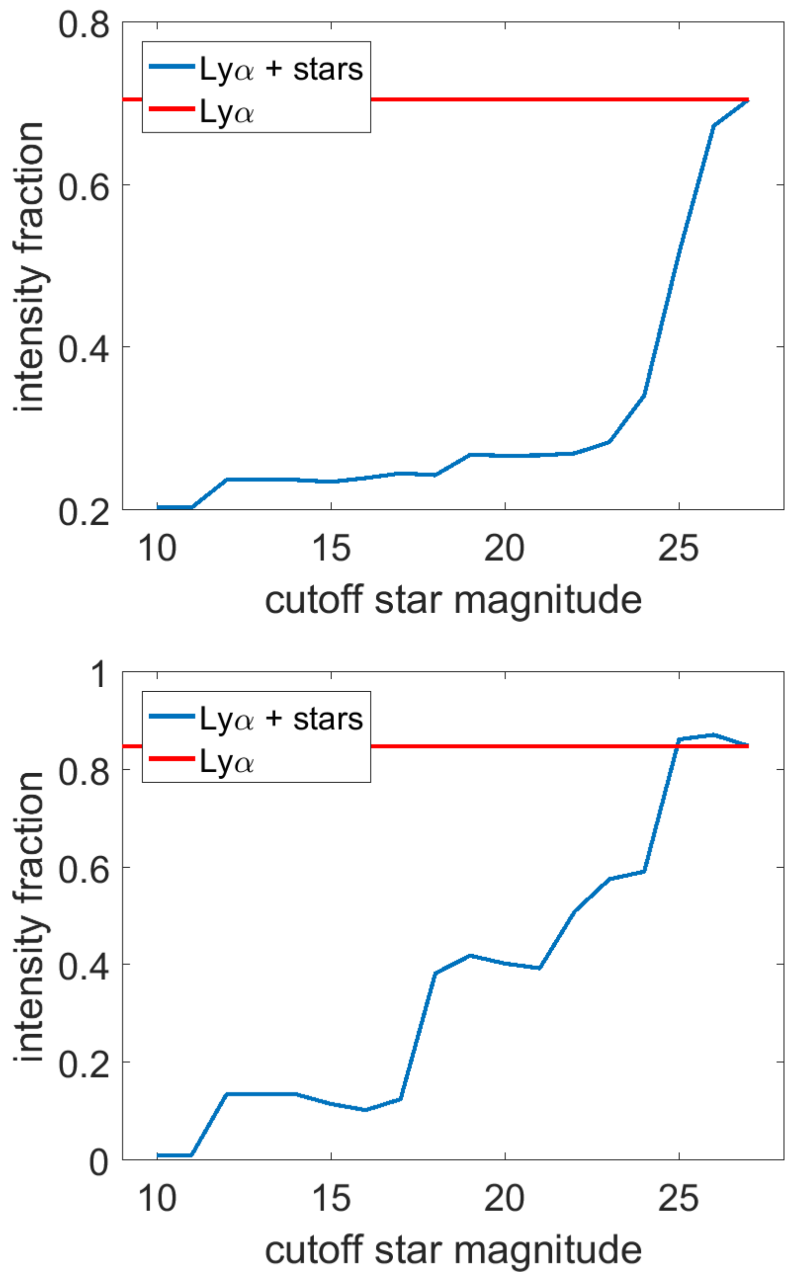

Figure 6.20: The fraction of the total Lyα intensity contained in those Lyα sources which are **brighter** than RMS value of scattered intensity, at various cutoff star magnitudes. The blue line is the simulated data set that consists of both Lyα sources and stars. Red line, as a comparison, shows the fraction of intensity when there are only Lyα sources in the data set. **Top**: Fourier method. **Bottom**: RL method.

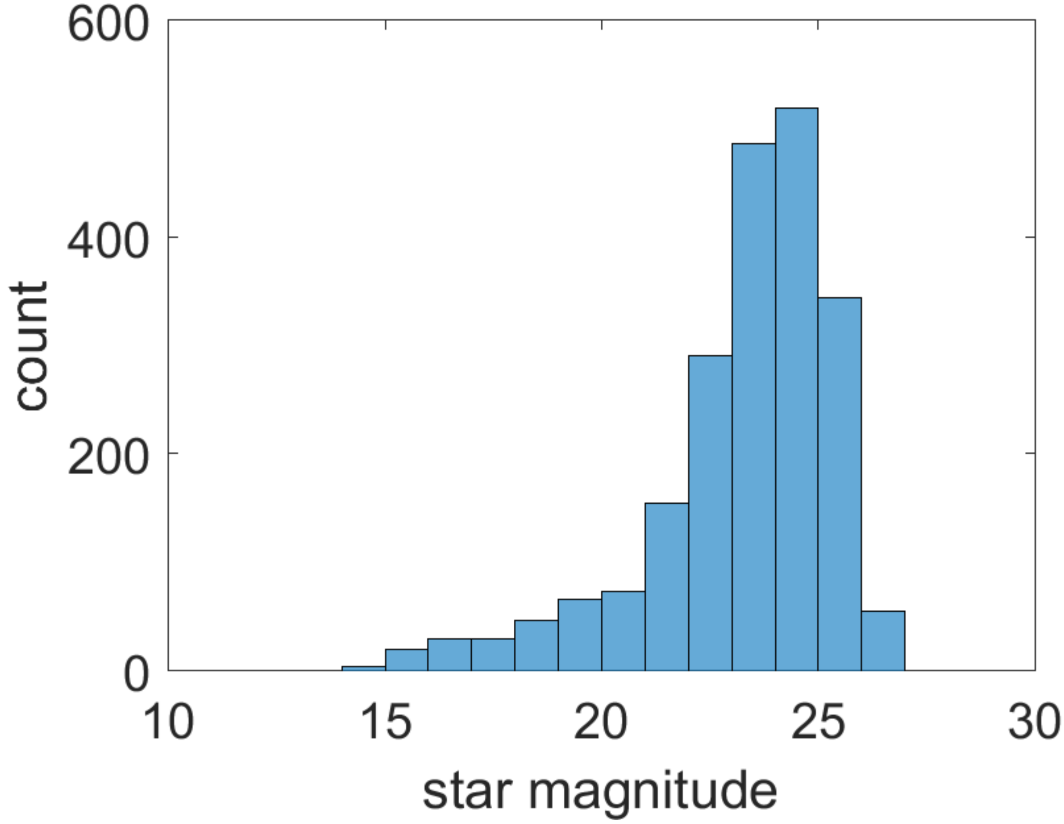

Figure 6.21: Histogram of SDSS stars that overlap with Lyα sources in the synthetic cube.

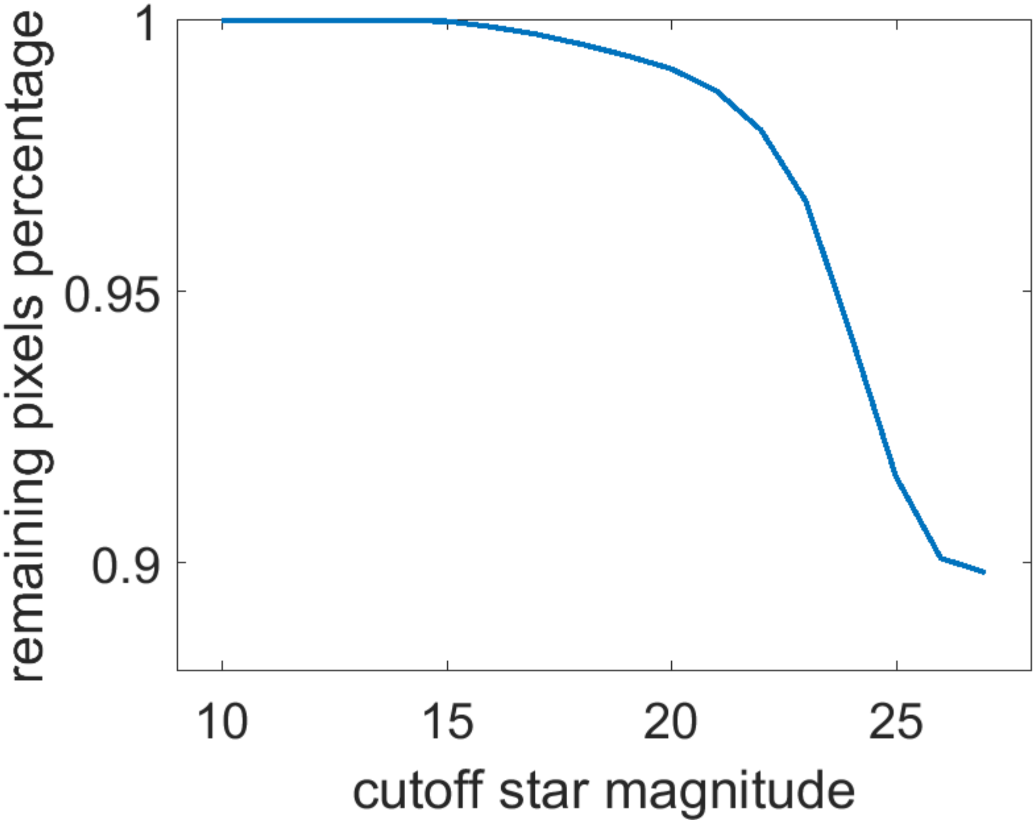

Figure 6.22: Percentage of pixels remaining in the field of view for each cutoff star magnitude

tude. And we can improve the Lyα recovery from 20% of intensity to 80% of intensity, by sacrificing only 10% of pixel information. Thus masking stars at the focal plane is necessary and effective for Lyα intensity mapping.

6.8 Conclusion

In this chapter, I discussed two deconvolution techniques and their performance under several scenarios. The results indicate that deconvolution is strongly affected by the bright sources in the field, which is a major problem due to stars observed in SDSS. This dynamic range is 1000 for both methods. Fourier technique suffers from location-dependent PSF and results in a great amount of scattered intensity in the reconstructed cube. Richardson-Lucy technique is better at reducing the scattered intensity and putting the intensity at the correct source location. A more fundamental problem with both techniques is that back-projection brings $L_z - 1$ times more intensity into the data cube than the actually observed intensity, where L_z is the length of the cube in the z-direction. In summary, both techniques cannot successfully reconstruct all Lyα sources given the stars present in the SDSS. Masking bright stars is required to reconstruct the Lyα signal. According to my simulation, 50% of the total Lyα intensity can be recovered using the RL method if we mask all stars brighter than magnitude 20 from the SDSS catalog.

Chapter 7

Experiments

I ran three different experiments to test my GSTI using real sources. First, I conducted experiments with my telescope on a HeNe laser ($\lambda = 632.8nm$). Since lasers are monochromatic light sources, they can demonstrate double cone structure in the back-projected cube. Second, I tested the telescope with 5 LEDs in the lab for multiple sources conditions. Third, I pointed my telescope to a bright star in the sky to obtain a real star spectrum. Experiment steps are outlined below:

1. Take 100 images of the source as the grism rotates, and each angle between each grism orientation is $\alpha = 3.6°$.

2. Pre-process these 100 grism-dispersed images and feed them to the basic back projection algorithm.

3. Conduct deconvolution using both Fourier and RL techniques on the back-projected data cube.

4. Calibration is done after deconvolution.

5. Analyze the spectrum and compare with the spectrum from other sources.

7.1 HeNe Laser

The HeNe laser is pointed on a white cardboard on which the laser spot is taken as the source. The angular step between each projection is $\alpha = 3.6°$. Our back projection angle is chosen to be $\beta = 45°$. To test the quality of optics, I ran this experiment 4 times with the laser spot at 4 different locations on the sensor plane. And I took 100 images at each of these locations, with 1/15 second exposure time and 100 ISO. The 4 locations are shown in Fig.7.1 and their back-projected data cubes are shown in Fig.7.2 respectively. When preprocessing the images, I also bin 4×4 finest pixels into one pixel because the size of the laser spot is about 10 pixels in diameter. I crop

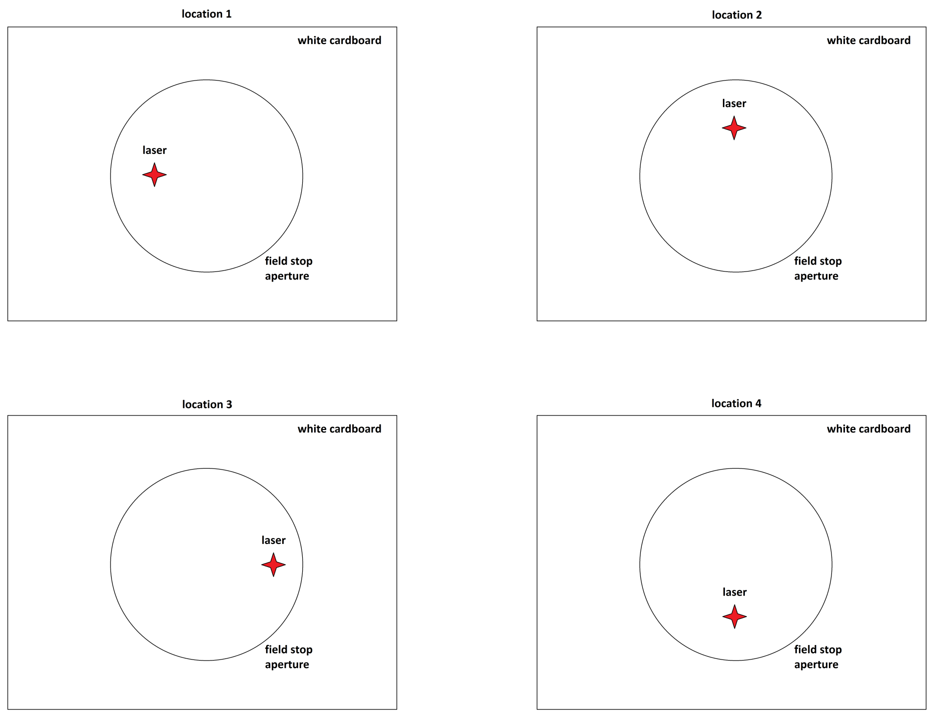

Figure 7.1: The 4 locations on sensor plane used in the experiments for HeNe laser. The laser spot is on a white cardboard. They are left, up, right and down relative to the center.

the images to use only the regions that have laser spots, which uses less memory of the computer and speeds up the computation.

Before reconstruction, I would like to show the quality of my grism. Two sets of the laser spots are compared in Fig.7.3 and Fig.7.4. They show eight laser spots respectively with different grism orientations for HeNe laser at location 1 and location 4. I put the brightest pixel at the center of each image. Obviously, the brightest part is not at the center of the laser spot and the profile is not Gaussian. In addition, the spot shape changed inconsistently as the grism rotated about the axis, not along the dispersion direction nor at a constant angle to that direction. The intensity in each pixel of the spots is also inconsistent at different grism orientations. The plots show the limited quality of the optics used on my instrument, which brings errors to the final reconstruction results.

The poor quality of optics results in slightly different back-projected data cubes in Fig.7.2. The back projection algorithm creates a double cone structure and the vertex of this double cone is at the wavelength of the laser. Despite the X shape for all 4 location, they have different intensities and shapes around the center of the vertex. This inconsistency can be attributed to the differences between the 4 sets of

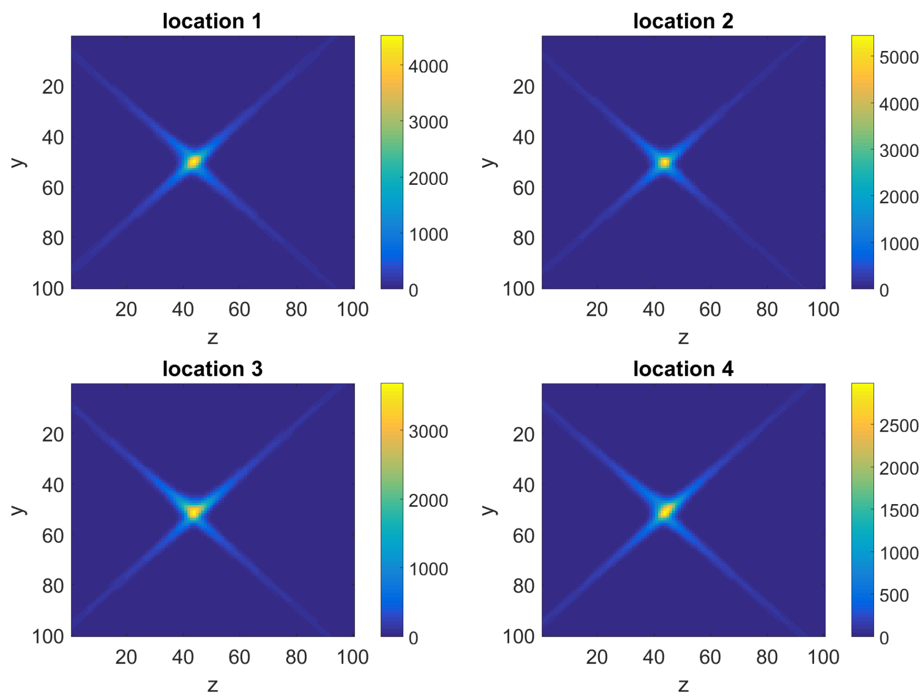

Figure 7.2: The double cone structure of HeNe laser at 4 locations shown as a slice along the $\lambda(z)$ direction at the source location x. The X shape is the cross section of the double-conical surface. The vertex of the double cone is the measured spectrum of the laser.

grism-dispersed images at 4 locations. The laser spot shapes and intensities are both varying with different locations and different grism orientations. And intensities from the strangely shaped laser spots do not intersect exactly at the pixels they come from during the back projection. So finally the intensity profile of the double cone vertex is different for the 4 locations.

The laser spectra before deconvolution are shown in Fig.7.5. Since the laser spot is larger than 1 pixel spatially, I choose the spectrum across the brightest pixel as the laser spectrum. These intermediate spectra display the results of basic back projection. The peak is located at the right wavelength and curve is smooth. This is already a good laser spectrum despite its large FWHM. Aside from spectrum, the double cone structure also exists in the back-projected data cube and needs to be corrected by the deconvolution.

The laser spectra after Fourier deconvolution are shown in Fig.7.6. The peak remains the same shape without narrowing the FWHM. It becomes less smooth but stays at the correct location. What becomes obvious is the scattered intensity and artifacts due to Fourier transform. There are also negative intensities in some of the voxels, because the deconvolution takes away more intensities from these voxels than they started with. The result is that intensities are scattered all over the reconstructed data cube. As I mentioned in Chapter 6, there are two reasons for this much scattering. One is the truncation effect of the double cones, which indicates there is a mismatch between the PSF and the actual double cone structures in the cube. The other reason is that poor quality of optics creates a back-projected data cube that is not described well by the model.

The laser spectra after RL deconvolution are shown in Fig.7.7. We can notice that the peak FWHM is smaller compared to results before deconvolution. Thus RL deconvolution improves the spectral resolution for the laser. And the scattered intensity can not be seen on the plots because it is reduced by the algorithm.

As a conclusion, HeNe laser serves as a real monochromatic point source in the hyperspectral data cube, and I use it as the basic scenario for my GSTI. Although the laser spots do not have Gaussian profiles and are not consistent at different grism orientations, the reconstruction results are still consistent with theory as well as simulation. Back projection creates double cones from the grism-dispersed images and forms a decent spectrum at the vertex. RL method outperforms Fourier deconvolution in terms of peak FWHM and scattered intensity.

7.2 LEDs

I then run the experiments on 5 LEDs in the lab, using the same target as briefly described in Chapter 4. The 5 LEDs with different colors and brightness are fixed on a white cardboard in the Lab. Their positions and colors are shown in Fig.7.8. I also mark the LEDs from 1 to 5 which are referred to later. In this experiment, I took a set of 120 images at a grism rotation step size $\alpha = 3°$. The exposure time is

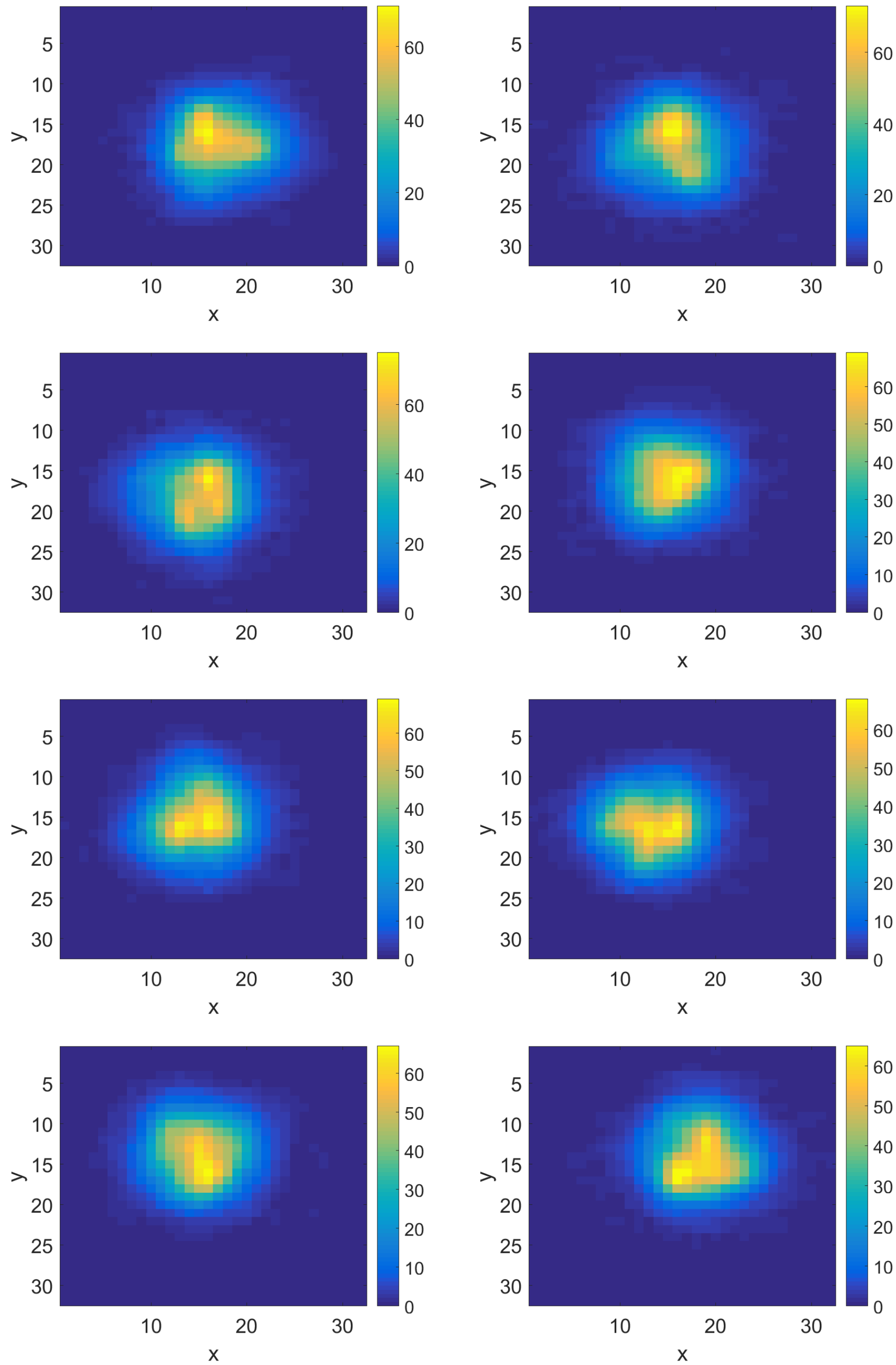

Figure 7.3: Zoomed-in images of raw laser spot at different grism orientations of location 1. The brightest pixel is centered for each image. Spot shapes are irregular for different orientations rather than circular or elliptical.

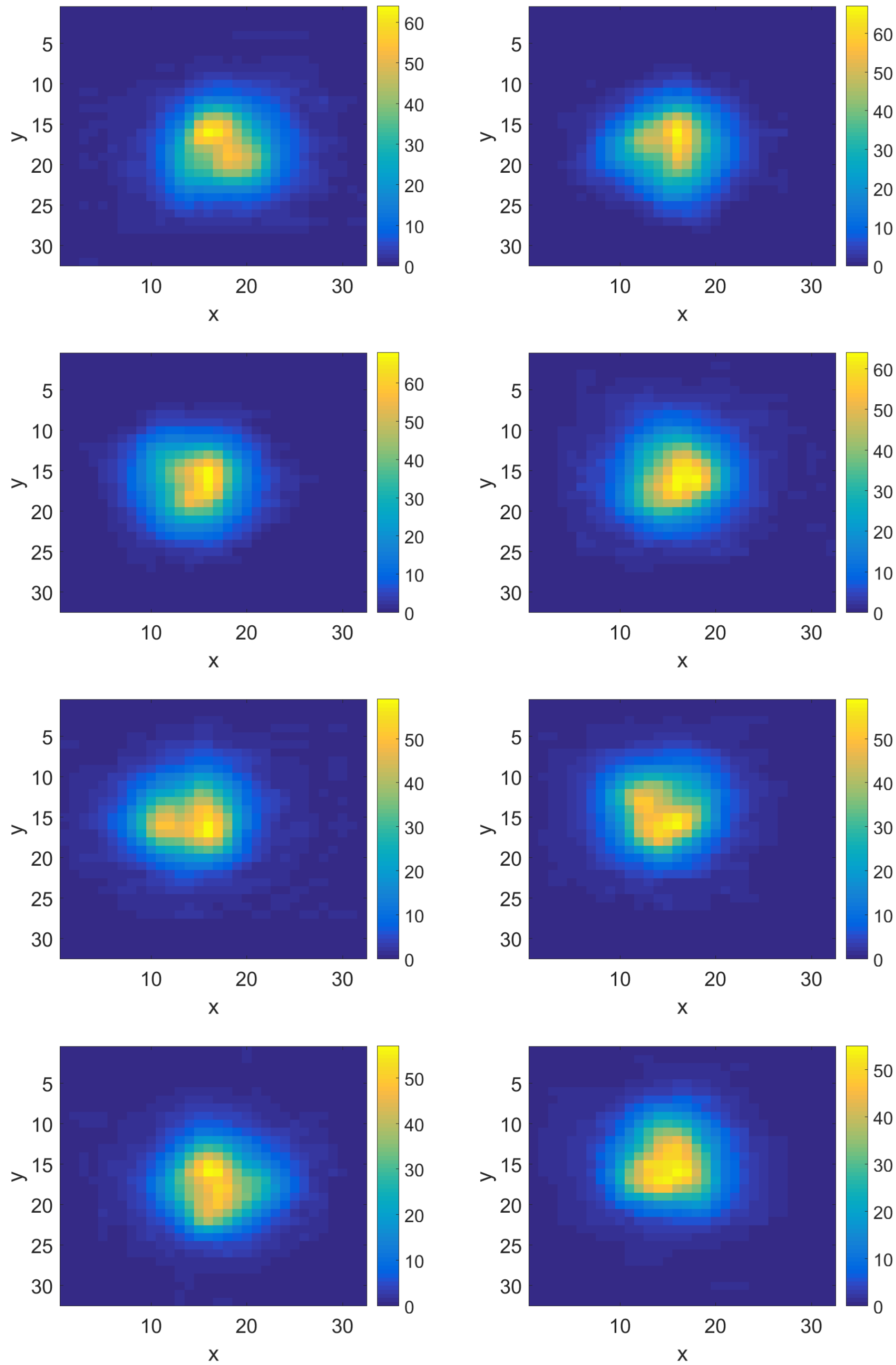

Figure 7.4: Zoomed-in images of raw laser spot at different grism orientations of location 4. The brightest pixel is centered for each image. Spot shapes are irregular for different orientations rather than circular or elliptical.

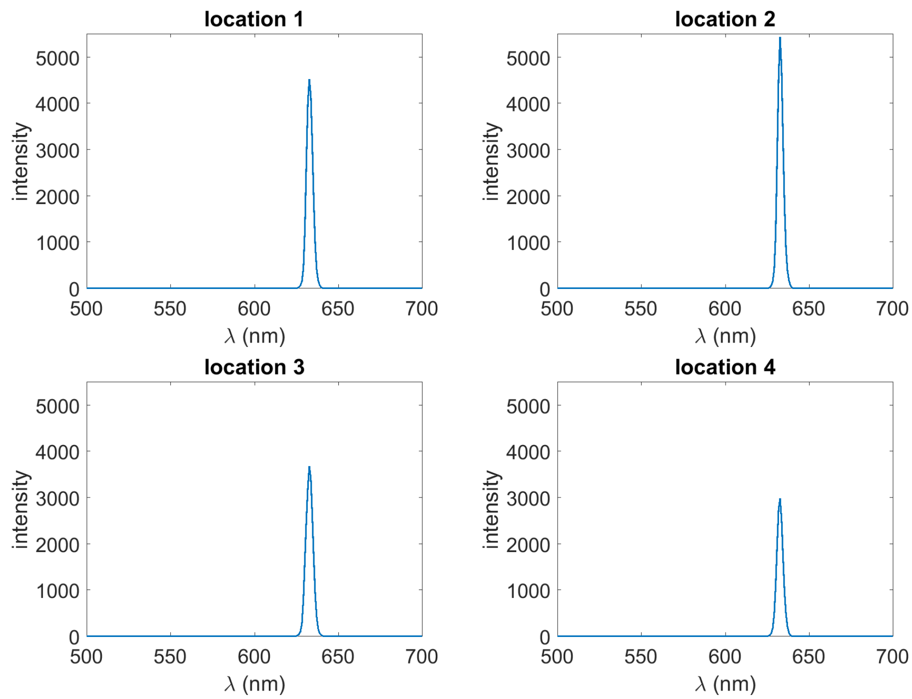

Figure 7.5: Spectrum of the HeNe laser for the 4 locations after basic back projection, but before deconvolution.

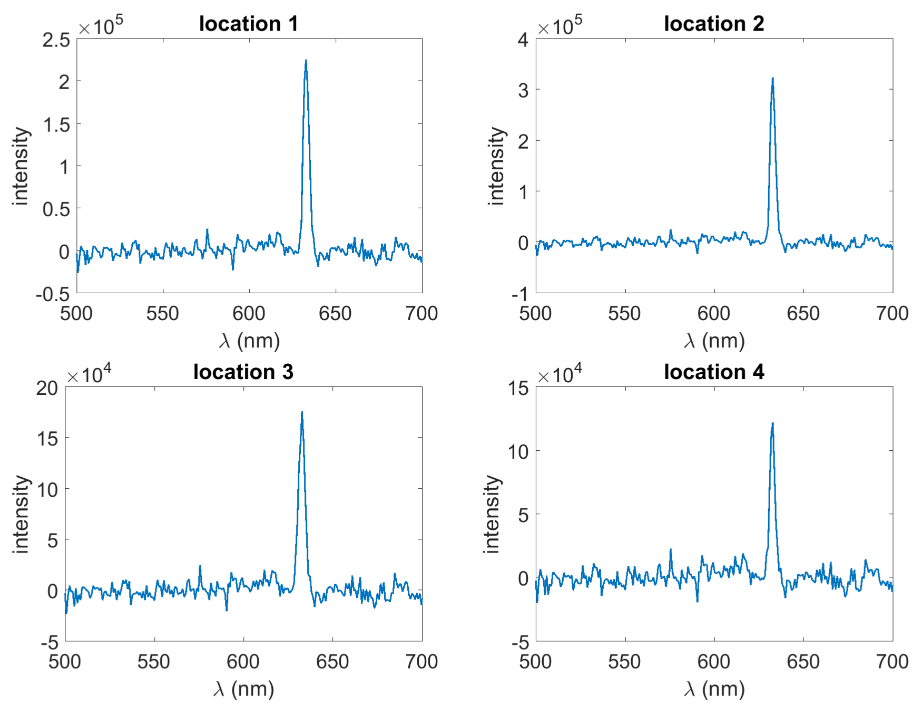

Figure 7.6: Spectrum of the HeNe for the 4 locations after Fourier deconvolution

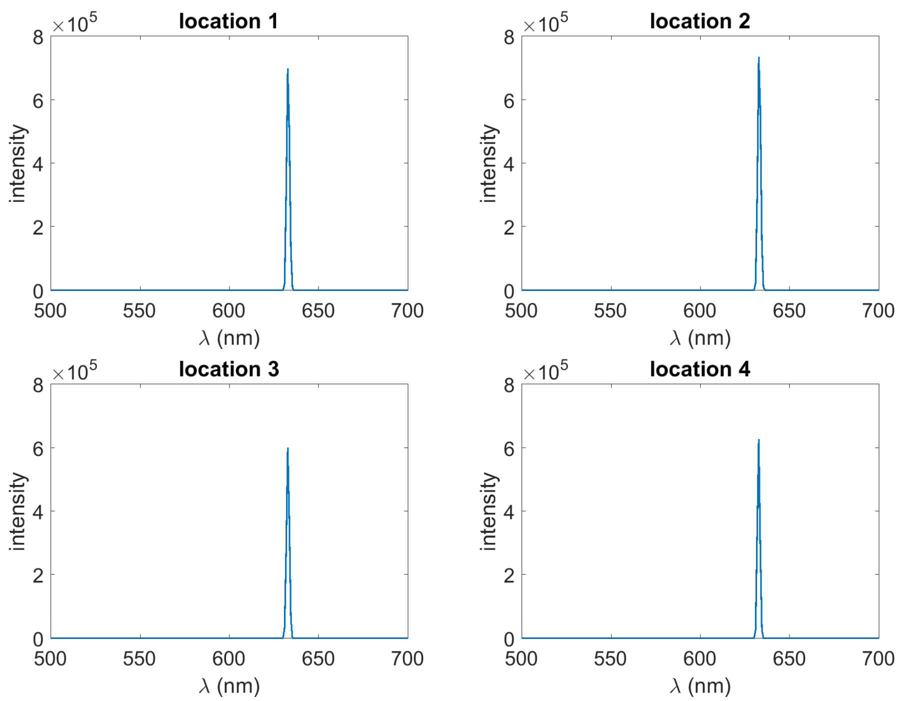

Figure 7.7: Spectrum of the HeNe for the 4 locations after Richardson-Lucy deconvolution

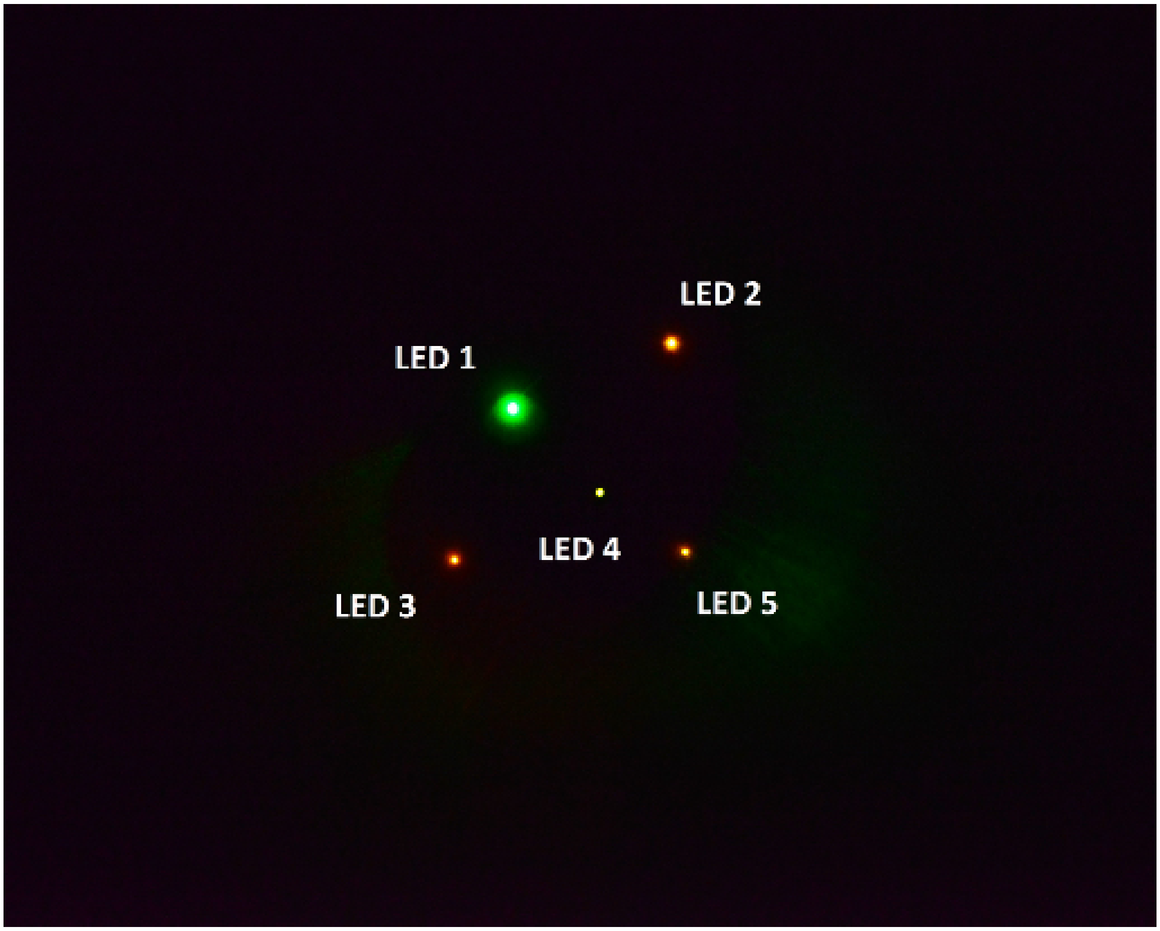

Figure 7.8: Marked LED positions used in the experiment. The image is taken with the same telescope but without the grism.

1/200 second, and ISO speed is 6400. I show in Fig.7.9 eight grism-dispersed images obtained by the GSTI from the LED experiment. These eight images are separated by a grism rotation angle 45°. The spectra from different LEDs may overlap as the grism rotates. 2nd order and 0th order diffraction also appear on the image at some grism orientations.

For the reconstruction process, I choose the back projection angle $\beta = 45°$. I also bin 16×16 finest pixels together due to limited computational resources. Binning pixels reduces spectral resolution because each voxel in the cube corresponds to a larger wavelength range than the laser experiment. During the preprocessing, I mask the 2nd order and 0th order diffractions and use only the center regions of the images that contain the spectra.

The 5 LED spectra resulted from basic back projection are shown in Fig.7.10. The LED spectra are all wider than the laser spectra in the above section. It indicates that LEDs are not monochromatic sources, which is consistent with our observation

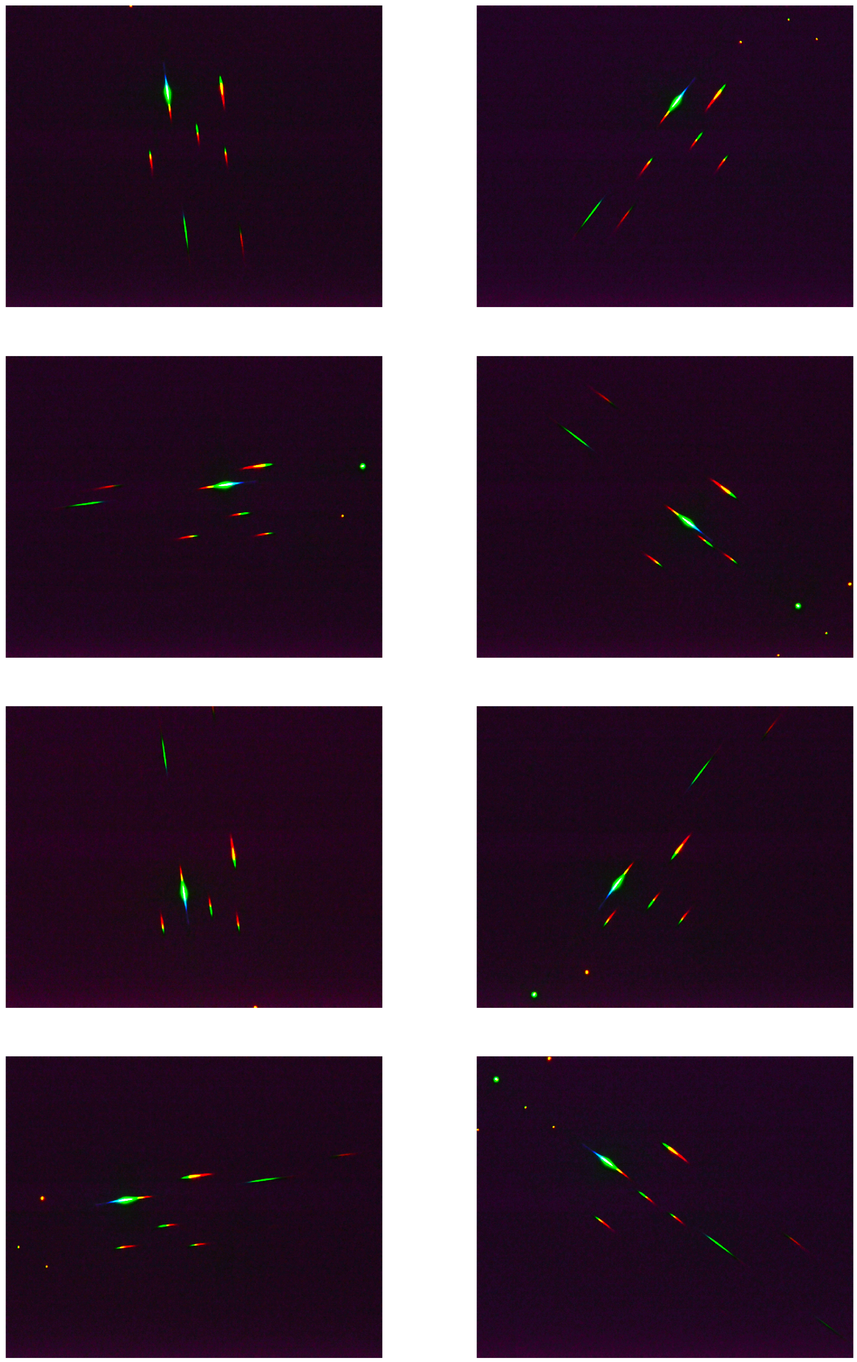

Figure 7.9: Raw grism-dispersed images from LED experiments. From left to right, from top to bottom, grism rotates 45° for each image.

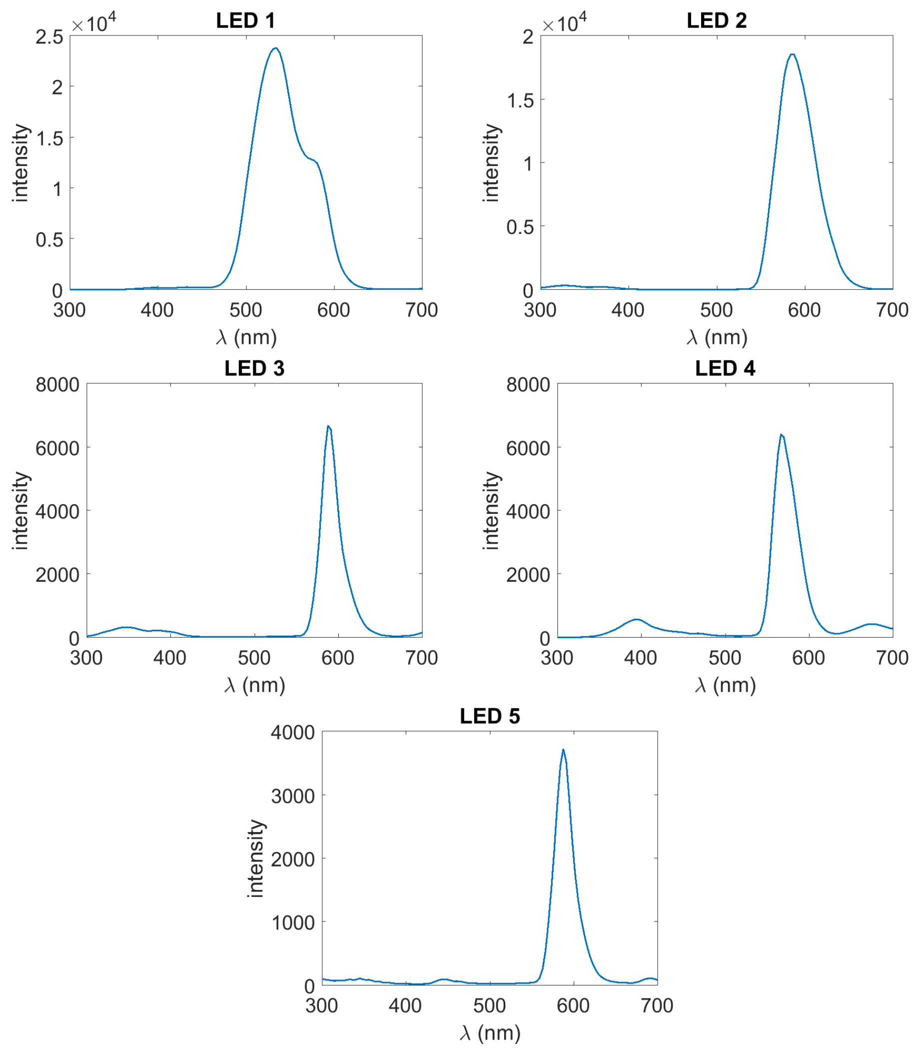

Figure 7.10: Spectra of 5 LEDs after basic back projection, but before deconvolution.

from the spectra on grism-dispersed images. The relative intensity and the width of the spectrum also match the grism-dispersed images. LED 1 has the brightest and longest spectrum, while LED 5 is the faintest. Besides spectral peaks, we can also notice some smaller bumps, especially in those fainter LEDs. These are the artifacts caused by double cone structures. These bumpy artifacts become more severe than the plots shown if there are more sources or brighter sources. So deconvolution must be carried out even if the spectra are good after back projection.

LED spectra after Fourier deconvolution are shown in Fig.7.11. The spectra shapes have not changed much. Similar to the results of the laser, there are negative voxel values and scattered intensity due to Fourier transform. There are fewer high-frequency components in the spectra compared to laser, mainly because LED experiments have more grism-dispersed images. More grism-dispersed images signify there is more in-

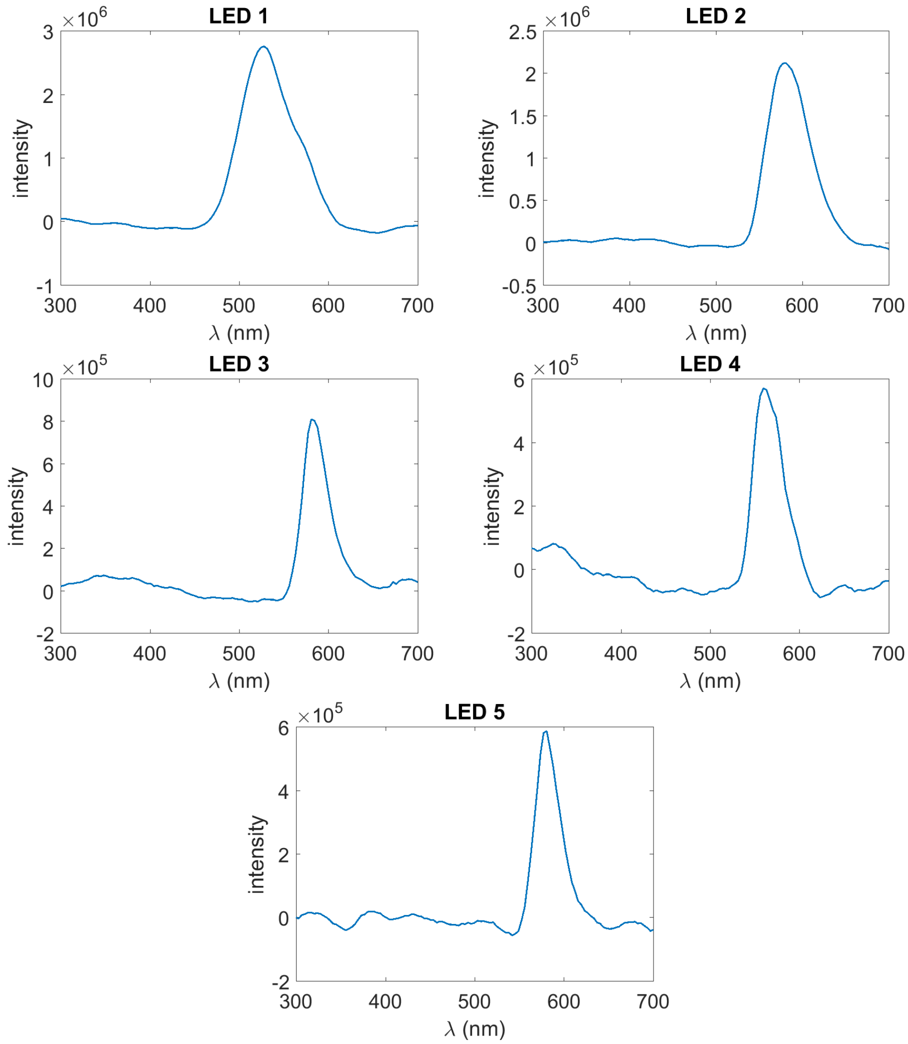

Figure 7.11: Spectra of 5 LEDs after fourier deconvolution.

formation in Fourier space, as explained by the Fourier slice theorem in Chapter 5. And high-frequency noise is diminished during the reconstruction process.

LED spectra after RL deconvolution are shown in Fig.7.12. The shapes and details of the peaks are unaffected during the deconvolution. The bumpy double cone structures in the cube are also removed during the process. There is little scattered intensity, and the resulting spectrum is decent.

Compared with some typical LED spectra shown in Fig.7.13, LED 1 has a combined green and yellow spectrum. The rest 4 LEDs have spectra of yellow or orange. The results match their original color, and their raw spectra on the grism-dispersed images. In conclusion, back projection plus RL deconvolution yields good LED spectra even with multiple sources in the field.

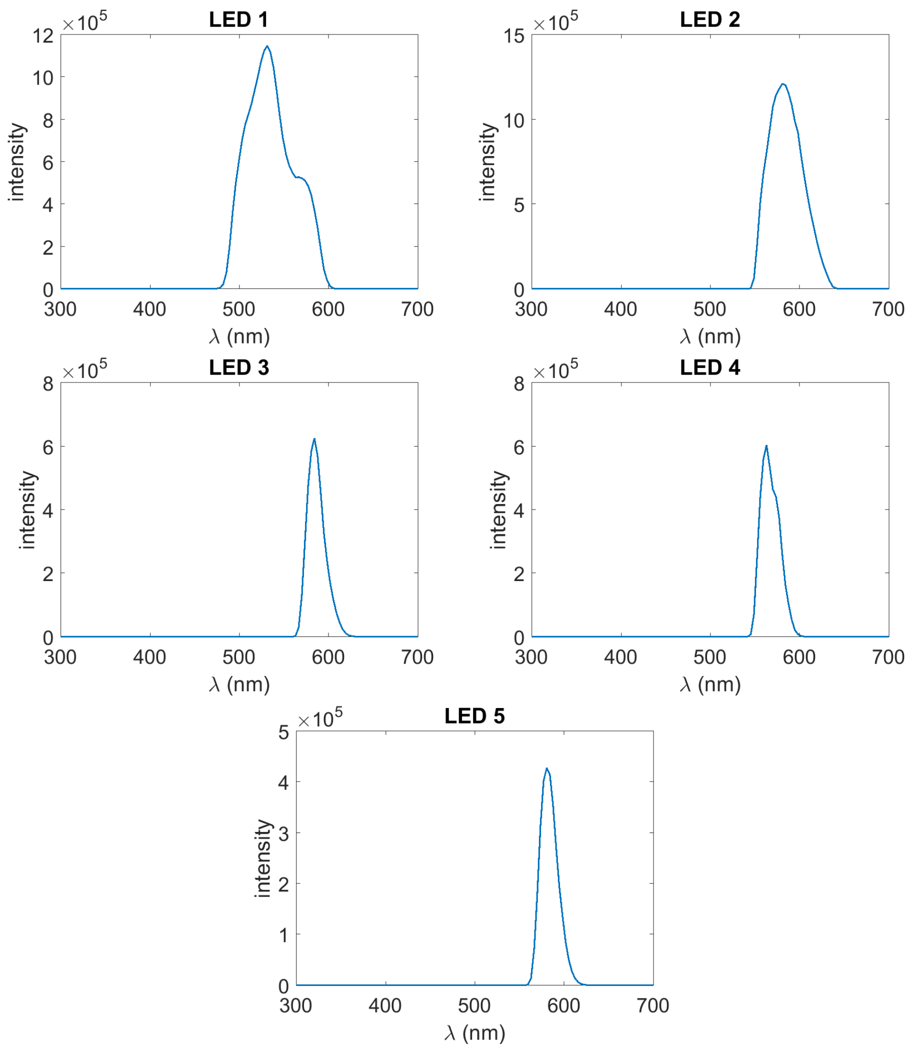

Figure 7.12: Spectra of 5 LEDs after Richardson-Lucy deconvolution.

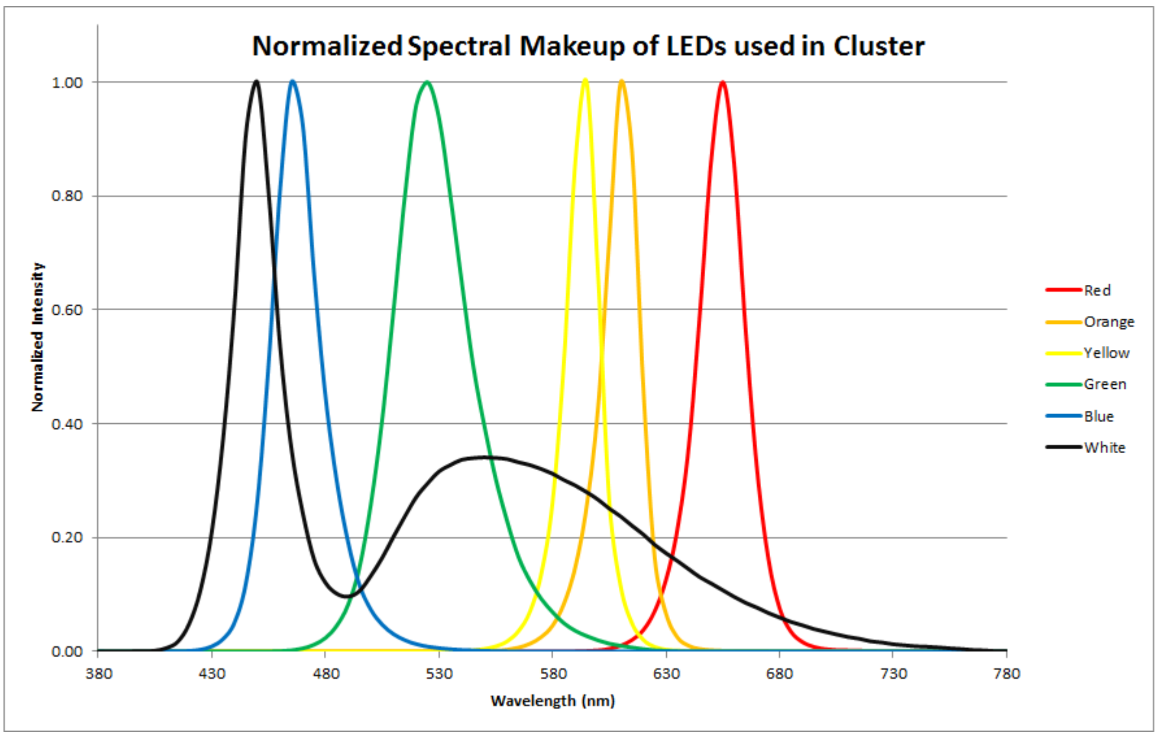

Figure 7.13: Typical LED spectra from the websites. Figure adapted from [14].

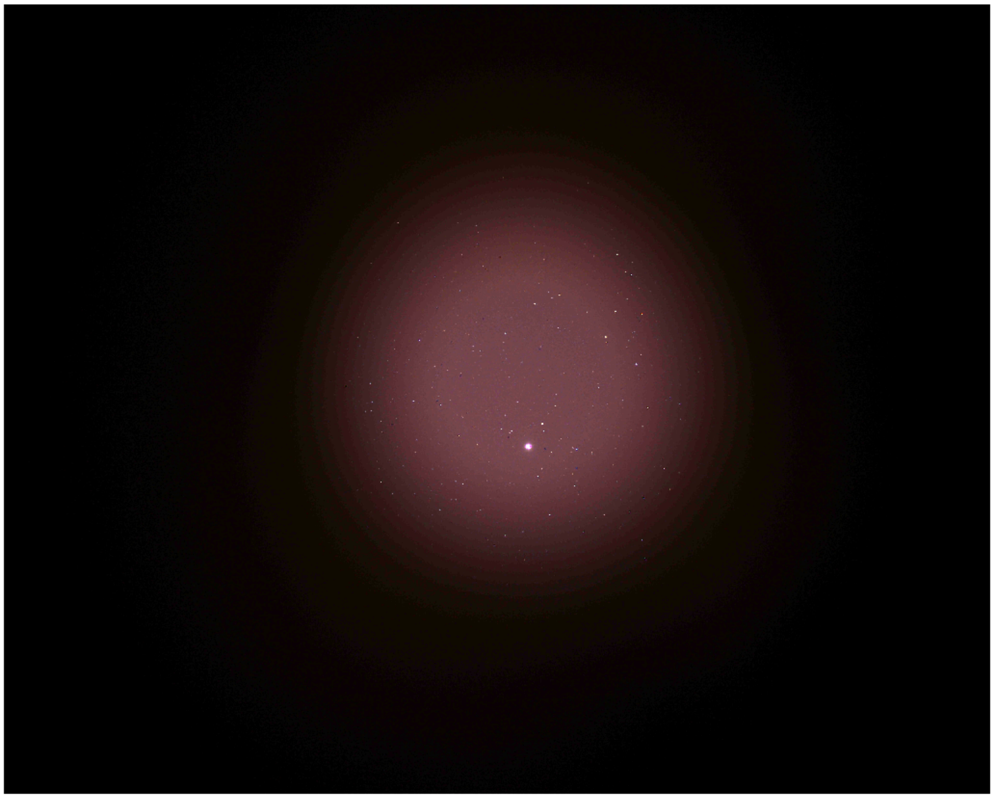

Figure 7.14: The sky image taken by my telescope without the grism. The brightest star in the image is Capella. The image brightness is increased for better visibility.

7.3 Stars

The last experiment I did is to observe the sky. I installed the telescope on a MEADE LXD55-Series Mount which can track the objects on the sky. The tracking is managed by Autostar Computer Controller. I pointed the telescope mainly at bright stars because the optics quality is poor and there is a maximum exposure time for the camera. Here I use the data set tracking Capella as an example. The sky region I pointed at is shown in Fig.7.14. I enhanced the image brightness to make the stars more visible to readers. There is only light at the center circle of the image due to the field stop. Capella is the brightest star in the image and there are a few fainter stars.

I show 8 sample images from the set of the grism-dispersed images in Fig.7.15. The images are taken with 10 seconds exposure time and ISO 100. I took 90 grism-dispersed images in total, making the angular step size $\alpha = 3°$. The only long spectrum visible in the figure is the spectrum of Capella. In the first three images, we can also find a short spectrum, which is the dispersion of zeroth order diffraction by the prism. I again increase the brightness of the images and the dim circle around the center is the spectrum from the background. More stars will show on the images if I increase the exposure time. But the tracking system of the mount is not accurate enough for long time exposure, where stars start to drift. Thus I only show the reconstruction result of this single star in this section.

The back projection angle is chosen at $\beta = 45°$, and I bin 16×16 finest pixels together. For the grism-dispersed images, I use only the regions that contain the spectrum for deconvolution and subtract the background from those images. The spectrum of Capella after back projection is shown in Fig.7.16. We can see a broad spectrum that matches the spectral length on the raw grism-dispersed images. Due to the low spectral resolution, there are not many absorption features in the spectrum.

The spectrum after Fourier deconvolution and RL deconvolution is shown in Fig.7.17 respectively. For the Fourier result, most features are kept the same except that there appear negative values in the spectrum. The scattered intensity and high-frequency noise also make the curve less smooth. For the RL result, features on the curve become sharper and the scattered intensity is reduced. Both results are consistent with the experiments on laser and LEDs.

As a comparison, I show the spectrum of a typical giant star G4III in Fig.7.18. Since Capella is classified as a G3III star, its spectrum can be roughly described by this plot. Although the features do not match exactly, the envelope of my reconstructed spectrum has a similar shape. The range and intensity are different mainly because of the RGB filter in the camera. I have not calibrated the spectral response of my GSTI, and therefore I show the spectral response of a Nikon camera found on the website in Fig.7.19. Comparing Fig.7.19 and Fig.7.17, we can observe that big notch comes from the intersection between red curve and green curve. Other small features on the reconstructed spectrum are also caused by converting the RGB image to grayscale image. Overall, the GSTI is able to reconstruct the wide spectrum of bright objects with the proposed algorithm.

7.4 Conclusion

In this chapter, I ran three experiments on the prototype GSTI with HeNe laser, LEDs, and stars. I built a control system to instruct the GSTI to rotate the grism and obtain a set of grism-dispersed images. It can effectively map the hyperspectral data cube that contains multiple sources. The proposed simple back projection plus RL deconvolution algorithm successfully reconstruct the spectra from the experimental data set. The reconstructed spectra match the shape of the sample spectra. However, higher quality optics would be required to proceed further with experimental investigation of this technique.

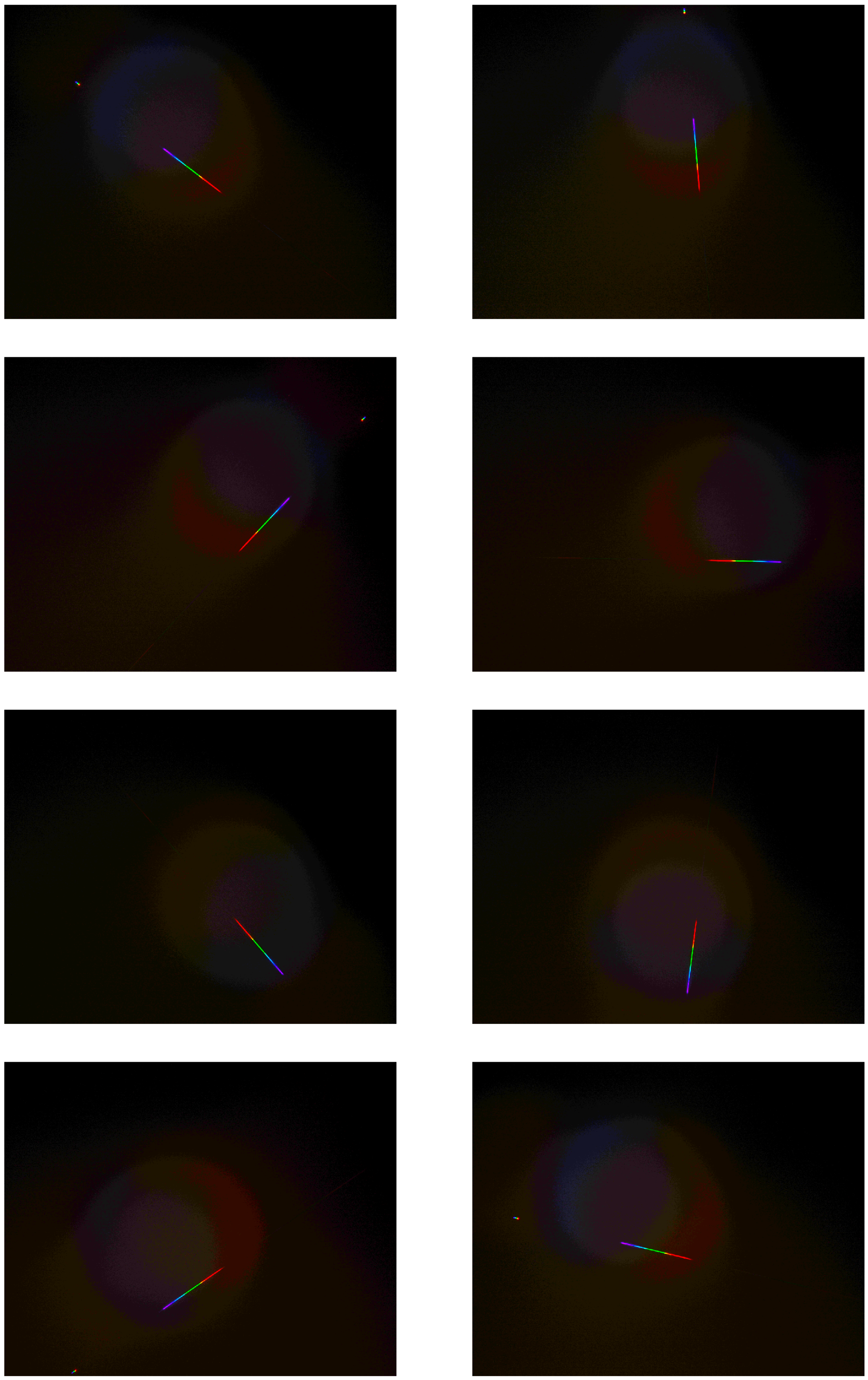

Figure 7.15: Raw grism-dispersed images from the sky shown above. The spectrum of Capella is the only visible spectrum in the image. The long spectrum is the first order diffraction, and the short spectrum in some of the images is the zeroth order diffraction. The background spectrum is also visible in these images.

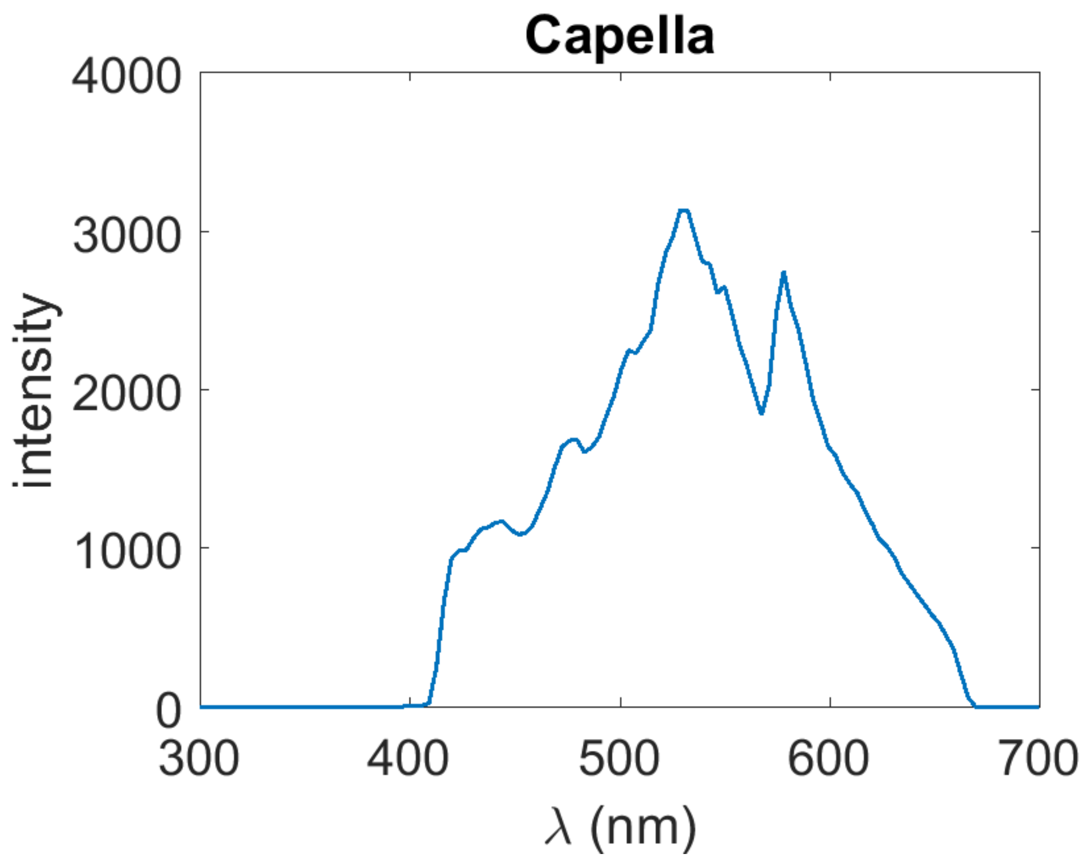

Figure 7.16: Spectrum of Capella after basic back projection, but before deconvolution.

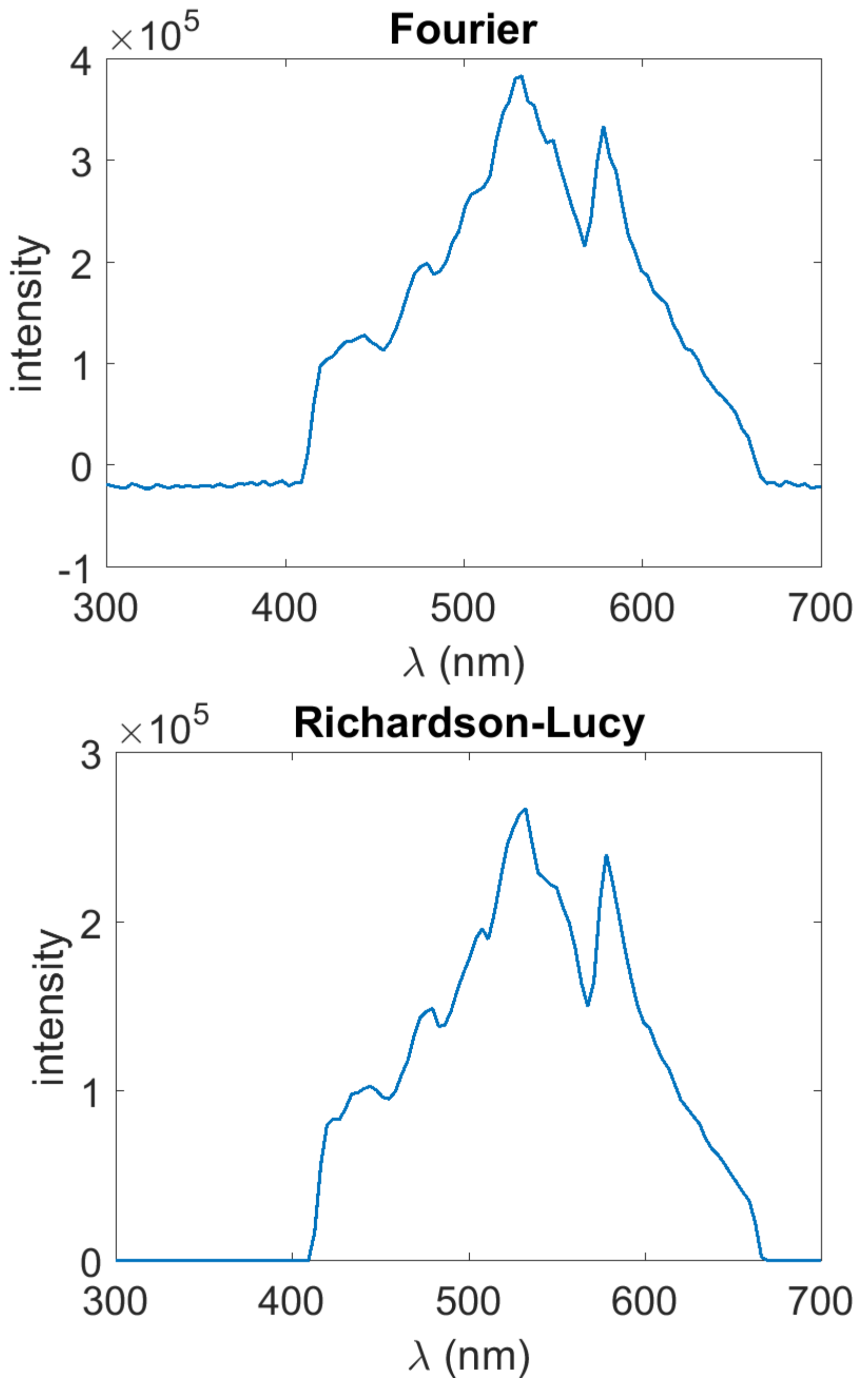

Figure 7.17: Top: Spectrum of Capella after fourier deconvolution. Bottom: Spectrum of Capella after RL deconvolution.

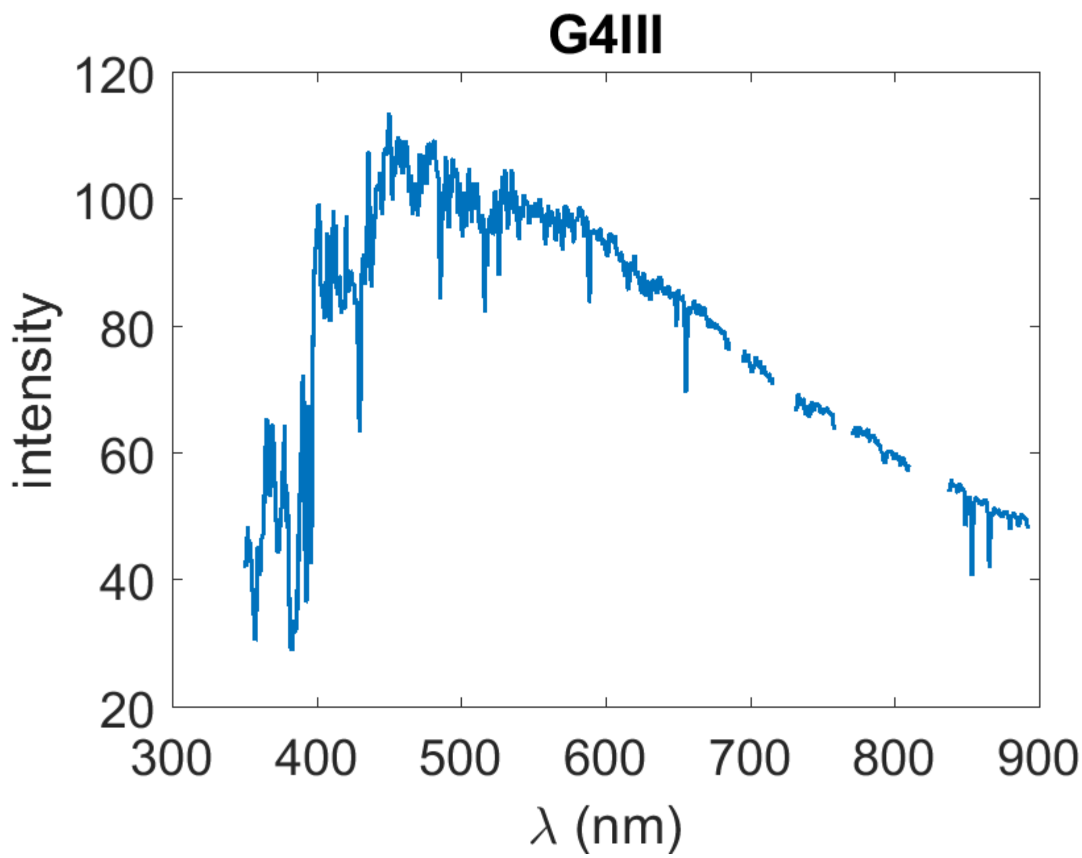

Figure 7.18: Model spectrum of a G4III star. Data from [15].

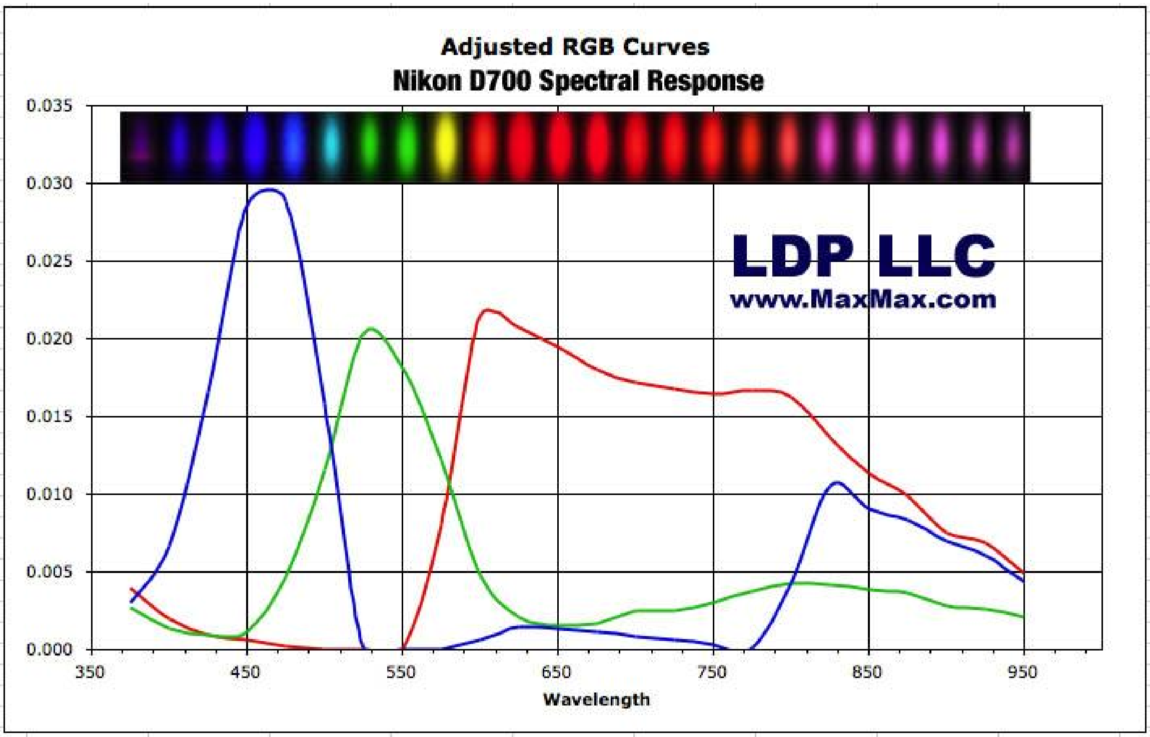

Figure 7.19: Nikon D700 spectral response.Figure adapted from [16].

Chapter 8

Conclusion

This thesis focuses on designing, analyzing, building, and testing a new telescope for Lyα intensity mapping. This new telescope I built is called Grism Spectrotomographic Imager (GSTI). It has a rotating grism in front of a Nikon D800 camera and takes a set of grism-dispersed images as the grism rotates. This set of grism-dispersed images is then processed to reconstruct the hyperspectral data cube based on grism spectrotomograpy principles.

In Chapter 2, I gave a general review of various types of integral field spectroscopy. By comparing their advantages and disadvantages, I concluded that Grism Spectrotomograph (GST) and Imaging Fourier Transform Spectrometer (IFTS) are two most suitable techniques for intensity mapping. In particular, GST and IFTS have the multiplex advantages that offer high throughput and low cost. GST is also less complex compared to IFTS.

In Chapter 3, I described three major sources of foreground contamination: continuum foreground, line foreground, and star foreground. The continuum foreground is relatively low in u band for the ground-based telescope, so I focused on intensity mapping in u band. Star foreground is a serious problem for intensity mapping in the visible light band, and it has not been fully studied. Masking bright stars is required to recover the Lyα power spectrum from the intensity mapping. I developed a masking and filtering scheme. First, I masked all the stars brighter than magnitude 18 at the image plane. Second, I designed a quarter circle filter with a stripe removed, which retains the modes of high Lyα power. The Lyα power dominates the power spectrum, and the ratio of Lyα power to star power can achieve 1000 after this masking and filtering. The results indicate that SDSS photometry catalog and bright stars catalog can be used together to mask stars for intensity mapping experiments. The masking scheme also provides an upper limit for the angular resolution, which is $74''$ at the loss of 10% pixels. This pixel scale makes IFTS and GST more feasible for intensity mapping.

In Chapter 4, I described the GSTI I built in the lab. It consists of a tube field stop, a grism attached to a rotating stage, the Nikon D800 camera and the lens. I listed the relevant specifications and showed sample images from the GSTI. I also demonstrated a more general design that puts the mask and the field stop at the image plane.

In Chapter 5, I described the imaging model I used for the GSTI. Due to the similarity between GST and CAT scan, the grism-dispersed images can be viewed as the projection of hyperspectral data cube onto the sensor plane. Thus I developed a two-step algorithm to reconstruct the hyperspectral data cube: the simple back projection followed by the PSF deconvolution. The back projection was then carefully explained and implemented. And I also explained using the Fourier slice theorem that this grism technique suffers from incomplete information during the image acquisition process. I also studied the resolution of the GSTI based on the back projection algorithm and the Fourier slice theorem.

In Chapter 6, I explored direct Fourier deconvolution and the Richardson-Lucy (RL) deconvolution under different scenarios. The Fourier deconvolution serves as a baseline result, and the RL deconvolution works better and more efficiently than other common deconvolution techniques. The difficulty of deconvolution comes from the back projection, which places $(L_z - 1)$ times more intensity into the hyperspectral cube where L_z is the cube's length in z-direction. The simulation results showed that Fourier method leaves a large amount of scattered intensity in the cube. On the other hand, RL method yields much less scattered intensity by eliminating faint sources and imposing positivity in the cube. For both methods, the scattered intensity is dominated by the few brightest sources. Both methods exhibited a dynamic range of 1000, which means the dim source cannot be recovered when it is more than 1000 times dimmer than the bright source. I then demonstrated with simulated Lyα sources and stars that masking stars is necessary for deconvolution. According to my simulation, 50% of the total Lyα intensity can be recovered using RL method if we mask all stars brighter than magnitude 20 from the SDSS.

In Chapter 7, I tested my GSTI with HeNe laser, LEDs and stars. For each experiment, I first took the set of grism dispersed images with a control program I wrote. Then I applied the two-step reconstruction algorithm to acquire the spectra of the sources. Even though the quality of optics is limited, the RL method produces the spectra of sources with low scattered noises. The results match the shapes of their true spectra under the spectral response of the sensor. GSTI is able to reconstruct the spectra of multiple bright sources in the field. Higher quality optics and spectral response calibration would be required to proceed further with experimental investigation of this technique.

8.1 Future Work

For star foreground, the power spectrum of stars at other filter bands can be calculated for Lyα intensity mapping at higher redshifts. The completeness curve of a catalog may be taken into account if stars are masked in other bands where they are brighter. Besides, I can consider large scale correction and projection effect to calculate the power spectrum more accurately. The filter shape can be further optimized to minimize the star contamination. Another thing I can do is to use different spectra for different stars to better approximate the power spectrum from stars.

For the telescope, higher quality optics and better tracking can be used to further investigate the GST technique. For example, I can reconstruct the spectra of a star cluster with better grism and tracking mount. To compare with the actual spectrum, it is necessary to calibrate the camera spectral response. I can also try the intensity mapping on a small field with proper optics, and develop the data processing pipeline. It is more thorough to test reconstruction algorithms on spatially extended sources in contrast to point sources. The masking technique can be tested with SDSS catalog and better instruments. Since GALEX used the grism at different angles, their spectra images can potentially be used to analyze real Lyα intensity mapping with GST. It is also important to describe the full practical requirements for the GSTI to perform cosmological Lyα intensity mapping, such as integration time. Besides GST, it is also important to test the other suitable technique for Lyα intensity mapping: IFTS. The results of IFTS can then be compared with GST for future intensity mapping telescopes.

For reconstruction, I can take into account that PSF depends on location in the back projection case and use a larger cube to minimize this effect. The back projection angle β may be better selected to further improve the spectral resolution and reconstruction result. Improvements on RL method should be studied to enhance stability and dynamic range, such as regularized RL method. More complicated reconstruction algorithms should also be explored given better computation resources. Other than back projection, I can try several algebraic reconstruction techniques (ART) or impose sparsity in wavelet space. Latest machine learning methods and image processing algorithms may also be helpful to the reconstruction. The implication of Fourier slice theorem on the power spectrum can also be studied.

Bibliography

[1] Ch Leinert, S Bowyer, LK Haikala, MS Hanner, MG Hauser, A-Ch Levasseur-Regourd, I Mann, K Mattila, WT Reach, W Schlosser, et al. The 1997 reference of diffuse night sky brightness. *Astronomy and Astrophysics Supplement Series*, 127(1):1–99, 1998.

[2] Throughput definition. Available at `https://en.wikipedia.org/wiki/File:Etendue-Definition.png`.

[3] Patrick Morrissey, David Schiminovich, Tom A Barlow, D Christopher Martin, Brian Blakkolb, Tim Conrow, Brian Cooke, Kerry Erickson, James Fanson, Peter G Friedman, et al. The on-orbit performance of the galaxy evolution explorer. *The Astrophysical Journal Letters*, 619(1):L7, 2005.

[4] Patrick Morrissey, Tim Conrow, Tom A Barlow, Todd Small, Mark Seibert, Ted K Wyder, Tamás Budavári, Stephane Arnouts, Peter G Friedman, Karl Forster, et al. The calibration and data products of galex. *The Astrophysical Journal Supplement Series*, 173(2):682, 2007.

[5] Goodwin M. Feger T. and Poppett C.L. Focal ratio degradation study of non-circular shaped fibres. `http://astrospectroscopy.files.wordpress.com/2011/06/noncircular-fibres.pdf`.

[6] K Bundy et al. Mapping nearby galaxies at apo (manga). `http://www.sdss.org/surveys/manga/#instrumentation`.

[7] Roger Bacon, Yannick Copin, G Monnet, Bryan W Miller, JR Allington-Smith, M Bureau, C Marcella Carollo, Roger L Davies, Eric Emsellem, Harald Kuntschner, et al. The sauron project–i. the panoramic integral-field spectrograph. *Monthly Notices of the Royal Astronomical Society*, 326(1):23–35, 2001.

[8] Robert Content. New design for integral field spectroscopy with 8-m telescopes. In *Optical telescopes of today and tomorrow*, pages 1295–1305. International Society for Optics and Photonics, 1997.

[9] Jeremy R Allington-Smith, Robert Content, and Roger Haynes. New developments in integral field spectroscopy. In *Astronomical Telescopes & Instrumentation*, pages 196–205. International Society for Optics and Photonics, 1998.

[10] JP Maillard, L Drissen, F Grandmont, and S Thibault. Integral wide-field spectroscopy in astronomy: the imaging fts solution. *Experimental Astronomy*, 35(3):527–559, 2013.

[11] Imaging data quality. Available at `http://www.sdss.org/dr12/imaging/other_info/`.

[12] Kevork Abazajian, Jennifer K Adelman-McCarthy, Sahar S Allam, Kurt SJ Anderson, Scott F Anderson, James Annis, Neta A Bahcall, Ivan K Baldry, Steven Bastian, Andreas Berlind, et al. The second data release of the sloan digital sky survey. *The Astronomical Journal*, 128(1):502, 2004.

[13] Michael W Kudenov, Julia Craven-Jones, Riley Aumiller, Corrie Vandervlugt, and Eustace L Dereniak. Faceted grating prism for a computed tomographic imaging spectrometer. *Optical Engineering*, 51(4):044002–1, 2012.

[14] Engineering design guide and environment. Available at `http://edge.rit.edu/edge/P11543/public/LED%20Specifications`.

[15] David R Silva and Mark E Cornell. A new library of stellar optical spectra. *The Astrophysical Journal Supplement Series*, 81:865–881, 1992.

[16] Nikon d700 study. Available at `https://www.maxmax.com/faq/camera-tech/spectral-response/nikon-d700-study`.

[17] David H Weinberg, Michael J Mortonson, Daniel J Eisenstein, Christopher Hirata, Adam G Riess, and Eduardo Rozo. Observational probes of cosmic acceleration. *Physics Reports*, 530(2):87–255, 2013.

[18] Daniel J Eisenstein, Idit Zehavi, David W Hogg, Roman Scoccimarro, Michael R Blanton, Robert C Nichol, Ryan Scranton, Hee-Jong Seo, Max Tegmark, Zheng Zheng, et al. Detection of the baryon acoustic peak in the large-scale correlation function of sdss luminous red galaxies. *The Astrophysical Journal*, 633(2):560, 2005.

[19] Adam K Tilling, G OLeary, JG Ferwerda, SD Jones, G Fitzgerald, and R Belford. Remote sensing to detect nitrogen and water stress in wheat. *The Australian Society of Agronomy*, 2006.

[20] H Holma. Thermische hyperspektralbildgebung im langwelligen infrarot, 2011.

[21] Kevin T. Higgins. Five new technologies for inspection. `http://www.foodprocessing.com/articles/2013/inspection-technologies/`.

[22] Will J Percival, Carlton M Baugh, Joss Bland-Hawthorn, Terry Bridges, Russell Cannon, Shaun Cole, Matthew Colless, Chris Collins, Warrick Couch, Gavin Dalton, et al. The 2df galaxy redshift survey: the power spectrum and the matter content of the universe. *Monthly Notices of the Royal Astronomical Society*, 327(4):1297–1306, 2001.

[23] Donald G York, J Adelman, John E Anderson Jr, Scott F Anderson, James Annis, Neta A Bahcall, JA Bakken, Robert Barkhouser, Steven Bastian, Eileen Berman, et al. The sloan digital sky survey: Technical summary. *The Astronomical Journal*, 120(3):1579, 2000.

[24] Kyle S Dawson, David J Schlegel, Christopher P Ahn, Scott F Anderson, Éric Aubourg, Stephen Bailey, Robert H Barkhouser, Julian E Bautista, Alessandra Beifiori, Andreas A Berlind, et al. The baryon oscillation spectroscopic survey of sdss-iii. *The Astronomical Journal*, 145(1):10, 2012.

[25] Daniel J Eisenstein, David H Weinberg, Eric Agol, Hiroaki Aihara, Carlos Allende Prieto, Scott F Anderson, James A Arns, Éric Aubourg, Stephen Bailey, Eduardo Balbinot, et al. Sdss-iii: Massive spectroscopic surveys of the distant universe, the milky way, and extra-solar planetary systems. *The Astronomical Journal*, 142(3):72, 2011.

[26] Richard A Battye, Rod D Davies, and Jochen Weller. Neutral hydrogen surveys for high-redshift galaxy clusters and protoclusters. *Monthly Notices of the Royal Astronomical Society*, 355(4):1339–1347, 2004.

[27] Shiv K Sethi. H i signal from re-ionization epoch. *Monthly Notices of the Royal Astronomical Society*, 363(3):818–830, 2005.

[28] J Stuart B Wyithe and Abraham Loeb. The 21-cm power spectrum after reionization. *Monthly Notices of the Royal Astronomical Society*, 397(4):1926–1934, 2009.

[29] Tzu-Ching Chang, Ue-Li Pen, Jeffrey B Peterson, and Patrick McDonald. Baryon acoustic oscillation intensity mapping of dark energy. *Physical Review Letters*, 100(9):091303, 2008.

[30] Jeffrey B Peterson, Roy Aleksan, Reza Ansari, Kevin Bandura, Dick Bond, John Bunton, Kermit Carlson, Tzu-Ching Chang, Fritz DeJongh, Matt Dobbs, et al. 21 cm intensity mapping. *arXiv preprint arXiv:0902.3091*, 2009.

[31] Mattia Righi, Carlos Hernandez-Monteagudo, and RA Sunyaev. Carbon monoxide line emission as a cmb foreground: tomography of the star-forming universe with different spectral resolutions. *Astronomy & Astrophysics*, 489(2):489–504, 2008.

[32] Adam Lidz, Steven R Furlanetto, S Peng Oh, James Aguirre, Tzu-Ching Chang, Olivier Doré, and Jonathan R Pritchard. Intensity mapping with carbon monoxide emission lines and the redshifted 21 cm line. *The Astrophysical Journal*, 741(2):70, 2011.

[33] Yan Gong, Asantha Cooray, Marta Silva, Mario G Santos, James Bock, C Matt Bradford, and Michael Zemcov. Intensity mapping of the [c ii] fine structure line during the epoch of reionization. *The Astrophysical Journal*, 745(1):49, 2011.

[34] Marta Silva, Mario G Santos, Asantha Cooray, and Yan Gong. Prospects for detecting c ii emission during the epoch of reionization. *The Astrophysical Journal*, 806(2):209, 2015.

[35] Bade D Uzgil, James E Aguirre, Charles M Bradford, and Adam Lidz. Measuring galaxy clustering and the evolution of [c ii] mean intensity with far-ir line intensity mapping during 0.5¡ z¡ 1.5. *The Astrophysical Journal*, 793(2):116, 2014.

[36] Yan Gong, Asantha Cooray, and Mario G Santos. Probing the pre-reionization epoch with molecular hydrogen intensity mapping. *The Astrophysical Journal*, 768(2):130, 2013.

[37] Marta B Silva, Mario G Santos, Yan Gong, Asantha Cooray, and James Bock. Intensity mapping of lyα emission during the epoch of reionization. *The Astrophysical Journal*, 763(2):132, 2013.

[38] Eli Visbal, Zoltán Haiman, and Greg L Bryan. Looking for population iii stars with he ii line intensity mapping. *Monthly Notices of the Royal Astronomical Society*, 450(3):2506–2513, 2015.

[39] José Fonseca, Marta B Silva, Mário G Santos, and Asantha Cooray. Cosmology with intensity mapping techniques using atomic and molecular lines. *Monthly Notices of the Royal Astronomical Society*, 464(2):1948–1965, 2017.

[40] Andrew Gould and David H Weinberg. Imaging the forest of lyman limit systems. *The Astrophysical Journal*, 468:462, 1996.

[41] J Michael Shull and Michael E van Steenberg. X-ray secondary heating and ionization in quasar emission-line clouds. *The Astrophysical Journal*, 298:268–274, 1985.

[42] Sebastiano Cantalupo, Cristiano Porciani, and Simon J Lilly. Mapping neutral hydrogen during reionization with the lyα emission from quasar ionization fronts. *The Astrophysical Journal*, 672(1):48, 2008.

[43] Marta B. Silva, Robin Kooistra, and Saleem Zaroubi. Mapping the low-surface brightness universe in the uv band with lyα emission from igm filaments. *Monthly Notices of the Royal Astronomical Society*, 462(2):1961–1971, 2016.

[44] Scott Dodelson. *Modern cosmology*. Academic press, 2003.

[45] Anthony R Pullen, Olivier Doré, and Jamie Bock. Intensity mapping across cosmic times with the lyα line. *The Astrophysical Journal*, 786(2):111, 2014.

[46] P Comaschi and A Ferrara. Probing high-redshift galaxies with lyα intensity mapping. *Monthly Notices of the Royal Astronomical Society*, 455(1):725–738, 2016.

[47] LM Haffner, RJ Reynolds, SL Tufte, GJ Madsen, KP Jaehnig, and JW Percival. The wisconsin hα mapper northern sky survey. *The Astrophysical Journal Supplement Series*, 149(2):405, 2003.

[48] D Christopher Martin, James Fanson, David Schiminovich, Patrick Morrissey, Peter G Friedman, Tom A Barlow, Tim Conrow, Robert Grange, Patrick N Jelinsky, Bruno Milliard, et al. The galaxy evolution explorer: A space ultraviolet survey mission. *The Astrophysical Journal Letters*, 619(1):L1, 2005.

[49] Olivier Doré, Jamie Bock, Matthew Ashby, Peter Capak, Asantha Cooray, Roland de Putter, Tim Eifler, Nicolas Flagey, Yan Gong, Salman Habib, et al. Cosmology with the spherex all-sky spectral survey. *arXiv preprint arXiv:1412.4872*, 2014.

[50] Olivier Doré, Michael W Werner, Matt Ashby, Pancha Banerjee, Nick Battaglia, James Bauer, Robert A Benjamin, Lindsey E Bleem, Jamie Bock, Adwin Boogert, et al. Science impacts of the spherex all-sky optical to near-infrared spectral survey: Report of a community workshop examining extragalactic, galactic, stellar and planetary science. *arXiv preprint arXiv:1606.07039*, 2016.

[51] Takayuki Okamoto and Ichirou Yamaguchi. Simultaneous acquisition of spectral image information. *Optics letters*, 16(16):1277–1279, 1991.

[52] Takayuki Okamoto, Akinori Takahashi, and Ichirou Yamaguchi. Simultaneous acquisition of spectral and spatial intensity distribution. *Applied Spectroscopy*, 47(8):1198–1202, 1993.

[53] Theodor V Bulygin and Gennady N Vishnyakov. Spectrotomography: a new method of obtaining spectrograms of two-dimensional objects. In *Analytical Methods for Optical Tomography*, pages 315–322. International Society for Optics and Photonics, 1992.

[54] JM Mooney. Spectral imaging via computed tomography. In *Proceedings of the 1994 Meeting of the Infrared Information Symposia Specialty Group on Passive Sensors*, volume 1, pages 203–215, 1994.

[55] PA Bernhardt. Direct reconstruction methods for hyperspectral imaging with rotational spectrotomography. *JOSA A*, 12(9):1884–1901, 1995.

[56] Avinash C Kak and Malcolm Slaney. *Principles of computerized tomographic imaging*. SIAM, 2001.

[57] C Hamaker, KT Smith, DC Solmon, and SL Wagner. The divergent beam x-ray transform. *Rocky Mt. J. Math.*, 10, 1980.

[58] Xiaochuan Pan, Emil Y Sidky, and Michael Vannier. Why do commercial ct scanners still employ traditional, filtered back-projection for image reconstruction? *Inverse problems*, 25(12):123009, 2009.

[59] Yan Betremieux, Timothy A Cook, Daniel M Cotton, and Supriya Chakrabarti. Spinr: two-dimensional spectral imaging through tomographic reconstruction. *Optical Engineering*, 32(12):3133–3138, 1993.

[60] Harrison H Barrett and William Swindell. *Radiological imaging: the theory of image formation, detection, and processing*, volume 2. Academic Press, 1996.

[61] Harrison H Barrett. Image reconstruction and the solution of inverse problems in medical imaging. In *Medical Images: Formation, Handling and Evaluation*, pages 3–42. Springer, 1992.

[62] Robert M Lewitt. Reconstruction algorithms: transform methods. *Proceedings of the IEEE*, 71(3):390–408, 1983.

[63] Yair Censor. Finite series-expansion reconstruction methods. *Proceedings of the IEEE*, 71(3):409–419, 1983.

[64] Richard Gordon, Robert Bender, and Gabor T Herman. Algebraic reconstruction techniques (art) for three-dimensional electron microscopy and x-ray photography. *Journal of theoretical Biology*, 29(3):471–481, 1970.

[65] Samuel C Barden and Richard A Wade. Densepak and spectral imaging with fiber optics. In *Fiber optics in astronomy*, volume 3, pages 113–124, 1988.

[66] N Drory, N MacDonald, MA Bershady, K Bundy, J Gunn, DR Law, M Smith, R Stoll, CA Tremonti, DA Wake, et al. The manga integral field unit fiber feed system for the sloan 2.5 m telescope. *The Astronomical Journal*, 149(2):77, 2015.

[67] Kevin Bundy, Matthew A Bershady, David R Law, Renbin Yan, Niv Drory, Nicholas MacDonald, David A Wake, Brian Cherinka, José R Sánchez-Gallego, Anne-Marie Weijmans, et al. Overview of the sdss-iv manga survey: mapping nearby galaxies at apache point observatory. *The Astrophysical Journal*, 798(1):7, 2014.

[68] Jeremy Allington-Smith, Graham Murray, Robert Content, George Dodsworth, Roger Davies, Bryan W Miller, Inger Jorgensen, Isobel Hook, David Crampton, and Richard Murowinski. Integral field spectroscopy with the gemini multi-object spectrograph. i. design, construction, and testing. *Publications of the Astronomical Society of the Pacific*, 114(798):892, 2002.

[69] Peter McGregor, John Hart, Peter Conroy, Leigh Pfitzner, Gabe Bloxham, Damien Jones, Mark Downing, Murray Dawson, Peter Young, Mark Jarnyk, et al. Gemini near-infrared integral field spectrograph(nifs). In *Proceedings of SPIE*, volume 4841, pages 1581–1591, 2003.

[70] L Drissen, A-P Bernier, M Charlebois, É Brière, C Robert, G Joncas, P Martin, and F Grandmont. Science results from the imaging fourier transform spectrometer spiomm. In *SPIE Astronomical Telescopes+ Instrumentation*, pages 70147K–70147K. International Society for Optics and Photonics, 2008.

[71] JP Maillard. Bear imaging fts: high resolution spectroscopy in infrared emission lines. In *Imaging the Universe in three dimensions*, volume 195, page 185, 2000.

[72] F Grandmont, L Drissen, Julie Mandar, S Thibault, and Marc Baril. Final design of sitelle: a wide-field imaging fourier transform spectrometer for the canada-france-hawaii telescope. In *SPIE Astronomical Telescopes+ Instrumentation*, pages 84460U–84460U. International Society for Optics and Photonics, 2012.

[73] Michael Dopita, John Hart, Peter McGregor, Patrick Oates, Gabe Bloxham, and Damien Jones. The wide field spectrograph (wifes). *Astrophysics and Space Science*, 310(3-4):255–268, 2007.

[74] Gary J Hill, Sarah E Tuttle, Niv Drory, Hanshin Lee, Brian L Vattiat, DL DePoy, JL Marshall, Andreas Kelz, Dionne Haynes, Maximilian H Fabricius, et al. Virus: production and deployment of a massively replicated fiber integral field spectrograph for the upgraded hobby-eberly telescope. In *SPIE Astronomical Telescopes+ Instrumentation*, pages 91470Q–91470Q. International Society for Optics and Photonics, 2014.

[75] Gary J Hill, Karl Gebhardt, Eiichiro Komatsu, Niv Drory, Phillip J MacQueen, Josh Adams, Guillermo A Blanc, Ralf Koehler, Marc Rafal, Martin M Roth,

et al. The hobby-eberly telescope dark energy experiment (hetdex): Description and early pilot survey results. *arXiv preprint arXiv:0806.0183*, 2008.

[76] A Lyle Broadfoot and Kenneth R Kendall. The airglow spectrum, 3100–10,000 a. *Journal of Geophysical Research*, 73(1):426–428, 1968.

[77] JS Mathis, PG Mezger, and Ni Panagia. Interstellar radiation field and dust temperatures in the diffuse interstellar matter and in giant molecular clouds. *Astronomy and Astrophysics*, 128:212–229, 1983.

[78] B Hoffmann, C Tappert, W Schlosser, Th Schmidt-Kaler, S Kimeswenger, K Seidensticker, L Schmidtobreick, and W Hovest. Photographic surface photometry of the southern milky way-viii. high-resolution u, v and r surface photometries of the southern milky way. *Astronomy and Astrophysics Supplement Series*, 128(3):417–422, 1998.

[79] G Toller, H Tanabe, and JL Weinberg. Background starlight at the north and south celestial, ecliptic, and galactic poles. *Astronomy and astrophysics*, 188:24–34, 1987.

[80] Pieter G Van Dokkum, Roberto Abraham, and Allison Merritt. First results from the dragonfly telephoto array: the apparent lack of a stellar halo in the massive spiral galaxy m101. *The Astrophysical Journal Letters*, 782(2):L24, 2014.

[81] AS Fruchter, RN Hook, IC Busko, and M Mutchier. A package for the reduction of dithered undersampled images. In *The 1997 HST Calibration Workshop with a New Generation of Instruments*, page 518, 1997.

[82] AS Fruchter and RN Hook. Drizzle: A method for the linear reconstruction of undersampled images. *Publications of the Astronomical Society of the Pacific*, 114(792):144, 2002.

[83] RH Garstang. Night sky brightness at observatories and sites. *Publications of the Astronomical Society of the Pacific*, 101(637):306, 1989.

[84] PA Shaver, RA Windhorst, P Madau, and AG De Bruyn. Can the reionization epoch be detected as a global signature in the cosmic background? *arXiv preprint astro-ph/9901320*, 1999.

[85] Tiziana Di Matteo, Rosalba Perna, Tom Abel, and Martin J Rees. Radio foregrounds for the 21 centimeter tomography of the neutral intergalactic medium at high redshifts. *The Astrophysical Journal*, 564(2):576, 2002.

[86] Tiziana Di Matteo, Benedetta Ciardi, and Francesco Miniati. The 21-cm emission from the reionization epoch: extended and point source foregrounds. *Monthly Notices of the Royal Astronomical Society*, 355(4):1053–1065, 2004.

[87] Xiaomin Wang, Max Tegmark, Mário G Santos, and Lloyd Knox. 21 cm tomography with foregrounds. *The Astrophysical Journal*, 650(2):529, 2006.

[88] S Peng Oh and Katherine J Mack. Foregrounds for 21-cm observations of neutral gas at high redshift. *Monthly Notices of the Royal Astronomical Society*, 346(3):871–877, 2003.

[89] Mário G Santos, Asantha Cooray, and Lloyd Knox. Multifrequency analysis of 21 centimeter fluctuations from the era of reionization. *The Astrophysical Journal*, 625(2):575, 2005.

[90] Eli Visbal and Abraham Loeb. Measuring the 3d clustering of undetected galaxies through cross correlation of their cumulative flux fluctuations from multiple spectral lines. *Journal of Cosmology and Astroparticle Physics*, 2010(11):016, 2010.

[91] Paolo Comaschi and Andrea Ferrara. Empowering line intensity mapping to study early galaxies. *Monthly Notices of the Royal Astronomical Society*, 463(3):3078–3082, 2016.

[92] Yan Gong, Marta Silva, Asantha Cooray, and Mario G Santos. Foreground contamination in lyα intensity mapping during the epoch of reionization. *The Astrophysical Journal*, 785(1):72, 2014.

[93] Eli Visbal, Hy Trac, and Abraham Loeb. Demonstrating the feasibility of line intensity mapping using mock data of galaxy clustering from simulations. *Journal of Cosmology and Astroparticle Physics*, 2011(08):010, 2011.

[94] Patrick C Breysse, Ely D Kovetz, and Marc Kamionkowski. Masking line foregrounds in intensity-mapping surveys. *Monthly Notices of the Royal Astronomical Society*, 452(4):3408–3418, 2015.

[95] Franco D Albareti, Carlos Allende Prieto, Andres Almeida, Friedrich Anders, Scott Anderson, Brett H Andrews, Alfonso Aragon-Salamanca, Maria Argudo-Fernandez, Eric Armengaud, Eric Aubourg, et al. The thirteenth data release of the sloan digital sky survey: First spectroscopic data from the sdss-iv survey mapping nearby galaxies at apache point observatory. *arXiv preprint arXiv:1608.02013*, 2016.

[96] Kevork Abazajian, Jennifer K Adelman-McCarthy, Marcel A Agüeros, Sahar S Allam, Scott F Anderson, James Annis, Neta A Bahcall, Ivan K Baldry, Steven Bastian, Andreas Berlind, et al. The first data release of the sloan digital sky survey. *The Astronomical Journal*, 126(4):2081, 2003.

[97] C Wolf, K Meisenheimer, H-W Rix, A Borch, S Dye, and M Kleinheinrich. The combo-17 survey: Evolution of the galaxy luminosity function from 25 000 galaxies with $0.2 < z < 1.2$. *Astronomy & Astrophysics*, 401(1):73–98, 2003.

[98] Rupert AC Croft, Jordi Miralda-Escudé, Zheng Zheng, Adam Bolton, Kyle S Dawson, Jeffrey B Peterson, Donald G York, Daniel Eisenstein, Jon Brinkmann, Joel Brownstein, et al. Large-scale clustering of lyman α emission intensity from sdss/boss. *Monthly Notices of the Royal Astronomical Society*, 457(4):3541–3572, 2016.

[99] Dorrit Hoffleit and Carlos Jaschek. The bright star catalogue. *The Bright Star Catalogue, New Haven: Yale University Observatory (4th edition), 1982*, 1982.

[100] MAC Perryman et al. The hipparcos and tycho catalogues. *star*, 2:2π1, 1997.

[101] FL Whipple. Smithsonian astrophysical observatory star catalog. *Smithsonian Astrophysical Observatory Star Catalog, Washington: Smithsonian Institution Press, 1966*, 1966.

[102] Christopher Palmer and Erwin G Loewen. *Diffraction grating handbook*. Newport Corporation New York, 2005.

[103] Eugene Hecht. Optics 4th edition. *Optics, 4th Edition, Addison Wesley Longman Inc, 1998*, 1998.

[104] M. N. Polyanskiy. Refractive index database. `http://refractiveindex.info`.

[105] Ren Ng. Fourier slice photography. In *ACM Transactions on Graphics (TOG)*, volume 24, pages 735–744. ACM, 2005.

[106] Donald L Snyder. Modifications of the lucy–richardson iteration for restoring hubble space telescope imagery. *The Restoration of HST Images and Spectra*, pages 56–61, 1990.

[107] William Hadley Richardson. Bayesian-based iterative method of image restoration. *JOSA*, 62(1):55–59, 1972.

[108] Leon B Lucy. An iterative technique for the rectification of observed distributions. *The astronomical journal*, 79:745, 1974.

[109] Lawrence A Shepp and Yehuda Vardi. Maximum likelihood reconstruction for emission tomography. *IEEE transactions on medical imaging*, 1(2):113–122, 1982.

[110] Richard L White. Image restoration using the damped richardson-lucy method. In *1994 Symposium on Astronomical Telescopes & Instrumentation for the 21st Century*, pages 1342–1348. International Society for Optics and Photonics, 1994.

[111] Arthur P Dempster, Nan M Laird, and Donald B Rubin. Maximum likelihood from incomplete data via the em algorithm. *Journal of the royal statistical society. Series B (methodological)*, pages 1–38, 1977.

[112] David SC Biggs and Mark Andrews. Acceleration of iterative image restoration algorithms. *Applied optics*, 36(8):1766–1775, 1997.

[113] Nishikanta Khandai, Tiziana Di Matteo, Rupert Croft, Stephen Wilkins, Yu Feng, Evan Tucker, Colin DeGraf, and Mao-Sheng Liu. The massiveblack-ii simulation: the evolution of haloes and galaxies to z 0. *Monthly Notices of the Royal Astronomical Society*, 450(2):1349–1374, 2015.